5-2018

IAPP Amyloid Aggregation and IAPP-Associated Toxicity Mitigation

Xinwei Ge
Clemson University, xinweig@g.clemson.edu

IAPP AMYLOID AGGREGATION AND IAPP-ASSOCIATED TOXICITY MITIGATION

A Dissertation
Presented to
the Graduate School of
Clemson University

In Partial Fulfillment
of the Requirements for the Degree
Doctor of Philosophy
Physics

---

by
Xinwei Ge
May 2018

Accepted by:
Feng Ding, Committee Chair
Emil Alexov
Jian He
Hugo Sanabria

ABSTRACT

Human islet amyloid polypeptide (IAPP, *a.k.a.* amylin) is a 37-residue peptide hormone co-synthesized and co-secreted with insulin by pancreatic β-cells for glycemic control. Extensive research indicates that the amyloid aggregation of IAPP into cross-β amyloid fibrils is a ubiquitous phenomenon as well as a major factor in the development and pathogenesis of type 2 diabetes mellitus (T2D), which is a long-term metabolic disorder compromises the quality of life of millions globally. The amyloid IAPP aggregation products, either soluble intermediate oligomers or mature fibrils, are found toxic to human cells and capable of eliciting systemic damage in T2D patients. Recent studies reveal that IAPP is able to cross the blood-brain barrier and co-aggregate with human amyloid-beta (Aβ), which is the protein associated with another amyloid neurodegenerative disorder, the Alzheimer's disease (AD). *In vitro* experiments demonstrate that soluble IAPP could significantly accelerate the aggregation of Aβ, with accumulating clinical and epidemiological evidences also suggest that T2D and AD are linked together. Despite the significant differences in their pathologies, T2D is suggested as a risk factor for AD. Here, we investigate the possible mechanism of the co-aggregation of IAPP and Aβ to explore the cross-talk between these two diseases and propose that IAPP promotes Aβ aggregation by reducing the aggregation free energy barrier through its binding with Aβ. In addition, with the fact that IAPPs are stored inside β-cell granules without apparent aggregation in healthy individuals, we also study the physiological environment inside β-cell granules and its endogenous inhibition effect on IAPP aggregation. Our work demonstrates that Zn^{2+} coordinated molecular complex might be

important to stabilize IAPP and hence the endogenous inhibition. Moreover, we study the interactions between IAPP and two different materials, the small molecule epigallocatechin gallate (EGCG) and the star-shaped polymer poly(2-hydroxyethyl acrylate) (PHEA). Our study demonstrates both EGCG and PHEA as inhibitors against amyloidogenesis, while perform in different strategies. EGCG is able to inhibit IAPP aggregation and result in minimizing the population of toxic oligomers and protofibrils, while PHEA accelerates IAPP fibrillation to circumvent accumulation of the more toxic intermediates.

TABLE OF CONTENTS

Page

TITLE PAGE i

ABSTRACT ii

LIST OF FIGURES vi

CHAPTER

I. IAPP and Amyloid Aggregation 1

Function of IAPP 1
IAPP Aggregation and Type 2 Diabetes 1
Co-aggregation of IAPP and Aβ 2
The Endogenous Inhibition of IAPP Aggregation 3
Strategies for Mitigating IAPP-associated Toxicity 5

II. IAPP Promotes Aβ Aggregation by Binding-induce Helix-unfolding of the Amyloidogenic Core 6

Introduction 6
Results and Discussion 7
Conclusion 16
Materials and Methods 17

III. Zinc-coordination and C-peptide Complexation: A Potential Mechanism for the Endogenous Inhibition of IAPP Aggregation 21

Introduction 21
Results and Discussion 22
Conclusion 28
Materials and Methods 29

IV. IAPP Amyloid Inhibition by Small Molecules 32

Introduction 32
Results and Discussion 33
Conclusion 36
Materials and Methods 37

Table of Contents (Continued)

Page

V. Star Polymers Reduce the IAPP Toxicity via Accelerated Amyloid Aggregation....39

Introduction....39
Results and Discussion....40
Conclusion....46
Materials and Methods....47

FIGURE CAPTIONS....50

REFERENCES....87

LIST OF FIGURES

Figure Page

2.1 Time evolution of atomic contacts between IAPPs, Aβs, and IAPP-Aβ 50

2.2 Time evolution of peptide cluster species for IAPP-Aβ mixtures 51

2.3 Identification of hot regions for inter-peptide interactions in both cross- and self-associations of IAPP and Aβ 52

2.4 The secondary structure propensity of Aβ and IAPP in monomer, heterodimer, and homodimer (helix and β-sheet) 53

2.5 The secondary structure propensity of Aβ and IAPP in monomer, heterodimer, and homodimer (random coil and turn) 54

2.6 Conformational dynamics of the helix unfolding and refolding in the amyloidogenic region of Aβ16-22 55

2.7 Replica exchange simulations of IAPP monomer, Aβ monomer, and heterodimer 56

2.8 The conformational free energy landscape of the amyloidogenic Aβ16-22 at 300K.....57

2.9 ThT fluorescence assay data of peptides at different concentration 58

2.10 *In vitro* studies of IAPP-Aβ cross- and self-association 59

3.1 DMD simulations of IAPP dimerization with and without the presence of C-peptide.....60

3.2 Secondary structure information and residue-wise binding frequency maps of IAPPs with and without C-peptide 61

3.3 DMD simulations of the binding between Zn^{2+}, C-peptide, and IAPP at 1:1:1 molar ratio.....62

3.4 Surface structures of the Zn^{2+} coordinated heterodimer and heterotrimer of IAPP and C-peptide 63

3.5 DMD simulations of the heterodimer and heterotrimer.....64

List of Figures (Continued)

Figure Page

3.6 The centroid heterodimer structures of the top 10 clusters 65

3.7 Nucleation test of zinc-coordinated heterodimer and heterotrimer 66

3.8 Experimental studies of zinc-coordinated IAPP-C-peptide complexation .. 67

3.9 ThT fluorescence assay data on zinc-coordinated complexation for 14h of sample incubation 68

3.10 High-resolution TEM imaging of zinc-coordinated complexation for 24h of sample incubation 69

3.11 CD measurement of the secondary structures of IAPP control and IAPP/C-peptide/Zn^{2+} mixtures 70

3.12 Cell viability assay 71

4.1 ThT fluorescence assay data on IAPP fibrillation in the presence of fresh EGCG, oxidized EGCG, or reduced EGCG 72

4.2 Contour length of IAPP fibrils 73

4.3 Circular dichroism (CD) spectra of IAPP, and IAPP with fresh EGCG, oxidized EGCG and reduced EGCG 74

4.4 DMD simulations of 8 EGCG ligands binding with 8 IAPPs 75

4.5 DMD simulations of various numbers of EGCGs and IAPPs 76

4.6 DMD simulations of IAPP aggregation with ThA 77

5.1 ThT fluorescence assay data on IAPP fibrillation in the presence of PHEA stars over 24h 78

5.2 Normalized circular dichroism spectra of IAPP alone and in the presence of PHEA stars 79

5.3 TEM imaging of fibrillating IAPP in the presence and absence of PHEA stars and structural analysis of amyloid fibrils 80

List of Figures (Continued)

Figure Page

5.4 Protective effect of PHEA stars against IAPP-mediated cytotoxicity in pancreatic β-cells and islets 81

5.5 Simulations of PHEA stars 82

5.6 Binding of IAPP with 6-arm PHEA..... 83

5.7 β-sheet formation in IAPP aggregates is correlated with their binding with PHEA 84

5.8 Binding with PHEA star reduces the aggregation lag time and induces the heterogeneity in the fibril elongation rate of IAPP self-association 85

5.9 Aggregation free energy landscapes of IAPP without and with PHEA..... 86

CHAPTER ONE

IAPP and Amyloid Aggregation

Function of IAPP

Human islet amyloid polypeptide (IAPP, a.k.a. amylin) is a 37-residue peptide hormone co-synthesized, co-stored, and co-secreted with insulin by pancreatic β-cells for glycemic control.[1,2] IAPP is synthesized from a 67-residue precursor protein, proIAPP. Through proteolysis and posttranslational modification processes, including peptide cleavage, C-terminal amidation, and finally a disulfide bond formation between residues 2 and 7, the transformation from proIAPP to the biologically active IAPP is complete, with the sequence as KCNTATCATQRLANFLVHSSNNFGAILSSTNVGSNTY.[3,4] IAPP is known as a synergistic partner to insulin in terms of its function, which is able to control the blood glucose level by slowing down gastric emptying, inhibiting digestive secretion, and promoting satiety.[5,6]Addiitonally, IAPP is also reported to contribute to the bone metabolism, along with the related peptides calcitonin and calcitonin gene-related peptides.[7]

IAPP Aggregation and Type 2 Diabetes

IAPP is characterized as a peptide of high propensity to aggregate and readily to form amyloid fibrils *in vitro* at μM concentration within hours.[8] Accumulating studies report the observation of IAPP enriched amyloid plaques in the pancreas of type 2 diabetes (T2D) patients, as well as the quick formation of amyloid fibrils *in vitro*. As with many

other amyloid proteins, the amyloid aggregation of IAPP is a nucleation-dependent process with an "all-or-none" sigmoidal kinetics, where an initial lag phase of nucleation is followed by rapid elongation and saturation.[9–11] Both the aggregation intermediates and the mature amyloid fibrils of IAPP are found toxic to human cells, with the intermediates identified as the more toxic species. Previous study has shown that IAPP1-19 is a non-fibril forming segment, while its toxicity is similar to that of the full-length peptide.[12] Study of IAPP oligomers also find them could disrupt cell coupling, induce apoptosis, and impair insulin secretion in isolated human islets.[13] Together with other studies, the toxic oligomer hypothesis is proposed, claiming that it is the intermediate oligomers instead of the amyloid fibrils are the most toxic species and may be responsible for the β-cell death in T2D.[14,15]

Co-aggregation of IAPP and Aβ

Alzheimer's disease (AD) is another common aging-associated disease similar to T2D, with the shared pathological hallmarks such as peptide amyloid aggregation and deposition of amyloids. The aberrant aggregation of human amyloid-β (Aβ) and IAPP is implicated in AD and T2D respectively, with both peptides can self-assemble into amyloid fibrils and accumulate in human tissues as amyloid deposits.[16–22] Accumulating clinical and epidemiological research suggest that T2D and AD are linked to each other. Studies report a relatively frequent appearance of mixed pathologies of both diseases, and T2D has also been found as a major risk factor for AD.[23–33] Given experimental evidence of IAPP being able to cross the blood-brain barrier and possibly expressed in sensory neurons, the co-aggregation of IAPP and Aβ has been explored to uncover the cross-talk between T2D

and AD.[34–36] Both IAPP and Aβ can form amyloid fibrils with similar characteristic of the cross-β structure, but their aggregation rates are quite distinct. *In vitro* experiments under same concentration conditions reveal IAPP aggregates much faster than Aβ, while their mixture at 1:1 ratio aggregates with a much shorter lag phase than Aβ alone but slightly longer than IAPP.[37,38] These studies also report the mixture aggregates in a similar manner as IAPP or Aβ self-aggregation (e.g., in terms of aggregation kinetics, fibril morphology, and the ability to disrupt membranes), and eventually forms IAPP/Aβ hetero-complexes and hetero-fibrils. Based on these observations, it has been postulated that IAPP and Aβ would form hetero-complexes first upon mixture, and the complexes subsequently aggregate.

The Endogenous Inhibition of IAPP Aggregation

IAPP is known as highly aggregation prone, however this peptide is stored inside β-cell granules at mM concentration for hours without apparent aggregation in healthy individuals before its secretion to the bloodstream.[39] Therefore, the physiological environment inside β-cell granules endogenously inhibits the IAPP aggregation.

Islet β-cell granules have a pH value of 5.5, which is below the physiological pH of 7.4. The inhibition of IAPP aggregation by low pH has been studied *in vitro*, with the observations of increased aggregation lag time and decreased fibrillization rate compared to that under the physiological pH condition.[40,41] Previous studies suggest the protonated histindine18 (H18) of IAPP at low pH would introduce electrostatic repulsion between IAPPs and result in inhibition effct.[42,43] As the pH value inside β-cell granules is close to

the isoelectric point of H18, it may contribute to the endogenously inhibition, but not likely to be the key factor since a significant portion of IAPPs are still unprotonated.[40,44]

In addition to IAPP, β-cell granules also feature the high concentration of Zn^{2+} and other molecules including insulin and C-peptide. The large amount of Zn^{2+} inside granules is maintained by a β-cell-specific zinc transporter – ZnT8, and is believed important for the efficient storage of insulin: Zn^{2+} coordinates the formation of insulin hexamers, which constitute insulin crystals as the dense core of β-cell granules.[45,46] Zn^{2+} has been explored having a concentration-dependent effect on IAPP aggregation. A low concentration of Zn^{2+} could cross-link IAPP oligomers and therefore promotes the aggregation, while higher ion concentration leads to an inhibition effect due to the formation of Zn^{2+}-IAPP complex via coordination with H18 and hence the electrostatic repulsion among complexes.[47–50] With the concentration of Zn^{2+} kept increasing, the induced screening effect would reduce electrostatic repulsion and the aggregation would be slightly promoted again.[49,50]

Several studies reveal insulin has a strong inhibition effect on IAPP aggregation.[51–54] However, since most insulin are found as the insoluble crystal-like dense core inside β-cell granules while IAPPs are exclusively found in the soluble halo fraction, their contribution to the endogenously inhibition may be limited. C-peptide is another peptide co-localized with Zn^{2+} and IAPP, which is a proteolytic product of proinsulin and able to bind multiple IAPP and promote aggregation.[48] Upon mixture with Zn^{2+}, C-peptide binds Zn^{2+} with a 1:1 ratio in stoichiometry and adopts specific structures with reduced charges, which might bind and stabilize IAPP afterwards.[55] It has been hypothesized that a balance

of Zn^{2+} and C-peptide appears important for maintaining the native state of IAPP in addition to the low pH effect.

Strategies for Mitigating IAPP-associated Toxicity

Aggregation inhibition with the use of peptides, small molecules as well as polymeric nanoparticles (NPs) have been long explored to develop possible strategies against amyloid-mediated toxicity. Among all the approaches, the small molecule epigallocatechin gallate (EGCG, *a.k.a.* epigallocatechin-3-gallate) is a polyphenol small molecule and possesses the advantages of naturally occurring, non-toxic at moderate concentration, and modest water solubility (33.3-100 g/L). Previous studies reveal that upon interfacing with EGCG, the IAPP aggregation is rendered off-pathway and the mature IAPP fibrils even display remodeled.[56–58] A possible mechanism is that EGCG binds IAPP with aromatic residues, and therefore traps IAPP into an early intermediate state prior to IAPP amyloid formation with reduced toxicity. Differently, the star-shaped polymer poly(2-hydroxyethyl acrylate) (PHEA) nanostructure shows mitigating IAPP-associated toxicity by promoting aggregation. The PHEA stars are weakly negatively charged and contains multiple rigid arms, with each arm serves as linear scaffold for IAPP binding and promotes IAPP aggregation. Binding between IAPP and PHEA star induce a unique "stelliform amyloid" morphology, which displays reduced toxicity both *in vitro* and *ex vivo*. As a result, PHEA circumvents the accumulation of toxic intermediates and mitigates IAPP-associated toxicity.

CHAPTER TWO

IAPP Promotes Aβ Aggregation by Binding-induced Helix-unfolding of the Amyloidogenic Core

Introduction

Previous studies reveal the co-aggregation of IAPP and Aβ, and observe the hetero-complex/hetero-fibril formation. Upon the formation of hetero-complexes, conformational changes have been detected, but the molecular details and mechanisms of co-aggregation remain unknown. Both segment Aβ40 and Aβ42 are implicated in the pathogenesis of AD, with Aβ42 is characterized as more hydrophobic, more cytotoxic, and the most amyloidogenic form of this peptide. Here, by combining atomistic discrete molecular dynamics (DMD) simulations with complementary thioflavin-T fluorescence assay (ThT), we study the interactions between IAPP and Aβ42, the formation of hetero-complexes, and also the corresponding structures and conformational dynamics upon binding in order to understand the co-aggregation behaviors. Through our work, we first identify the IAPP-Aβ heterodimer as the most populated hetero-complexes during the early stage of co-aggregation when IAPP and Aβ are mixed at equimolar ratio *in silico*. The residue-wise inter-peptide interactions revealed by DMD simulations are consistent with experimentally identified hot-spot regions for IAPP-Aβ binding.[59] Our simulation results also suggest the helix unfolding of Aβ amyloidogenic region (16KLVFFAE22) as the major conformational change upon the formation of heterodimer. The complementary ThT assay applied by our collaborators confirms the accelerated amyloid aggregation of IAPP/Aβ mixture compared

to Aβ. Using an approach proposed by the Wetzel group, further analysis about the aggregation kinetics suggests that the rate-limiting step of Aβ42 aggregation is conformational changes taking place in approximately two peptides.[10] Together with our computational results and previous reports of Aβ42 oligomerization, we propose an aggregation mechanism that the helix unfolding of Aβ16-22 corresponds to the major free energy barrier of Aβ42 aggregation, which can take place in various Aβ42 oligomers populated during the early stage of aggregation.[60,61] Upon mixing with IAPP, the formation of IAPP-Aβ heterodimer induces the helix unfolding of Aβ16-22, which subsequently reduces the aggregation free energy barrier and accelerates the co-aggregation compared to Aβ42 alone. Our works offer a potential molecular mechanism for the increased AD risk in T2D patients as observed in clinical and epidemiological studies.

Results and Discussion

Heterodimer formation is the first step towards the co-aggregation of IAPP and Aβ. We perform all-atom DMD simulations of multiple IAPP and Aβ at 1:1 ratio to investigate the assembly dynamics of the peptide mixture. Two sets of molecular systems are studied, with one contains two IAPPs along with two Aβs and another has four peptides of each species, where the same peptide concentration is maintained. We perform 50 independent simulations with each lasted 200ns for the smaller system and 20 independent simulations with each lasted 100ns for the larger system at 300K, simulations are started with different initial inter-molecular distances and orientations.

To capture the assembly dynamics, we calculate the number of atomic contacts between various peptides and also monitor the formation of peptide clusters. When two IAPPs and two Aβs are mixed, the total number of contacts is dominated by the cross-species interactions, while both the contacts among IAPPs and among Aβs are significantly smaller (Fig. 2-1). The number of IAPP-Aβ contacts increases rapidly in the early stage of simulations with obvious lag-time observed for both IAPP-IAPP and Aβ-Aβ interactions, suggesting an initial hetero-complexes formation in the mixture. For the peptide clustering analysis, we compute the time evolution of various cluster species weighted by the number of peptides in a cluster (Fig. 2-2A). We observe rapid formation of IAPP-Aβ heterodimer following a decrease of initial monomers. The heterodimer is the most populated species before they finally associate into the hetero-hexamer. Similar association dynamics can also be observed for the larger system, where the heterodimer is also the most populated species during early assembly process, although other higher order oligomers (such as two IAPPs bound to one or three Aβs) are later observed before the appearance of hetero-octamer (Fig. 2-2B).

Hence, our simulations suggest that when IAPP and Aβ peptides are mixed at an equimolar ratio, the cross-species interaction dominates over their self-associations during the early assembly. The rapid formation of hetero-complexes could be explained by the opposite net charges of the two peptides (i.e., the net charges of IAPP and Aβ are +2e and -3e, respectively) and the relatively long-range electrostatic interactions under the physiological condition (the Debye length is ~10Å). Our results also indicate that the

heterodimer of IAPP and Aβ is the major intermediate species populated towards their co-aggregation.

Computationally observed inter-peptide interactions for both cross- and self-association of IAPP and Aβ are consistent with previous experiments. The hot-spot regions for both cross- and self-association of IAPP and Aβ have been investigated experimentally.[59] For experimental validation of our simulations, we perform DMD simulations of one IAPP with one Aβ mixture (i.e., cross-association), along with control simulations of two IAPPs and two Aβs respectively (i.e., self-association). We carry out 20 independent simulations at 300K with each lasted 600ns for each molecular system, and the last 300ns trajectories are used to compute the residue-wise binding frequency maps (Fig. 2-3). From simulations of IAPP-Aβ cross-association, we identify several "hot regions" with high binding frequencies, including residues 8-18 and 22-28 in IAPP, as well as residues 17-24 and 27-42 in Aβ, (Fig. 2-3A). Same regions are also important for the self-associations of IAPP and Aβ (Fig. 2-3B&C). Besides, shared features can be observed between cross- and self-associations. For instance, an "anti-parallel" binding pattern (i.e., perpendicular to the diagonal) due to interactions between C-terminal residues of Aβ is present in both IAPP-Aβ and Aβ-Aβ contact frequency maps (Fig. 2-3A&B). Similar patterns formed by the hot-spot residues of IAPP (e.g., 8-18 and 22-28) could also be found in both IAPP-Aβ and IAPP-IAPP maps (Fig. 2-3A&C). Our observations agree very well with previous experimental reports, in which the hot regions for cross- and self-associations are determined as residues 8-18, 22-28 in IAPP, and residues 19-22, 27-32, 35-40 in Aβ.[59]

These similarities suggest a common binding mechanism in cross- and self-associations of IAPP and Aβ, which may arise from their similarity in sequences.[62–64] Both IAPP and Aβ are amyloidogenic with about 50% similarity in sequences, and the sequences with the highest degree of similarity are 10-16, 21-27 in IAPP and 15-21, 26-32 in Aβ (Fig. 2-3D), all of which are within or close to the hot regions determined both experimentally and computationally. Therefore, the regions important for both IAPP and Aβ self-associations also mediate their cross-association, and their cross- and self-associations could occur in a competitive manner.

Conformational changes of IAPP and Aβ heterodimer upon cross-association. We further study the structural properties of IAPP-Aβ heterodimer. For comparison, we also perform simulations of IAPP and Aβ monomers and dimers, following the same protocol - i.e., 20 independent simulations of 600ns at 300K, with trajectories of the last 300ns are used to compute the secondary structure propensities (Fig. 2-4 and Fig. 2-5). For the Aβ monomer, the amyloidogenic region (Aβ16-22) is partially helical, while the N- and C-termini mostly adopt β-sheet conformation (Fig. 2-4A&B). IAPP monomer contains a stable helix in the N-terminus, with the amyloidogenic IAPP22-29 mostly unstructured with a weak helical propensity (Fig. 2-4C&D and Fig. 2-5C&D). Compared to monomers, both IAPP and Aβ homodimers show an overall increase of α-helix (Fig. 2-4A&C), consistent with many experimental observations of the increased α-helical contents during early stage of amyloid aggregation of IAPP and Aβ before the final conversion to β-rich fibrils.[65,66] In contrast, the heterodimer has the β-sheet propensity increased while helix propensity decreased for

both peptides compared to their monomers, especially in the corresponding amyloidogenic regions (e.g., IAPP22-29 and Aβ16-22 in Fig. 2-4). Given the importance of these amyloidogenic regions in forming the cross-β architecture in the mature amyloid fibrils, the conformational transition form α-helix to β-sheet in these regions makes the peptides more aggregation prone upon their cross-association.[67]

Helix unfolding of Aβ16-22 is the major conformational change upon binding with IAPP in the heterodimer. To better understand the conformational dynamics of IAPP and Aβ upon association as the heterodimer, we further analyze the simulation trajectories of the monomers and the heterodimer by focusing on their corresponding amyloidogenic regions. Following a similar approach in protein folding studies, we monitor the folding and unfolding of helixes in the amyloidogenic regions - i.e., IAPP22-29 and Aβ16-22.[68,69] During simulations of Aβ monomer, we could observe the dynamics of helix unfolding and refolding of the amyloidogenic Aβ16-22 (e.g., 22 unfolding and 9 refolding events), where the population of the helical state was approximately 61% (Fig. 2-6). In the presence of IAPP, the number of helix refolding events is drastically reduced (e.g., 18 unfolding and only 1 refolding events) and the population of the helical state is reduced to ~57%. In terms of IAPP22-29, the helix population is slightly changed from ~21% in monomer to ~20% in heterodimer, and the helix unfolding/refolding dynamics in heterodimer is slower but still frequent (i.e., from 72/56 to 34/18). These observations indicate that the binding between IAPP and Aβ in the heterodimer increases the free energy barriers of helix unfolding/refolding of their corresponding amyloidogenic regions. For IAPP22-29, the

barrier increase doesn't change the equilibrium between helical and non-helical conformations, and the frequent unfolding/refolding dynamics suggests that our computational observations are significant. The conformation dynamics of Aβ16-22, on the other hand, is shifted towards the non-helical state upon binding with IAPP. With the rare observation of helix refolding events of Aβ16-22 suggesting a slow conformational dynamics, the conformational equilibrium might not have been reached in our constant temperature simulations (e.g., up to 600ns in each independent simulation).

In order to better sample the conformational equilibrium of the heterodimer, we apply replica exchange DMD (REXDMD) simulations, where parallel simulations at different temperatures are performed with Monte-Carlo based periodic exchanges between replicas of neighboring temperatures.[70] Although the interpretation of kinetics might be challenging compared to serial ones at constant temperatures, replica exchange simulations have been widely applied for enhanced sampling of thermodynamic equilibrium by overcoming energy barriers at high temperatures. We perform REXDMD simulations for IAPP monomer, Aβ monomer, and the heterodimer, with each replica of simulations lasted 200ns and trajectories of the last 150ns are used in data analysis. Using the weighted histogram analysis method (WHAM), we compute the specific heat (C_v) as the function of temperature (Fig. 2-7A).[71] A peak in the C_v plot usually corresponds to conformational transitions around the temperature with the heights indicating the transition cooperativity. To uncover the details of conformational transitions, we also compute the temperature dependence of the number of inter-peptide contacts in the heterodimer (Fig. 2-7B) and secondary structure contents of both Aβ and IAPP in monomers and heterodimer

simulations (Fig. 2-7C&D). The weak C_v peak of IAPP around ~305K corresponds to the gradual and non-cooperative unfolding of helixes (Fig. 2-7A&D), while the peak of Aβ at a higher temperature (~325K) results from unfolding of both helices and strands (Fig. 2-7A&C). Remarkably, the heterodimer displays a high C_v peak around ~322K mainly due to the dissociation of a large number of inter-peptide contacts (Fig. 2-7B). Compared to the monomers, the strong inter-peptide binding in the heterodimer significantly reduces the helical content of Aβ (mainly in the amyloidogenic region of Aβ16-22) and increases its β-sheet content (Fig. 2-7C). For IAPP, Aβ binding does not significantly change the conformational dynamics with only a slight increase of the β-sheet content (Fig. 2-7D). Therefore, our REXDMD simulations confirms the IAPP-binding induced helix unfolding of Aβ16-22 as observed in constant temperature simulations (Fig. 2-4 and Fig. 2-6).

To better characterize the conformational change of Aβ16-22 upon IAPP binding, we further compute the potential mean force (PMF, i.e., the effective free energy landscapes) of the fragment with respect to the number of residues in helical content and the end-to-end distance at 300K based on our REXDMD simulation results (Fig. 2-8). For both monomer and heterodimer, four major basins could be observed, corresponding to helical, partially helical and non-helical states with either compact or extended conformations (e.g., typical snapshot structures in Fig. 2-8). The partially unfolded state corresponds to the intermediate of helix unfolding and the saddles connecting basins denote the folding pathways. Compared to Aβ16-22 in the monomer, the binding with IAPP renders the non-helical basins deeper, the helical and partially helical states shallower, and the saddle between the non-helical and the intermediate states broadened. Therefore, our

results suggest that binding with IAPP in the heterodimer at 300K shifts the conformational equilibrium of Aβ16-22 from helix towards extended non-helical conformational states, readily to form β-sheets (e.g., the snapshots in Fig. 2-8).

In vitro studies of IAPP and Aβ self- and cross-aggregation. We apply the ThT fluorescence assay to study the self- and cross-aggregation of IAPP and Aβ. Mixtures of IAPP and Aβ42 at equimolar ratio with different concentrations are tested (1.0, 2.0, 2.5, 3.0, 3.5, 4.0, and 5.0μM accordingly) and compared with control groups of individual peptides aggregating at the same concentrations. Multiple repeats are done for each molecular system at a given concentration. Sigmoidal aggregation kinetics has been observed in all peptide systems (e.g., Fig. 2-9), and the corresponding lag time and fibril elongation rate are obtained by fitting the data with an empirical sigmoidal function (Fig. 2-10A&B). Our results are consistent with previous experimental reports that IAPP is more aggregation prone than Aβ with shorter lag phases for all the tested concentrations.[30,72] The lag time of the mixture is comparable to that of the IAPP alone and significantly reduced compared to Aβ alone, consistent with previous report that mixing of IAPP and Aβ retards the rate of IAPP assembly while enhances that of fibril formation by Aβ.[38] Similarly, IAPP has higher aggregation elongation rates than Aβ at the same concentrations and the mixture has the corresponding values in between (Fig. 2-10B).

Based on a nucleated polymerization mechanism, the Wetzel group proposed an aggregation kinetics analysis approach to determine the critical number of monomers, n^*, the conformational changes of which are rate-limiting for aggregation.[9,10] Briefly, during

the initial growth phase before the rapid elongation, the increase of aggregation linearly depends on the square of time, t^2, and the slope is the power function of peptide concentration with the exponent index corresponding to n^*+2. Given the fast aggregation of IAPP and IAPP-Aβ mixture and the resulting limited number of data points with high noise-to-signal ratio for detailed analysis of the initial phases, we only apply the above analysis to the aggregation of Aβ. We select data corresponding to the initial phase of Aβ aggregation, and estimate the amount of aggregates based on the ThT fluorescence intensity signal. For each concentration, we determine the slope with respect to t^2 (e.g., Fig. 2-10C). Based on the log-log plot of the slopes vs. concentrations (Fig. 2-10D), we obtain the exponent of ~3.5 and thus the value of n^* ~1.5.

Many previous experiments have reported the observation of Aβ oligomers such as pentamers and hexamers during the initial phase of amyloid aggregation.[73] Here, our aggregation kinetics analysis reveals that the rate-limiting step of Aβ42 aggregation requires the conformational changes of approximately 2 peptides, which can take place within the initially formed Aβ oligomers. Based on our simulation results, these rate-limiting conformational changes correspond to the unfolding of α-helix in Aβ16-22. The relatively slow aggregation of Aβ42 observed *in vitro* might result from the stabilization of the helical conformation in Aβ16-22 in the self-associated oligomers such as homodimers (Fig. 2-4). Upon binding with IAPP in the mixture, the strong inter-peptide interactions shift the conformational equilibrium of Aβ16-22 from helical to the extended conformation (Fig. 2-8), which in turn reduce the aggregation free energy barrier as in the isolated Aβ peptides and thus shorten the aggregation lag time (Fig. 2-10).

Conclusion

Combining all-atom DMD simulations with the complementary ThT assay, we investigate the molecular mechanism for the accelerated co-aggregation of IAPP and Aβ42 mixture compared to the self-aggregation of Aβ alone. Our simulation results suggest that the formation of IAPP-Aβ heterodimer is the first step towards their co-aggregation due to electrostatic attraction between the two peptides with opposite net charges. The computationally determined residue-wise inter-peptide interactions between IAPP and Aβ in the heterodimer agree very well with previous experimental results of the hotspot regions for their cross-association. Detailed analysis of our serial simulations at constant temperature and replica exchange simulations at multiple temperatures reveal that the strong inter-peptide interactions in the heterodimer introduce the unfolding of helix in the amyloidogenic region of Aβ16-22, which makes Aβ ready for aggregation. The helix of Aβ16-22 is otherwise stabilized in the homodimer of Aβ42, consistent with the experimentally observed accumulation of helical contents before the rapid conversion into β-rich aggregates.[65,66]

Our ThT experiments confirm previous experimental reports that the lag phase of IAPP and Aβ co-aggregation is shorter than that of Aβ alone but only slightly longer than IAPP. The kinetics analysis based on the nucleated growth polymerization theory indicates that the critical number of peptides, whose conformational change is the rate-limit step for aggregation, is approximately 2. With experimental observations of various Aβ42 oligomers and the in-registered β-sheet structures of Aβ16-22 in the core of Aβ42 amyloid

fibrils, our combined computational and experimental studies suggest that the nucleation of fibrillization corresponds to the helix unfolding of central hydrophobic cores (i.e., 16-22) of approximately two peptides in these oligomers and the subsequent formation of inter-peptide β-sheets in this region.[67] Therefore, the binding of IAPP with Aβ in the mixture reduces the free energy barrier for Aβ aggregation - i.e., the helix unfolding of the central hydrophobic core of Aβ16-22, and thus promotes the co-aggregation with reduced lag time for aggregation nucleation. With experimental evidences of IAPP being able to cross the blood-brain barrier, the overproduction of IAPP in T2D, known as the hyperamylinemia, may result into increased IAPP concentration in the brain, which in turn promotes the formation of toxic aggregates with Aβ42 and increases the risk of AD.[34]

Materials and Methods

DMD simulations. DMD is a special flavor of MD algorithm with high computational efficiency and predictive power, which has been extensively used by our group and others to study protein folding, protein dynamics, and amyloid aggregation.[74–76] In DMD, discrete step functions instead of continuous potentials are used to model inter-atomic interactions. The step-function potentials are adapted from the continuous Medusa force field to model inter-atomic interactions.[77] The non-bonded inter-atomic interactions include van der Waals (VDW), solvation, hydrogen bond and electrostatic terms. The VDW parameters were adopted from the CHARMM force filed and the EEF1 implicit solvent model is used to model the solvation term.[78,79] The hydrogen bond interactions are implicitly modeled with a reaction-like approach.[80] The Debye-Hückel approximation is applied to model the

screened electrostatic interactions with the Debye length assigned ~10Å. We use the Anderson's thermostat to maintain the temperature, which is fixed at 300K except for the replica exchange simulations.[81] To ensure sufficient sampling and avoid potential bias arise from starting configurations, we perform multiple independent simulations for each molecular system with different initial conditions, including randomized velocities, intermolecular distances and orientations.

Simulation setup. In all simulations, we use the IAPP (PDB ID: 2L86) and Aβ42 (PDB ID: 1Z0Q) structures obtained from PDB to construct our systems. Counter ions Cl^- and Na^+ are also introduced into systems to achieve a neutral charge condition if necessary. For both IAPP and Aβ peptides, we maintain the peptide concentration same as that of a single peptide in a cubic box with the dimension of 83Å in all simulations. The periodic boundary condition is used. In replica exchange simulations for IAPP and Aβ monomers, five replicas are running at 275, 295, 315, 335, and 355K respectively, while eight replicas running at 275, 290, 300, 310, 320, 330, 340, and 355K are performed to model the heterodimer. The temperatures are chosen to ensure that the simulation exchange rates are between 30% to 70%. During the analysis of simulation trajectories, we use the DSSP program to compute protein secondary structures, and the weighted histogram analysis method (WHAM) to evaluate the temperature dependence of thermodynamic quantities.[71,82]

Folding/Unfolding analysis. For the characterization of helix unfolding and refolding, we based on two criterions: a helical to non-helical state conversion is considered if a structure contains at least five helical residues inside amyloidogenic region converts into one contains no more than two helical residues, and the conversion would be determined as valid and recorded only if the new state could last for no less than 0.5ns simulation time. Non-helical to helical state conversion is identified in a similar way. Structural percentage and the number of conformational change are recorded according to all simulation trajectories.

Calculation of the potential mean force (PMF). The two-dimensional PMF (or effective free energy) is computed according to

$$PMF = -K_B T \ ln \ P(N_{helical}, D_{end\text{-}to\text{-}end}), \qquad (2\text{-}1)$$

where K_B is the Boltzmann constant, T corresponds to the simulation temperature 300K, and $P(N_{helical}, D_{end\text{-}to\text{-}end})$ is the probability of finding a Aβ16-22 segment containing $N_{helical}$ helical residues, with an end-to-end distance of $D_{end\text{-}to\text{-}end}$ at the time.

Thioflavin-T Fluorescence Assay. To study the kinetics of IAPP and Aβ42 amyloid fibrils formation *in vitro*, our collaborators apply the ThT assay and single compound samples or 1:1 mixtures of concentrations from 1 to 5μM have been tested. All kinetic measurements are performed at least in triplicate. The fluorescent ThT data are fitted to an empirical equation to reproduce the change of fluorescent intensity ThT upon binding to the amyloid

fibrils (I_{max}-I_0), the apparent rate constant for fibrillization (k), and the lag time ($t_{lag}=t_0-2/k$) to represent the time of nucleation before detectable amyloid formation:

$$I(t) = I_0 + \frac{I_{max}-I_0}{1+e^{-(t-t_0)k}}, \qquad (2\text{-}2)$$

where I, I_0 and I_{max} are the reading, initial and maximum fluorescence values, t_0 is the time required to reach half change of intensity.

Nucleation Kinetics. The details describing the nucleated growth polymerization mechanism could be found elsewhere.[9,10] The important kinetics feature of the initial phase of aggregation we examined here is the linear dependence of the aggregation content on the time square (t^2), and the power-law dependence of the corresponding slope on the peptide concentration. The exponent index corresponds to n^*+2, where n^* is the critical number of peptides whose conformational changes are the rate-limiting step for aggregation nucleation. By fitting the ThT assay data with the sigmoidal equation (Eq. 2-2), we choose the initial phase with $t<t_{lag}$ and estimate the amount of aggregation by normalizing them based on concentration conditions, $\rho(I-I_0)/I_{max}$, with ρ corresponding to the total peptide concentration.

CHAPTER THREE

Zinc-coordination and C-peptide Complexation: A Potential Mechanism for the Endogenous Inhibition of IAPP Aggregation

Introduction

The observation that IAPPs are stored inside β-cell granules at mM concentrations for hours without apparent aggregation in healthy individuals suggests a mechanism of endogenous inhibition of IAPP aggregation from the physiological environment inside β-cell granules. Previous studies offer a comprehensive molecular insight into the intermolecular binding between insulin and IAPP and uncover the corresponding inhibition mechanism of IAPP aggregation.[52–54] However, since IAPPs are found almost exclusively in the soluble halo fraction of β-cell granules while insulin is mostly insoluble in the core, the insulin-IAPP interaction is limited and therefore a balance of Zn^{2+} and C-peptide co-localized with IAPP appears crucial for maintaining the native state of IAPP.[48] It has been explored that Zn^{2+} has a concentration-dependent effect on IAPP aggregation, while C-peptide is found to promote IAPP aggregation *in vitro*.[47–49] Hence, we postulate that the cooperative effect of Zn^{2+} and C-peptide rather than individual molecules may be responsible for the endogenous inhibition of IAPP aggregation. In this study, we apply DMD simulations to examine the effects of C-peptide and its coordination with Zn^{2+} on IAPP aggregation. The 31-residue C-peptide contains five acidic amino acids, which contribute to Zn^{2+} coordination of the peptide at a 1:1 stoichiometry.[55,83] Our DMD simulations show that a Zn^{2+} coordinated heterotrimer with two IAPPs and one C-peptide

forms a well-defined stable molecular complex, which stabilizes IAPP in an aggregation-incompetent helical conformation to inhibit the formation of β-rich aggregates. Further ThT fluorescence assay and high-resolution transmission electron microscopy (TEM) imaging validate our computational predictions, and reveal the maximum inhibition of IAPP aggregation occurs at ~2.7:1:1 IAPP/C-peptide/Zn^{2+} molar ratio *in vitro*. Together, our study suggests that the Zn^{2+} coordinated IAPP and C-peptide complexation plays a critical role in the endogenous inhibition of IAPP aggregation inside β-cell granules.

Results and Discussion

Effects of C-peptide on IAPP self-association. We first simulate the dimerization of IAPP at 300K with and without the presence of C-peptide to evaluate the effect of C-peptide on IAPP self-association. For both molecular systems, 100 independent simulations are carried out with each lasted 50ns, and the IAPP concentration is maintained the same. Our simulation results reveal the accelerated dimerization of IAPP with the presence of C-peptide, which is in agreement with experimental observations (Fig. 3-1). By fitting the trajectories of binding probability exponentially, we obtain the aggregation rates as 0.052 ns^{-1} for simulations with C-peptide and 0.029 ns^{-1} for simulations of IAPPs alone respectively, while their saturations are comparable. Further examination shows that C-peptide binding doesn't affect the secondary and quaternary structures of the IAPP dimeric aggregates (Fig. 3-2). In both systems, IAPP adopts an N-terminal α-helix and a small β-strand region around residue H18, with the whole peptide mostly unstructured. The residue-wise binding frequency maps for both systems also share similar patterns, where

L12, F15, L16, and F23 are highly engaged in IAPP self-association. Taken together, our simulations suggest C-peptide could accelerate IAPP aggregation but exert little influence on the structure of IAPP dimeric aggregates. This effect likely originated from electrostatic attractions, as the net charge of IAPP is +2e (K1 and R11) while it is -5e for C-peptide (E1, E3, D4, E11, and E27). The long-range electrostatic attractions induce a high local concentration of IAPP to trigger their aggregation, while those highly engaged residues in IAPP self-association are neutral and available for IAPP binding.

The corporative effect of Zn^{2+} and C-peptide on IAPP aggregation. It has been experimentally shown that Zn^{2+} binds C-peptide at a 1:1 stoichiometry, we therefore study the corporative effect of Zn^{2+} and C-peptide on IAPP aggregation with various molar ratios.

We simulate Zn^{2+}, C-peptide, and IAPP at a 1:1:1 ratio first, with 100 independent simulations and each performed for 50ns. Through our simulations, we observe Zn^{2+} binds C-peptide more rapidly than its binding with IAPP and eventually the formation of a heterodimer (Fig. 3-3A). After 50ns of simulation, the binding probability of Zn^{2+} with C-peptide approaches 1, while the binding of Zn^{2+} with IAPP is only observed in 40% of the final structures. The differential binding kinetics is possibly due to different driving forces. C-peptide has five charged acidic residues all contributing to Zn^{2+} binding with a longer interaction range and larger binding cross section, while the zinc-binding H18 on IAPP is neutral with a shorter interaction range and smaller binding cross section. Our analysis reveals that Zn^{2+} binds preferentially to the three N-terminal acidic residues of C-peptide due to their mutual proximity (Fig. 3-3B&C).

Since the coordination valence of Zn^{2+} is up to six and Zn^{2+} in the heterodimer obtained above is still solvent exposed (Fig. 3-4A), it's possible for Zn^{2+} to coordinate additional molecules. Given that Zn^{2+} binds C-peptide at 1:1 stoichiometry while each Zn^{2+} already coordinates with at least three N-terminal acidic residues of C-peptide in the heterodimer, we anticipate further coordination of Zn^{2+} with additional IAPPs instead of C-peptides to form higher-order complexes. We also perform DMD simulations with one Zn^{2+}, one C-peptide, and up to three IAPPs. With two IAPPs, the Zn^{2+} is already fully buried, preventing further coordination with additional IAPPs (Fig. 3-4B). Therefore, our simulations suggest that each Zn^{2+} and C-peptide pair could coordinate up to two IAPPs, forming a heterodimer or a heterotrimer.

We find the heterotrimer has a significantly stronger energy gain upon complexation than the heterodimer, suggesting a higher thermodynamic stability (Fig. 3-5A). Secondary structure contents information reveals that the N-terminal IAPP6–15 and the amyloidogenic region IAPP21–30 adopt helical structures in both complexes, while the heterotrimer is significantly more helical (Fig. 3-5B). Moreover, the structural ensemble of the heterodimer is diverse with a high number of representative structures (e.g., the top ten centroid structures with clustering analysis in Fig. 3-6), suggesting a high structure flexibility. Contrarily, heterotrimer structures are well-defined (e.g., three lowest energy representative structures from clustering analysis in Fig. 3-5C), where each IAPP features two helixes and separated by the C-peptide. Since the formation of inter-peptide hydrogen bonds especially between the amyloidogenic regions is important for amyloid fibrillization,

the heterotrimer with stable helixes in the amyloidogenic region is likely aggregation-incompetent.

The nucleation propensity of both heterodimer and heterotrimer are evaluated *in silico* by testing whether the IAPPs in the complexes can form further inter-peptide hydrogen bonds with an additional IAPP. For the heterodimer, the binding between its IAPP and the incoming one is similar to that of two IAPP alone, with extensive contacts and hydrogen bonds formed (Fig. 3-7A). In contrast, IAPPs in the heterotrimer may still associate with the incoming IAPP via dynamic binding, but they don't form many contacts or inter-peptide hydrogen bonds (Fig. 3-7B). Together, our simulation results suggest that the formation of zinc-coordinated hetero-complexes between IAPP and C-peptide, especially the stable heterotrimer instead of the intermediate heterodimer, stabilizes IAPP in a helical and aggregation-incompetent state, which may play an important role in the endogenous inhibition of IAPP aggregation.

In vitro studies of the effect of Zn^{2+} and C-peptide on IAPP aggregation. To validate our computational predictions, our collaborators apply multiple *in vitro* studies including ThT fluorescence assay, TEM imaging, and CD spectroscopy to examine the effect of Zn^{2+} and C-peptide on IAPP aggregation.

Using a ThT fluorescence kinetic assay, we observe that in the presence of Zn^{2+}, C-peptide, or both Zn^{2+} and C-peptide at 1:1 stoichiometry, IAPP fibrillization is increased or comparable with the control of IAPP alone after 14h incubation, except for the molar ratios of 2.7:1:1 of IAPP/C-peptide/Zn^{2+} where IAPP fibrillization has been markedly

decreased and its lag phase increased compared to the IAPP control (Fig. 3-8A and Fig. 3-9). Specifically, the ThT fluorescence intensity is increased at IAPP/C-peptide/Zn^{2+} molar ratios of 0.3:1:1 and 0.7:1:1, and comparable to that for IAPP alone at molar ratios of 1.3:1:1 and 5.3:1:1.

High-resolution transmission electron microscopy (TEM) imaging provides direct visualization of IAPP fibrillization and morphology. Consistently with the ThT assay for 14h of incubation, TEM imaging reveals the formation of fibrils and aggregates at IAPP/C-peptide/Zn^{2+} molar ratios of 0.3:1:1, 0.7:1:1, 1.3:1:1, and 5.3:1:1 (Fig. 3-10). In contrast, we do not observe conventional fibrillar structures but the presence of small aggregates of 8.4±2.7nm in size at IAPP/C-peptide/Zn^{2+} molar ratios of 2.7:1:1 (10× magnification in Fig. 3-8B). Statistical analysis indicates that these aggregates are much softer (λ~187 nm, Fig. 3-8C) than those of the IAPP control (λ~2885nm), confirming their amorphous and non-fibrillar characteristics. IAPP fibrillization is persistent for IAPP/C-peptide of all tested molar ratios from 0.3:1 to 5.3:1 (Fig. 3-8B and Fig. 3-10), while fibril softening occurs also for all conditions (Fig. 3-8C). In addition, 24h incubation of IAPP with Zn^{2+} either enhances or inhibits IAPP fibrillization according to TEM imaging (Fig. 3-8B and Fig. 3-10M–Q), although 14h incubation with Zn^{2+} causes modest IAPP fibrillization inhibition in the ThT assay (Fig. 3-8A). Here, the observed concentration-dependence for Zn^{2+} on IAPP aggregation is consistent with our previous studies. The experimentally observed 2.7:1 ratio with maximum aggregation inhibition is close to the predicted 2:1 molar ratio between IAPP and C-peptide in the aggregation-incompetent heterotrimer (Fig. 3-5 and Fig. 3-8).

Circular dichroism (CD) spectroscopy is utilized to assess the effects of Zn^{2+}/C-peptide on the secondary structures of IAPP at different molar ratios (Fig. 3-11). The IAPP control shows a significant increase of β-sheet content from 32% and 77% coupled with a drastic decrease in random coil, indicating IAPP aggregation after 24h incubation. 24h incubation of IAPP/C-peptide/Zn^{2+} at 0.7:1:1, 1.3:1:1, 2.0:1:1 and 2.7:1:1 ratios yield significant reductions in the β-sheet content and overall increases in turns and random coils. Specifically, IAPP/C-peptide/Zn^{2+} at the molar ratio of 2.7:1:1 exhibits a marked decrease from 77% and 34% in β-sheets along with an increase of α-helix from 19% to 25% and turns from 4% to 40%, displaying a non-fibrillar characteristics. Such contrasting conformational changes of IAPP at different IAPP/C-peptide/Zn^{2+} molar ratios are consistent with the ThT and TEM results. Most importantly, the increase of helical content at the 2.7:1:1 molar ratio agrees with the simulation predicted formation of stable α-helix in the IAPP amyloidogenic region upon zinc-coordinated C-peptide complexation. At lower IAPP to Zn^{2+}/C-peptide molecular ratios, the unstructured C-peptides in the solution results in the reduced overall helical content and increased coil content (Fig. 3-11B). Therefore, our complementary biophysical experiments offer compelling evidence for the predicted IAPP stabilization via zinc-coordinated complexation with C-peptide.

We also perform a cell viability assay to assess the differential cytotoxicity of the various molecular species to insulin-secreting NIT-1 mouse pancreatic β-cell line. After 24h incubation, the cells are exposed to DNA binding dyes Hoechst 33342 and propidium iodide. Hoechst 33342 freely diffuses into cells with preserved membranes, staining DNA blue. Propidium iodide is permeable to compromised cell membranes, staining DNA of

dead cells red. Thus, viable cells are identified by their intact nuclei with blue fluorescence, whereas cell death is quantified by blue-red fluorescence or by fragmented blue nuclei with immunofluorescence and light microscopy. We find that the controls of C-peptide and Zn^{2+} induce little toxicity (＜0.7%＝ in NIT-1 cells after 24h of treatment, while the controls of IAPP and IAPP/Zn^{2+} (2.7:1) cause significant cell death at 22.2±6.5% and 30.3±8.1%, respectively (Fig. 3-12). The sample of IAPP/C-peptide (2.7:1) induce minor toxicity (~1.8%). In contrast, IAPP/C-peptide/Zn^{2+} at 2.7:1:1 molar ratio elicits minimal cytotoxicity of ~1.1±0.2%, indicating remarkable mitigation of IAPP toxicity through zinc-coordinated IAPP/C-peptide complexation. These *in vitro* results vindicate *in silico* prediction as well as ThT, TEM, and CD observations.

Conclusion

In summary, the zinc-coordinated heterotrimer with one C-peptide and two IAPPs is both thermodynamically and structurally stable, further with the amyloidogenic region of IAPP stabilized in helical structure and the complex is suggested as aggregation-incompetent. IAPP/C-peptide/Zn^{2+} mixture at 2.7:1:1 molecular ratio significantly reduces the cytotoxicity of IAPP. In light of the coexistence of high concentrations of zinc, C-peptide, and IAPP inside β-cell granules, this study suggests that zinc-coordinated complexation between IAPP and C-peptide may play an important role in the endogenous inhibition of IAPP aggregation in addition to the reported low pH effect. With future *in vivo* verifications and structural characterizations of the molecular complex, therapeutic

approaches mimicking or promoting such zinc-coordinated molecular complexes may prove potent for the mitigation of aggregation-induced β-cell death in T2D.

Materials and Methods

DMD simulations. We apply all atom DMD simulations to study the effects of C-peptide and Zn^{2+} coordinated complexation on IAPP aggregation. Our simulations are performed under the same protocol as that introduced in chapter two.

Modeling zinc-coordination. The bindings between zinc and residues H18 on IAPP, D and E on C-peptide are modeled by a number of constraints with a series of square well functions. The interaction parameters are obtained by statistical analysis of all available structures containing Zn^{2+} in the protein databank (PDB). To capture the distance and angular dependence of zinc coordination, we compute the interatomic distances between zinc and all atoms in the associated chemical groups, including imidazole of histidine and carboxyl of aspartic (Asp) and glutamic (Glu) acids. Since the adjacent carbons (i.e., the CB atom in aspartic acid and the CG atom in glutamic acid) are coplanar to carboxyl groups, we also include their distances to the coordinated zinc. Based on the histograms of interatomic distances, we determine the lower bound and upper bound values to assign the coordination interactions. More details can be find elsewhere.[84]

Simulation setup. In all simulations, we use the IAPP (PDB ID: 2L86) and C-peptide (PDB ID:1T0C) structures obtained from PDB. To maintain the same IAPP peptide concentration,

cubic boxes with the dimension of 100Å, 126Å and 144Å are used to model 1, 2, and 3 IAPPs, respectively. For simulations to obtain the binding kinetics (such as modeling the effect of C-peptide alone on IAPP aggregation, and the binding of zinc/C-peptide/IAPP at 1:1:1 molecular ratio) and the modeling of zinc-coordinated IAPP and C-peptide complexation, 100 independent simulations with different initial conditions are performed to acquire sufficient samplings. For the nucleation test, 10 independent simulations for each representative molecular complex are performed in parallel. Counter ions including Cl^- and Na^+ are added to neutralize the systems if necessary. In addition, no coordination interaction has been assigned between Zn^{2+} and the histidine of incoming IAPP in the nucleation tests for both the heterodimer and heterotrimer.

Clustering Analysis. For the structural ensembles of both the heterodimer and heterotrimer, we perform the clustering analysis using a hierarchical clustering program, oc (www.compbio.dundee.ac.uk/downloads/oc). The clustering analysis is based on the calculation of root-mean-square-deviation (RMSD) between two structures. Given the two IAPP are indistinguishable in the heterotrimer, we perform structural alignment twice by alternating the index of the two IAPPs and use the small RMSD value for any two structures. For the clustering of the heterodimer, we set the cutoff value as 6Å and all low energy structures are grouped into 10 large clusters (shown in Fig. 3-6) and 256 small ones with one or two structures. We use the centroid node of the top 10 largest clusters for the nucleation test. Given the larger size of the heterotrimer, we find a cutoff of 8Å is able to effectively distinguish different structures, ending with 7 clusters. Compared to the

heterodimer, the heterotrimer has significantly smaller structural variations. To further improve our structural sampling of the heterotrimer, we apply 7 replica exchange DMD (RXDMD) simulations with each of the centroid structure as the starting configuration. In all simulations, the coordination interactions are maintained. Based on simulation trajectories from all replica runs, we select again the low energy states, with potential energy one standard deviation bellow the lowest Gaussian-like peak in the histogram. Similar clustering analysis results into only 3 clusters with similar over-all structural features as in Fig. 3-5C.

Materials. Human IAPP and C-peptide are obtained as lyophilized powders from AnaSpec. Zinc chloride and ThT kit are acquired from Sigma-Aldrich. Milli-Q water has been used for all dilutions.

In vitro studies. To validate our computational predictions, our collaborators apply multiple *in vitro* studies including ThT assay, high-resolution TEM imaging, CD spectroscopy and cell viability assay. Details can be found elsewhere in our publication.[84]

CHAPTER FOUR

IAPP Amyloid Inhibition by Small Molecules

Introduction

Some naturally occurring small molecules such as curcumin, resveratrol, and epigallocatechin-3-gallate (EGCG) have shown potency in directing the progression of Aβ, α-synuclein, IAPP, prions, and cystatin amyloids towards disordered and amorphous aggregates.[85–96] Among the above small molecules, EGCG is unique due to its better water solubility and a high capability of remodeling amyloid fibrils.[97] Previous studies reveal EGCG inhibit IAPP amyloids and against IAPP-associated toxicity by trapping IAPP into an early intermediate state prior to IAPP amyloid formation.[98] EGCG could also remodel IAPP amyloid fibrils, but couldn't fully resolubilize them back to monomers, suggesting IAPP fibrillization and EGCG remodeling are irreversible processes.[58] In this study, we combine transmission electron microscopy (TEM), atomic force microscopy (AFM), and DMD simulations to extract nanoscale information on IAPP inhibition by fresh, autoxidized, or glutathione (GSH)-reduced EGCG. We systematically analyze the persistence length, contour length, as well as the morphology of IAPP and IAPP-EGCG products versus time, and also reveal the molecular details of EGCG interacting with soluble IAPP using DMD simulations. The nanoscale information uncovered by this study has filled a knowledge gap between the atomic- and cellular-level understanding of IAPP amyloidogenesis and mitigation against T2D.

Results and Discussion

Nanoscale IAPP interfacing with EGCG. Our collaborators apply multiple experimental studies to investigate the interaction between IAPP with different EGCG species and also the inhibition effect. TEM imaging is the first applied, and reveals IAPP fibrillization in the presence of EGCG and its derivatives. The selection of 1, 6, and 24h of fibrillization is intended to cover the nucleation, end of elongation, and saturation phases respectively (Fig. 4-1C-N). IAPP seeds and protofibrils (30–200nm) start to emerge after 1h for IAPP alone and IAPP with fresh, oxidized, or GSH-reduced EGCG. In the presence of EGCG, the protofibrils appear amorphous with multiple splitting branches, differing from the linear contours of the IAPP control. After 6h, IAPP forms long fibrils with a broad contour length distribution (160–17400nm, as shown in Fig. 4-2A). Whereas all EGCG species yield short and ramified fibrils (Fig. 4-1G&J&M and Fig. 4-2B-D). Fibrillization inhibition is achieved with fresh EGCG at 6h (65–330nm; Fig. 4-1G and Fig. 4-2B), whereas oxidized EGCG renders longer fibrils (40–1125nm; Fig. 4-1J and Fig 4-2C). At 24h, IAPP length distribution is further broadened (60–20600nm; Fig. 4-2A), and all samples display polymorphisms of long fibrils alongside short, soft, and curvy fibrils/protofibrils, suggesting the coexistence of amyloid and non-amyloid fibrils. Further analysis reveals that long IAPP fibrils are 7.9±0.9nm in thickness, whereas short ones are 9.8±2.5nm in thickness with more pronounced variations due to their amorphous nature (Fig. 4-1E, inset). In addition, short fibrils re-emerge at 24h, departing from the log-normal distribution of such aggregation processes and corroborating the possibility of multiple fibrillation rates for IAPP (Fig. 4-2A, grey circle). No small fibrils are observed after one month.

As a result, fresh, autoxidized, and GSH-reduced EGCG could inhibit IAPP fibrillization up to 6h, while small fibrils can be observed at 24h for all three cases (Fig. 4-2B-D, grey circles). We also find fresh EGCG exerts stronger inhibition than oxidized EGCG up to 6h. At 24h, both fresh and oxidized EGCG display similar length distributions, which is likely due to the gradual oxidation of fresh EGCG. With GSH-reduced EGCG, shorter and fewer IAPP fibrils are observed than with other EGCG species, which is confirmed by a narrower length distribution of the contour length (Fig. 4-2D). Persistence length (λ) analysis using FiberApp also reveals three distinct fibril species with reduced EGCG, whereas the other samples display the formation of two different species—long and rigid fibrils along with short and soft fibrils or amorphous aggregates (Fig. 4-2E). Accordingly, after 24h in the presence of fresh, oxidized, or GSH-reduced EGCG species, the β-sheet content of IAPP is reduced from 39.2% to 34.3%, 35.7%, and 32.9%, respectively, while the unstructured content enhanced from 37.3%, as seen in the IAPP control, to 49.7%, 47.3%, and 51.7%, respectively (Fig. 4-2F and Fig. 4-3).

Molecular details of IAPP interfacing EGCG. To further provide the molecular insight of IAPP interfacing with EGCG, we perform all-atom DMD simulations of 1, 2, 4, 6, and 8 IAPP peptides in the presence of EGCG (ligand) at equimolar ratio, with IAPP concentration maintained the same. In all systems we modelled, we observe the binding of EGCG with IAPP, and all simulation components tend to form a single cluster (Fig. 4-4 and Fig. 4-5). Examinations of the final aggregates reveal amorphous structures, with EGCG ligands forming small clusters and scattering inside (Fig. 4-4B). These results are

consistent with our experimental observations of IAPP aggregates of amorphous morphology in the presence of EGCG. Additionally, the observed structures of IAPP-EGCG complexes are drastically different from the reported complexes formed by IAPP with small molecules resveratrol or curcumin.[93] For resveratrol and curcumin, the hydrophobic ligands aggregate into a nano-sized core, while IAPP peptides are bound to the surface by burying hydrophobic residues and leaving hydrophilic residues exposed, which turns into a well-defined off-pathway oligomer that subsequently inhibits fibrillization. For EGCG, the small ligand clusters appear to scatter inside the amorphous aggregates, which may not have prevented the continuous growth of aggregates, but interfered with the formation of an elongated fibril instead, and would result in the formation of curly aggregates (Fig. 4-1 and Fig. 4-2). This difference likely originates from the higher solubility of EGCG compared with that of resveratrol or curcumin.

Further analysis of the binding suggests residues R11, F15, H18, F23, and Y37 on IAPP, all of which are aromatic residues, exerts significantly stronger binding effect with EGCG than other residues (Fig. 4-4D). As a polyphenol small molecule, EGCG ligand contains multiple benzene rings, its strong binding with aromatic residues indicates π-stacking is the driving force of IAPP-EGCG interfaces. This finding is similar to that of our study on the off-pathway nano-assemblies of IAPP with curcumin and resveratrol, where aromatic F15, F23, and Y37 residues are the most actively engaged in binding with small molecules.[93] The strong binding of EGCG with R11 indicates the importance of hydrogen bonding.

Simulations of IAPP interfacing oxidized EGCG. We also model the oxidized EGCG after Theasinensin A (ThA), a cross-linked EGCG dimer identified as a major product of EGCG auto-oxidization (Fig. 4-1B).[99] DMD simulations are performed for 2, 4, and 6 IAPP peptides mixed with ThA at a 2:1 ratio to keep a similar mass ratio to the simulations of EGCG with IAPP. Our simulations display ThA binds IAPP in a similar profile as EGCG, and forms similar complexes (Fig. 4-6C). However, ThA binds IAPP at a slower rate than EGCG-IAPP binding, which may due to the larger size and therefore slower diffusion rate of ThA. Consequently, EGCG tends to bind IAPP first before the IAPP self-association, while self-association of IAPP takes place before its binding with ThA (Fig. 4-4C, Fig. 4-5, and Fig. 4-6A). The slower binding of ThA with IAPP may have contributed to the reduced capability of ThA in inhibiting IAPP aggregation, as observed experimentally.

Conclusion

In summary, our study reveals that EGCG, oxidized EGCG, and (GSH)-reduced EGCG all appear effective at IAPP amyloid inhibition. Different from small molecules resveratrol or curcumin which could direct the IAPP amyloid aggregation process into a well-defined off-pathway oligomer that subsequently inhibits fibrillization, EGCG ligands would form small clusters and scatter around IAPP and result in amorphous aggregates, which may subsequently prevent the continuous growth of aggregates. Our analysis of binding between EGCG and IAPP reveal that the comparable effects on IAPP fibrillization inhibition by EGCG species are indicative of the significance of π-stacking, as hydrogen bonding and hydrophobic interactions are altered while aromatic EGCG moieties are

conserved across the three cases. In light of the importance of π-stacking in peptide assembly and fibrillization inhibition and remodeling, exploiting this mode of interaction by molecular design may hold the key to effective peptide aggregation intervention.

Materials and Methods

DMD simulations. We apply all atom DMD simulations to study the interfacings of EGCG and oxidized EGCG with IAPP. Our simulations are performed under the same protocol as that introduced in chapter two.

Simulation setup. In simulations of EGCG binding with soluble IAPP peptides, the initial structure of the IAPP monomer is obtained from the Protein Data Bank (PDB ID: 2L86), and we use the EGCG structure obtained from PubChem (CID: 65064). To keep the peptide concentration fixed during simulations of EGCG binding with various numbers of soluble IAPPs, we vary the size of a cubic simulation box with a dimension of 63.7Å for one IAPP to 127.4Å for eight peptides. Ten independent simulations are carried out for each system with different initial conditions, including randomized velocities, intermolecular distances and orientations. In our data analysis, we use an inter-atomic distance cutoff of 5Å to define an atomic contact.

Materials. Human IAPP is obtained as lyophilized powder from AnaSpec. EGCG (≥95%) and L-glutathione (≥98%) are acquired from Sigma-Aldrich. IAPP is weighed using a Cubis MSE balance (0.01mg resolution; Sartorius), dissolved in water to a concentration

of 100μM, and used immediately for TEM sample preparations. EGCG stock solutions (1mM) are prepared immediately or 24h prior to TEM sample preparation to obtain fresh or oxidized EGCG, respectively. Fresh EGCG solutions are colorless up until 6h, while oxidized EGCG solutions appears light yellow. Therefore, nominally fresh EGCG would have been partially auto-oxidized after 6h. Reduced EGCG is obtained by mixing the polyphenol with GSH (1mM stock) at a 1:1 molar ratio in water. All solutions are prepared using degassed ultrapure Milli-Q water (18.2MΩ·cm; Millipore Corporation, USA).

In vitro studies. To investigate the interaction between IAPP with different EGCG species and also the inhibition effect, our collaborators apply multiple *in vitro* studies including ThT assay, high-resolution TEM imaging, CD spectroscopy and AFM assay. Details can be found elsewhere in our publication.[100]

CHAPTER FIVE

Star Polymers Reduce the IAPP Toxicity via Accelerated Amyloid Aggregation

Introduction

Aggregation inhibition with the use of small molecules as well as polymeric nanoparticles (NPs) has been a major strategy against amyloid-mediated toxicity.[90,101,102] Polymeric NPs have been explored as protein aggregation inhibitors utilizing their tunable hydrophobicity as well as their capacity for initiating H-bonding.[103–106] Curiously, previous studies report the amyloidogenesis of melanocyte protein Pmel17 in the human system is entirely nonpathogenic.[107] The rapid fibrillization of Pmel17, which transits from monomeric form to mature amyloid fibrils within 3s, is a cytoprotective mechanism through reducing the half-life of the most toxic intermediate products (i.e., oligomers and protofibrils) to favor the formation of less toxic or nontoxic mature amyloid fibrils. Later studies also show this effect can be extended to other pathogenic amyloids.[108] Therefore, the concept of fibrillization promotion instead of inhibition, provides a biomimetic and perhaps counterintuitive strategy in the mitigation of amyloid cytotoxicity. In this study, we synthesize and demonstrate the use of star-shaped polymer poly(2-hydroxyethyl acrylate) (PHEA) nanostructure as an anti-IAPP agent capable of cytoprotective rescue of pancreatic β-cells through the promotion of amyloid aggregation.[109] PHEA stars are synthesized using a reversible addition-fragmentation chain-transfer (RAFT) polymerization methodology and are weakly negatively charged, each possessing a hydrodynamic size of ~12nm and containing on average 12 arms. Through biophysical

characterizations, we demonstrate a significant, positive correlation between the promotion of amyloid aggregation induced by PHEA stars and the reduction in IAPP-mediated cytotoxicity both *in vitro* and *ex vivo*. Additionally, we also identify a new amyloid morphology through our work, named "stelliform amyloids", which is formed by the co-aggregation of IAPP and PHEA stars at a molar ratio of 5:1. Atomistic DMD simulations further reveal the PHEA stars possess rigid rod-like arms which can serve as linear scaffolds for IAPP binding and therefore accelerate the nucleation of β-sheet aggregates by increased local peptide concentration. Each arm of the PHEA stars could nucleate the fibrillization of IAPP resulting in the stelliform amyloid morphology. This study opens the door to the design and application of a new class of agents against amyloid diseases.

Results and Discussion

Modulation of IAPP fibrillization by PHEA polymers. Our collaborators first apply ThT fluorescence assay to provide a measurement of both the extent and kinetics of amyloid fibrillization over time. The control IAPP is shown to fibrillate with a nucleation period of ~2h followed by an exponential period of ~12h before reaching saturation at 14h (Fig. 5-1A). Incubation of PHEA with IAPP at molar concentrations of 1:125, 1:25, and 1:5 have a promotional effect on IAPP fibrillization, with the largest increase in ThT fluorescence observed at 1:5. Following the trend of increasing fibrillization with increasing concentration of PHEA, the energetically unfavorable nucleation period is also shown to significantly decrease with increasing concentration of PHEA, falling from ~3.5h in the IAPP control to less than 30min with the highest concentration of PHEA. The reduction in

IAPP lag time is also demonstrated through CD spectroscopy, wherein the presence of PHEA to IAPP at the 1:5 ratio notably promotes the amyloidogenic conversion of random coil content to β–sheets (Fig. 5-1B and Fig. 5-2). Over 2.5h, the β-sheet conversion in IAPP with PHEA at 1:5 ratio (25-34%) is 2.3× more rapid than that of IAPP alone (29-33%). Concordantly, IAPP contains 25% higher β-sheet content at 24h in the presence of PHEA (55%) compared to that of IAPP alone (44%). This shift in prototypical IAPP aggregation kinetics, in addition to the promotion of fibrillization overall, presents a case for rapid local sequestration of IAPP seeds by PHEA.

Stelliform amyloid formation by PHEA. TEM imaging complement ThT and CD measurements for fibrillating IAPP, allowing further analysis of persistence and contour length of amyloid fibrils generated after 24h in aqueous solution in the presence and absence of PHEA. After 24h, IAPP amyloidogenesis reaches the saturation phase, and long, semi-flexible fibrils can be observed by TEM with some shorter species still present (Fig. 5-3A). Once fibril elongation and 3D cross-linking occurred at>5 days of amyloidogenesis, amyloids form in-solution hydrogels, and generally, shorter species are absent.[110] "Stelliform amyloids" are observed when PHEA incubated with IAPP at a 1:5 molar ratio (Fig. 5-3A). These amyloids are characterized by a central nucleation "core", ranging from smaller clusters of 50-150nm to micrometers in diameter. Fibrils of low persistence (average of 891.9nm compared with that of 2885±60nm for the IAPP control) and contour length (<1350nm) are additionally observed radiating out from the core, forming the full

stelliform structure of ~0.5μm in diameter for smaller cores and micrometers in diameter for larger cores with some macroscopic aggregates visible in solution (Fig. 5-3A).

With lower concentrations of PHEA, the fibrillization products generally trend towards matching the structural morphology of IAPP alone (Fig. 5-3B). IAPP amyloid fibrils with significantly reduced contour lengths are produced with increasing PHEA concentration, indicating polyphenol-like stabilization of growing fibrils through H-bonding; hydrophobic and π-π interactions by PHEA may have terminated fibril elongation, resulting in a fibril population with predominantly low contour lengths.[93] As fibril elongation is mediated by amyloid seeds, the extensive exponential periods observed in the ThT assay could be indicative of the PHEA-IAPP complex rapidly sequestering amyloid seeds to render large populations of shorter fibrils, thus depleting the available seeding population to perform elongation (Fig. 5-1).

Stelliform IAPP amyloids are cytoprotective in vitro and ex vivo. IAPP-mediated cytotoxicity is assessed in an insulin-producing pancreatic β-cell line over a 24h period and *ex vivo* in mouse islets after 48h (Fig. 5-4). PHEA stars are completely biocompatible at all concentrations tested. *In vitro*, IAPP alone typically begin to induce cytotoxicity at ~6h post-treatment with cell death progressing exponentially up until the 20-24h mark to an end point toxicity value of 38%. When incubated with IAPP at 1:25 and 1:125 ratios, PHEA stars delay the progression of IAPP toxicity by ~2h and reduce IAPP-mediated toxicity overall compared to that of the IAPP control. However, when PHEA incubated with IAPP at 1:5 ratio, cells are 94% viable after 24h, and low levels of cytotoxicity are only observed

more than 15h post incubation. The cytoprotective capacity of PHEA stars at a 1:5 ratio to IAPP is also seen *ex vivo*, where mouse islets treated with IAPP in the presence of the highest concentration of PHEA stars (~8% relative cell death) demonstrate a significant reduction in toxicity compared to that of IAPP alone (64%) after 48h treatment.

The near-complete mitigation in IAPP-mediated toxicity observed both *in vitro* and *ex vivo* when IAPP is incubated with PHEA stars correlates with the stelliform amyloid formation as observed (Fig. 5-3A). Likely the key to the cytoprotective nature of stelliform amyloids lies first in their mechanism of formation and additionally in terms of the structure itself. First, oligomeric and proto-fibrillar species formed as intermediates during IAPP amyloidogenesis are widely considered responsible for the majority of IAPP-mediated cytotoxicity, with far less toxicity attributed from amyloid fibrils. Concordantly, rapid sequestering of toxic low-order IAPP species through the formation of stelliform amyloids mediated by PHEA stars would reduce the local population of toxic species.

Lastly, it has also been purported that the cytotoxicity of amyloid fibrils is mediated through partitioning of the hydrophobic, stiff fibrils into the cell membrane, leading to disruption of the membrane and production of radical oxygen species.[111–113] The structure of stelliform amyloids, with a compact core and vastly reduced persistence and contour lengths of radiating fibrils, would be unable to effectively partition into the lipid bilayer and would also readily form a protein corona within the extracellular milieu through electrostatic and hydrophobic interactions, further limiting any amyloid contact with cellular membranes.[114–116] Importantly, we observe complete protection from IAPP-induced cell death in primary mouse islets treated with PHEA stars at a 1:5 molar ratio.

In silico study of the PHEA polymers and their effects on IAPP aggregation. To complement the experimental findings, we examine the structural properties of model PHEA polymers by all-atom DMD simulation. We first study the 2-arm PHEA polymers with different degrees of polymerization (DP) and compute their corresponding radius of gyration (*Rg*) values (Fig. 5-5A&D). The data reveal an approximately linear dependence of *Rg* on DP (up to ~40), suggesting the PHEA stars are rather rigid (Fig. 5-5D). The autocorrelation analysis of the polymer dynamics results in an estimated Kuhn length of ~36 repeats, which confirms the rigidity of the PHEA stars (Fig. 5-5E). To evaluate the structure and dynamics of PHEA stars, we study an 8-arm PHEA model with molecular compositions resembling the experimental data in all-atom DMD simulations. A rapid equilibration in terms of *Rg* and ellipticity is observed (Fig. 5-5F). The average *Rg* of the 8-arm polymer is ~4.5nm, consistent with the experimentally measured hydrodynamic radii ~4.9nm, and the high ellipticity value (close to 1) suggests the 8-arm PHEA adopt a non-spherical conformation. Because of the high rigidity, the interactions between different arms are found minimal beyond the covalent cross-links. Therefore, the all-atom DMD simulations reveal a unique morphology of the PHEA that features a micellar structure with a porous interior for encapsulating small molecules and IAPP peptides.

To provide molecular insight into IAPP-PHEA binding and its effect on IAPP self-association, we perform DMD simulations on two sets of molecular systems with one containing six IAPP peptides along with a 6-arm PHEA polymer and another of six peptides alone as the control (Fig. 5-5B). By monitoring the size of the largest IAPP

aggregates, we find the presence of PHEA promotes the IAPP self-aggregation *in silico* (Fig. 5-6A). On the basis of the last 25ns of simulations where the largest IAPP aggregates are formed, the binding probabilities of each IAPP residue with PHEA reveal that both polar and nonpolar residues could bind PHEA, though hydrophobic and aromatic residues show a slightly higher binding propensity (Fig. 5-6B). As a result, the generally nonspecific attractions between IAPP and PHEA lead to the accumulation of peptides on PHEA arms, and the increased local peptide concentration accelerates the aggregation of IAPP consistently with a previous coarse-grained computational study.[117] We also examine the secondary structure of IAPPs and their binding with PHEA along the simulation trajectories, where a general trend of correlation between IAPP-PHEA binding and β-sheet formation in IAPP aggregates is evident (Fig. 5-7). Comparison-average secondary structure contents of the last 25ns between simulations with and without PHEA suggest the PHEA binding accelerates IAPP self-association without significantly change in the structure of the aggregates (Fig. 5-6C&D).

Next, we analyze the kinetics of β-sheet formation for simulations of IAPPs with and without PHEA. We fit our data following the sigmoidal-like kinetics and obtain the lag time and elongation rate for each independent simulation. Our data reveal the presence of PHEA significantly reduces the aggregation lag time and broadens the distribution of elongation rate, further suggest PHEA binding accelerates the nucleation of β-sheet aggregates and induces heterogeneity in β-sheet elongation (Fig. 5-8B&C). Additionally, wo compute the potential of mean force (PMF) with respect to the size of IAPP oligomers, $n_{oligomer}$, and the degree of IAPP fibrillization, $Q_{fibrillization}$. Two major basins can be

observed in the PMF with or without presence of PHEA, corresponding to the IAPP monomers/oligomers with little amount of β-sheet contents, and IAPP aggregates with high amount of β-sheet contents, respectively (Fig. 5-9). Saddles connecting the two basins are corresponding to the aggregation pathways and intermediates. According to our PMFs, the presence of PHEA renders the non-β-sheet basin shallower and the saddle broader, suggesting more pathways towards the final β-rich aggregates and is accounted for the reduced aggregation lag time and heterogeneity in β-sheet elongation rate.

Conclusion

Inspired by the mechanism of Pmel17 amyloidogenesis, we have developed and established that a polymeric star nanoparticle, PHEA, is capable of mitigating IAPP-mediated toxicity both *in vitro* and *ex vivo* through PHEA-mediated promotion of IAPP aggregation and formation of a unique "stelliform amyloid" morphology. PHEA stars possess the structural properties of high rigidity, long arm length, and rich aromatic moieties, and facilitate rapid deposition and fibrillization of IAPP monomers into amyloid fibrils. Subsequently, this amyloid structure elicits significantly reduced toxicity in a pancreatic β-cell line and in mouse islets when compared to the long, semi-flexible fibrils typically formed by IAPP. Our study suggests that the shape/morphology of the PHEA stars is likely a contributing factor in the IAPP-PHEA interaction, and shortening of the oligomer lifetime through amyloid aggregation promotion represents a potential strategy to be explored within the larger context of amyloid research. This study has shed new light

on the IAPP structure-toxicity relationship and presents an alternative blueprint for the design of polymeric nanomedicines against amyloidogenesis.

Materials and Methods

DMD simulations. Our DMD simulations are performed under the same protocol as that introduced in chapter two.

Simulation setup. All the PHEA model structures are constructed with the Avogadro molecular builder software and energy minimized with the MMFF94s force field. MedusaScore, an extension of the Medusa force field, is adapted to model the polymers in addition to IAPP. The MedusaScore is parametrized on a large set of ligands and is transferrable to different molecular systems. The predictive power of MedusaScore has been validated in various benchmark studies, including recent community structure-activity resource (CSAR) blind ligand-receptor docking prediction exercises.[43,119]

For each 2-arm PHEA, we perform 20 independent simulations at 300K with different starting configurations. Each independent simulation is lasted for 300ns, and an accumulative 6μs simulation is obtained for the polymer model. We use the last half of all simulations to compute the radius of gyration (*Rg*) values of the modeled polymers. For the 8-arm PHEA, 20 independent simulations are performed at 300 K with different starting configurations, each of which lasted 200ns.

The IAPP (PDB ID: 2L86) structure is obtained from PDB. Counter ions Cl^{1-} are introduced to achieve a neutral charge condition if necessary. For systems containing six

IAPPs, the peptide concentration is maintained by fixing the dimension of the simulation box as 120Å, and periodic boundary conditions are applied. For each of the multi-molecular systems, 20 independent simulations starting with different intermolecular distances and orientations are performed at 300K with each run lasted 100ns.

Secondary structure analyses are performed using the dictionary secondary structure of protein (DSSP) method. For each snapshot structure, the secondary structure, such as helix, sheet, coil, and turn, for each residue has been obtained. An empirical sigmoidal function

$$y = \frac{(I_{max} - I_{min})}{\left(1 + exp\left(-k(t - t_0)\right)\right)} + I_{min}, \qquad (5\text{-}1)$$

is adopted to fit the kinetics of the total number of residues in the β-sheet conformation, where fitting parameters *A*, *B*, t_0, and *k* correspond to the max and min values of aggregation, the midpoint time of aggregation, and the elongation rate, respectively. The lag time is determined as

$$t_{lag} = t_0 - 2/k, \qquad (5\text{-}2)$$

In the potential of mean force (PMF) calculation, normalized sigmoidal function, $Q_{fibrillization}$=1/(1+ exp(−k(t − t0))), is used to quantify the extent of fibrillization for each independent simulation. For a given snapshot, the distribution of IAPP oligomers is analyzed, where any two peptides interconnected by at least one intermolecular heavy atom contact (the cutoff of 0.55nm) is defined to belong to an oligomer. The size of an oligomer, $n_{oligomer}$, was defined by the number of IAPP peptides forming the aggregate. The two-dimensional PMF (or effective free energy) is computed according to

$$PMF = -K_B T \ln P(n_{oligomer}, Q_{fibrillization}), \quad (5\text{-}3)$$

where K_B is the Boltzmann constant, T corresponds to the simulation temperature 300K, and $P(n_{oligomer}, Q_{fibrillization})$ is the probability of finding a peptide in an oligomer with the size of $n_{oligomer}$ and the extent of fibrillization $Q_{fibrillization}$ at the time.

Materials. 2-Hydroxyethyl acrylate (HEA) is purchased from Sigma-Aldrich and deinhibited by passing through a column of basic alumina. S,S′-Dibenzyl trithiocarbonate (DBTC), N,N′ methylenebis- (acrylamide) (X) is purchased from Sigma-Aldrich. Azobis-(isobutyronitrile) (AIBN) is purified by recrystallization from methanol before use. Dimethyl sulfoxide (DMSO) is purchased from Merck Millipore and used as received. Human IAPP is obtained in lyophilized powder form from AnaSpec and made up to a 200μM stock immediately prior to an experiment or allowed to fibrillate at 25°C for >5 days to produce mature IAPP amyloids. All materials are weighed out on a Cubis MSE balance (Sartorius, 0.01mg resolution) and made up fresh in Milli-Q water prior to experiments unless otherwise specified. Thioflavin-T (ThT) dye (Sigma-Aldrich) is prepared fresh for each experiment at a 250μM stock solution. Propidium iodide (PI) dye stock solution (1mg/mL in water) is stored at -20°C. Detailed information about raft synthesis of poly(2-hydroxyethyl acrylate) stars can be found elsewhere.[118]

In vitro and ex vivo studies. The experimental studies carried out by our collaborators can be found in our publication.

FIGURE CAPTIONS

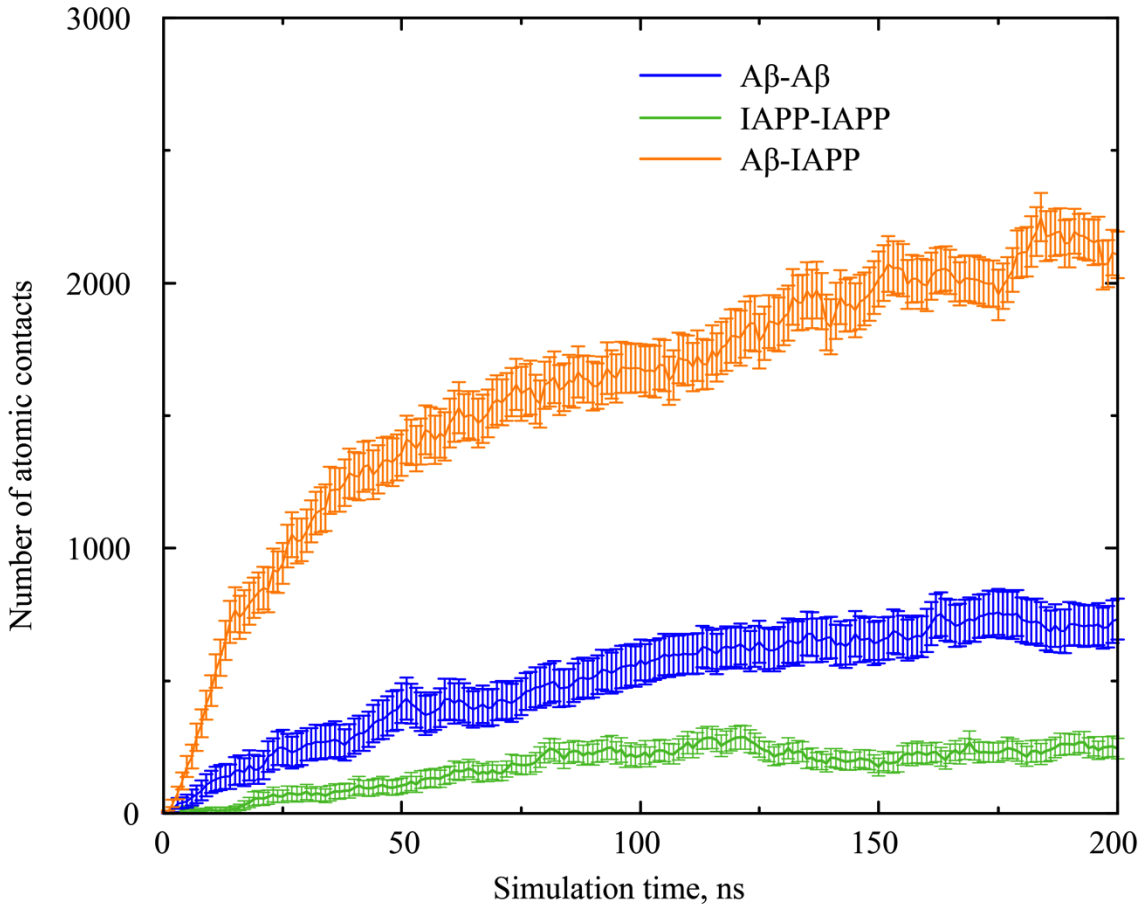

Figure 2-1. Time evolution of atomic contacts between IAPPs (green), Aβs (blue), and IAPP-Aβ (orange). Data are derived from simulation system containing two IAPPs and Aβs. Error bars denote the standard error of means (SEM).

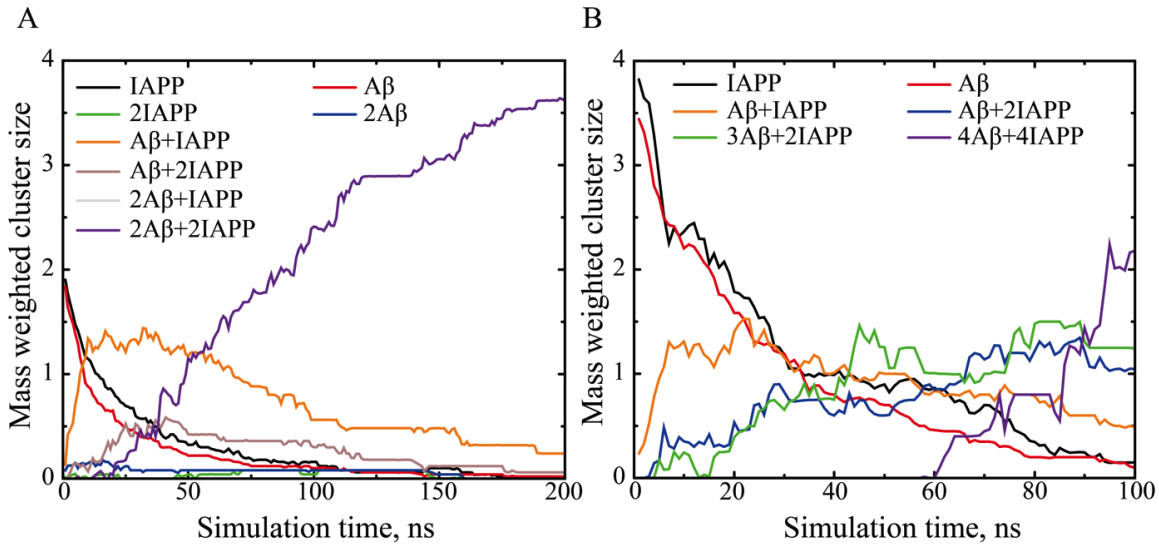

Figure 2-2. Time evolution of peptide cluster species for IAPP-Aβ mixtures with molecular ratios of (A) 2:2 and (B) 4:4. The number of each species weighted by the number of peptides forming the cluster is averaged over the number of independent simulations. For simulations with 2:2 ratio, all possible cluster species are shown. In the case of 4:4 ratio, only the six most-populated cluster species are shown.

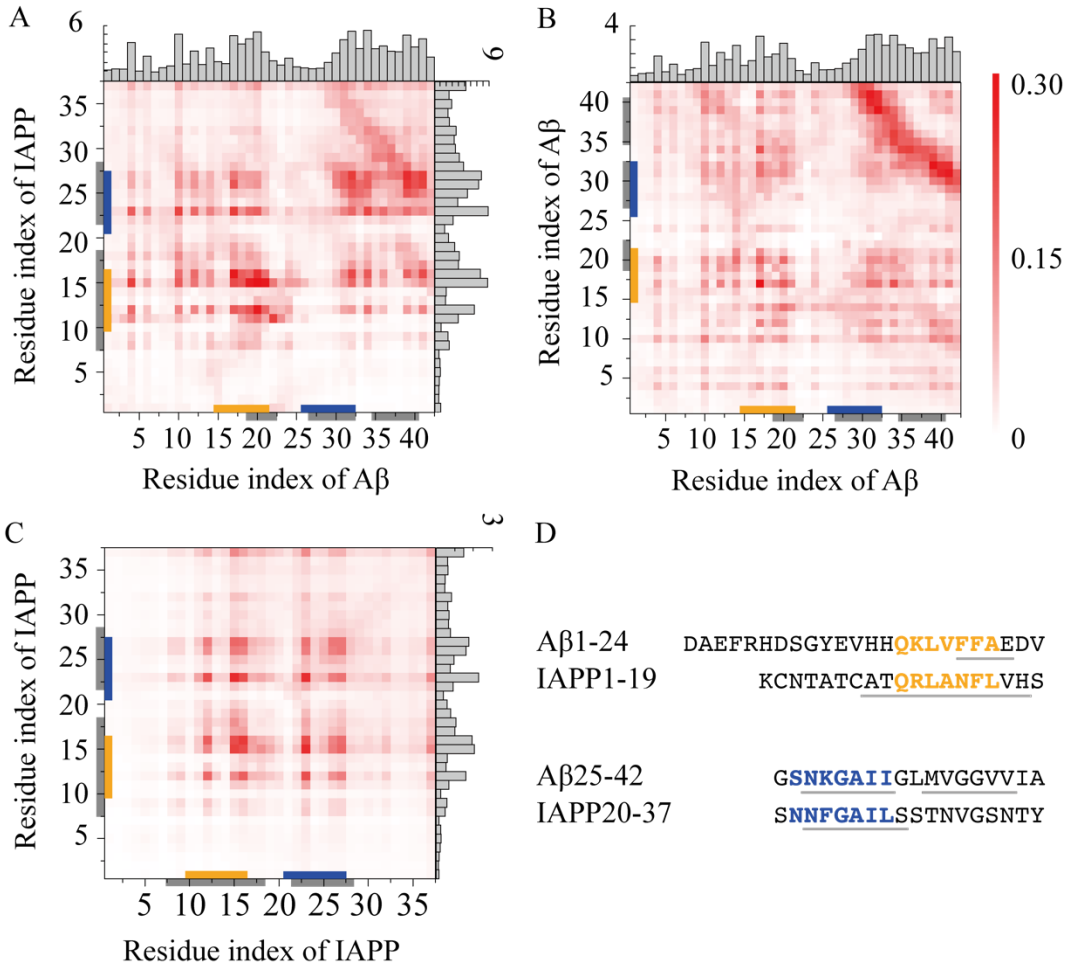

Figure 2-3. Identification of hot regions for inter-peptide interactions in both cross- and self-associations of IAPP and Aβ. Residue-wise contact frequency maps are computed for (A) IAPP and Aβ binding in heterodimer simulations, and self-association of (B) Aβ and (C) IAPP in dimer simulations. Histograms are also obtained to show the total contact frequency of each residue. (D) Sequence fragments with the highest degree of similarity between Aβ and IAPP are highlighted in orange and blue, while the domains experimentally-identified to be important for both their cross- and self-associations are highlighted in gray.

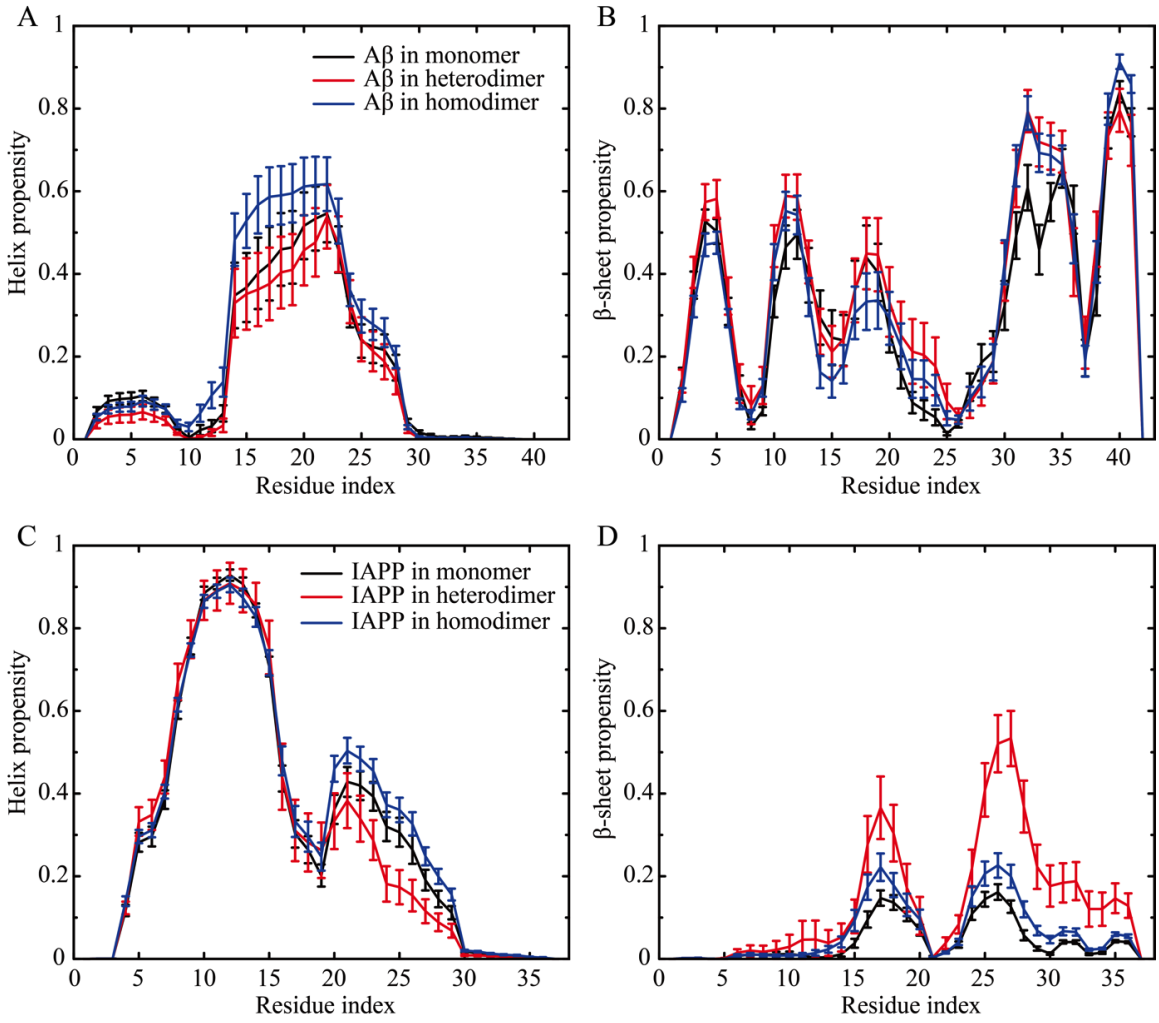

Figure 2-4. The secondary structure propensity of Aβ and IAPP in monomer, heterodimer, and homodimer. (A, C) Helix propensity and (B, D) β-sheet propensity of each peptide residue, where data for different peptide states are shown in black, red and blue respectively. All data are averaged over the last half of 20 independent simulations, with each performed for 600ns simulation time. Error bars denote the standard error of means (SEM).

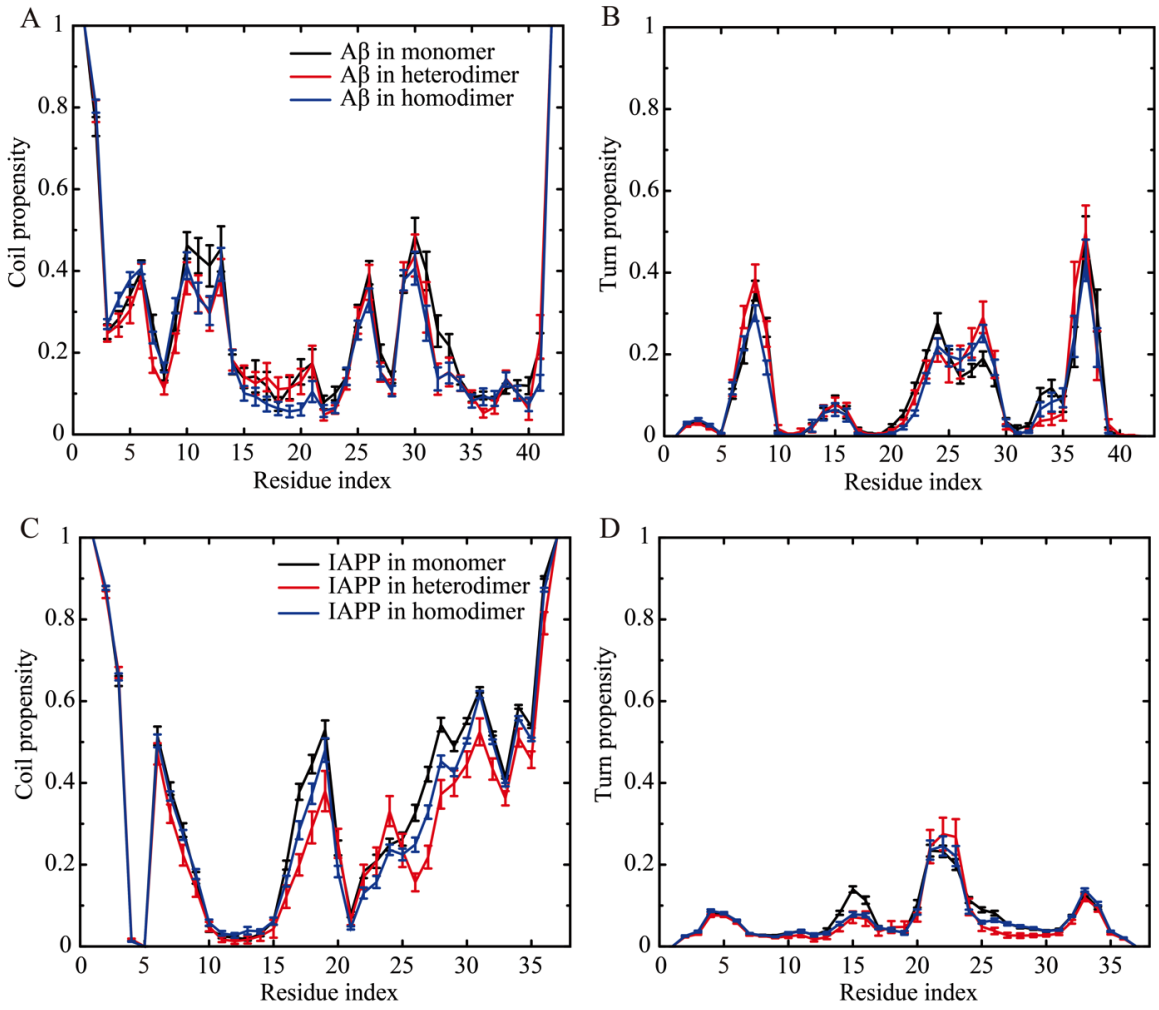

Figure 2-5. The secondary structure propensity of Aβ and IAPP in monomer, heterodimer, and homodimer. (A, C) Random coil propensity and (B, D) turn propensity of each peptide residue, where data for different peptide states are shown in black, red and blue respectively. All data are averaged over the last half of 20 independent simulations, with each performed for 600ns simulation time. Error bars denote the standard error of means (SEM).

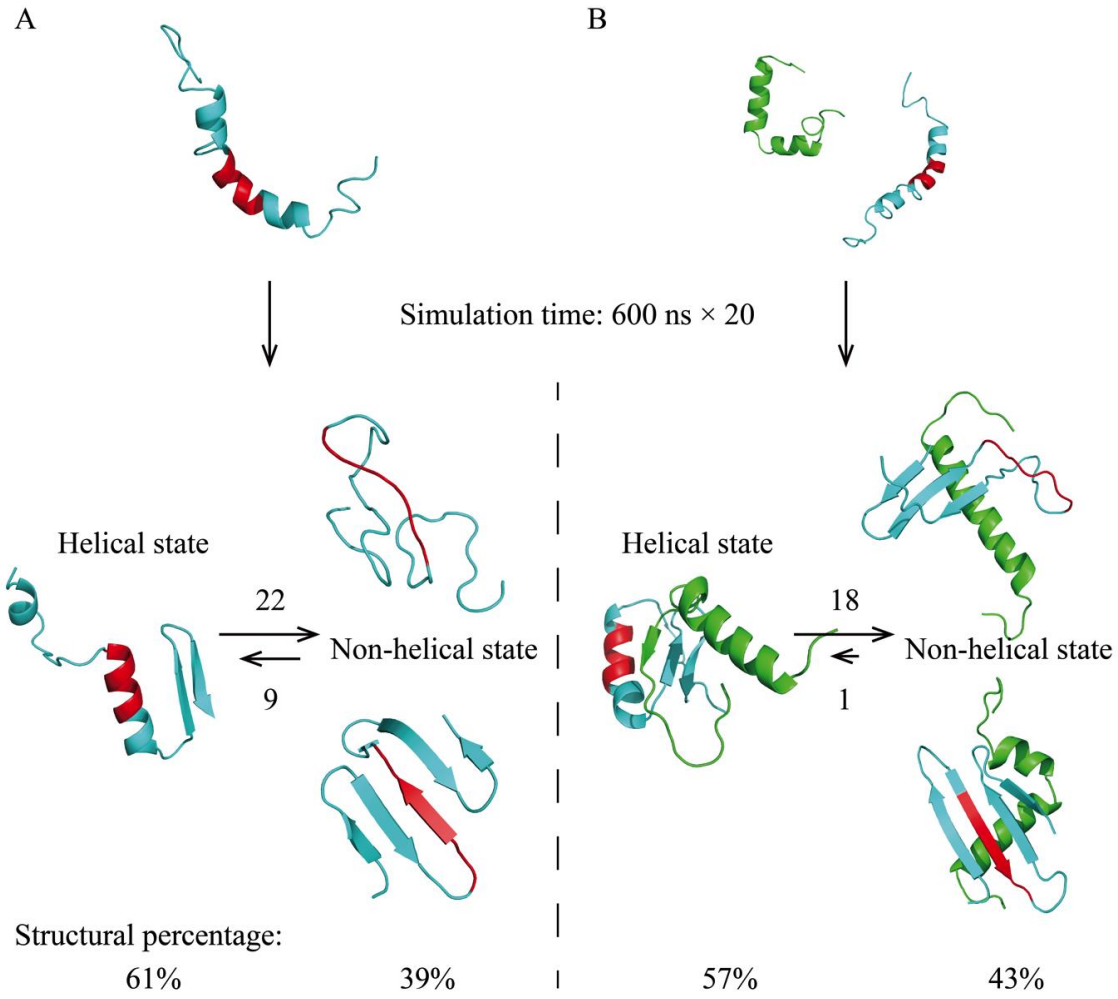

Figure 2-6. Conformational dynamics of the helix unfolding and refolding in the amyloidogenic region of Aβ16-22. Numbers of transition between helical and non-helical state are recorded for (A) Aβ monomer simulations and (B) IAPP-Aβ heterodimer simulations. IAPP peptides are colored in green and Aβ in cyan, while the amyloidogenic region of Aβ16-22 is highlighted in red. Observation of the helix unfolding/refolding events and structural percentage of the helical/non-helical state are determined over 20 independent simulations, with each lasted 600ns. Simulation snapshots are used to display peptide structures.

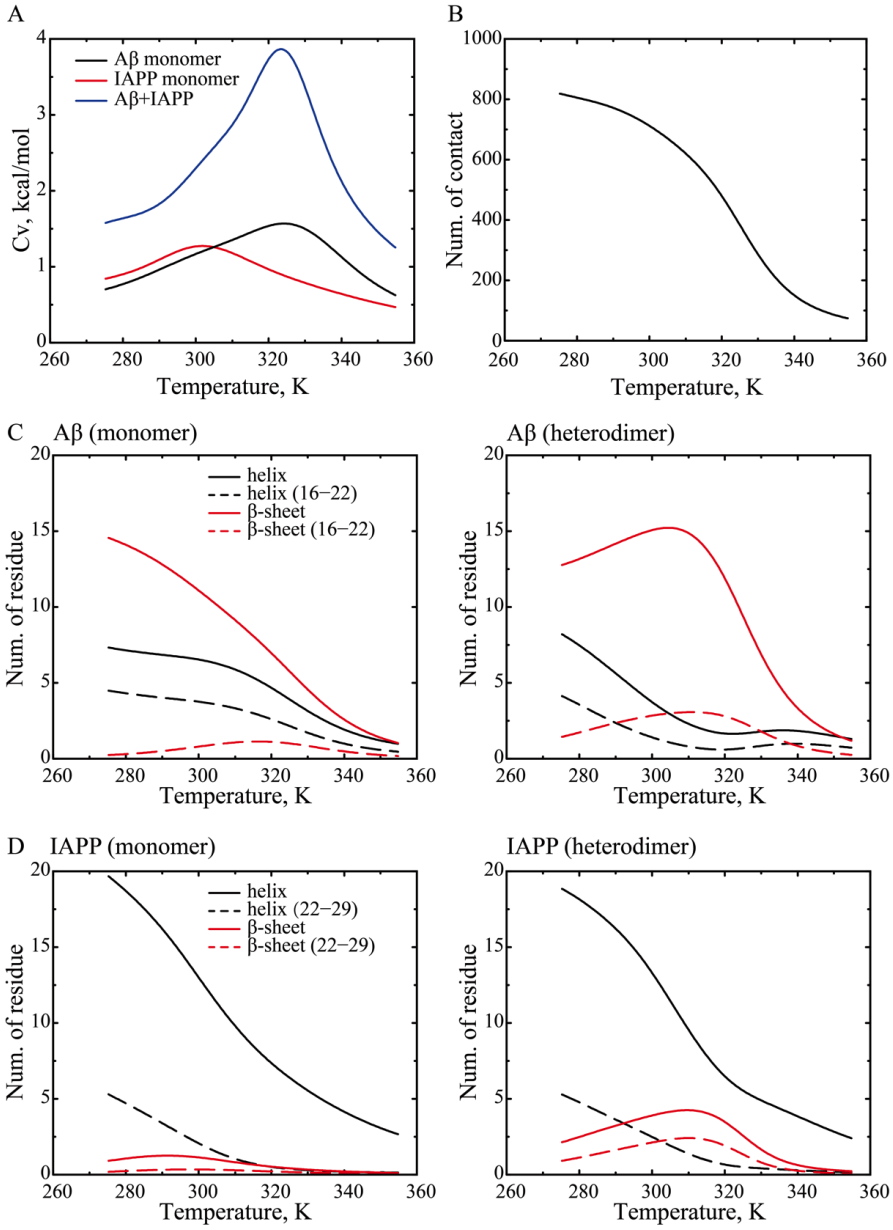

Figure 2-7. Replica exchange simulations of IAPP monomer, Aβ monomer, and heterodimer. The temperature dependence of (A) heat capacity (C_V), (B) number of atomic contacts between IAPP and Aβ in heterodimer, (C) secondary structure contents of Aβ in monomer/heterodimer, and (D) secondary structure contents of IAPP in monomer/heterodimer are displayed respectively.

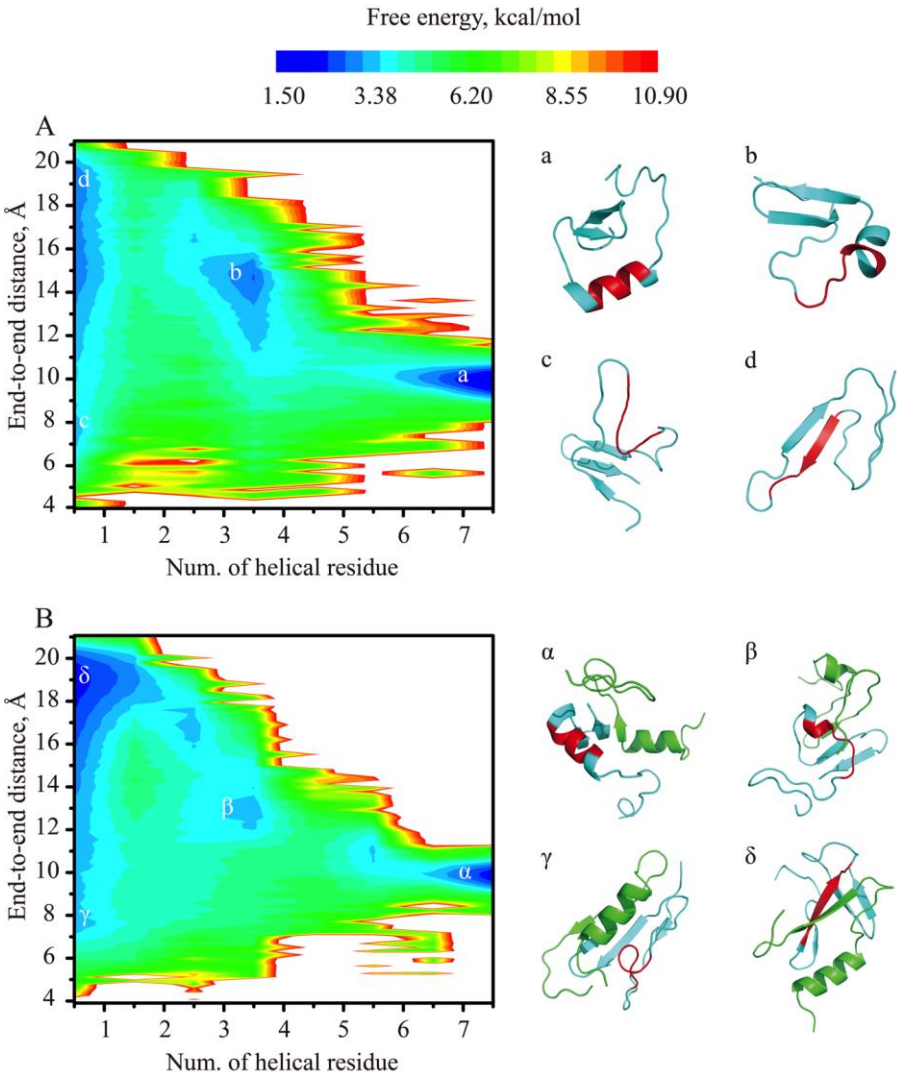

Figure 2-8. The conformational free energy landscape of the amyloidogenic Aβ16-22 at 300K in simulations of (A) the Aβ42 monomer and (B) the Aβ42-IAPP heterodimer. Using the WHAM analysis of the replica exchange simulation trajectories, the 2D PMF is computed as the function of the number of helical residue and end-to-end distance. The basins correspond to helical (a, α), partially helical intermediate (b, β), and non-helical (c, d and γ, δ) states. IAPP peptides are shown in green and Aβ in cyan. The amyloidogenic region of Aβ16-22 is highlighted in red.

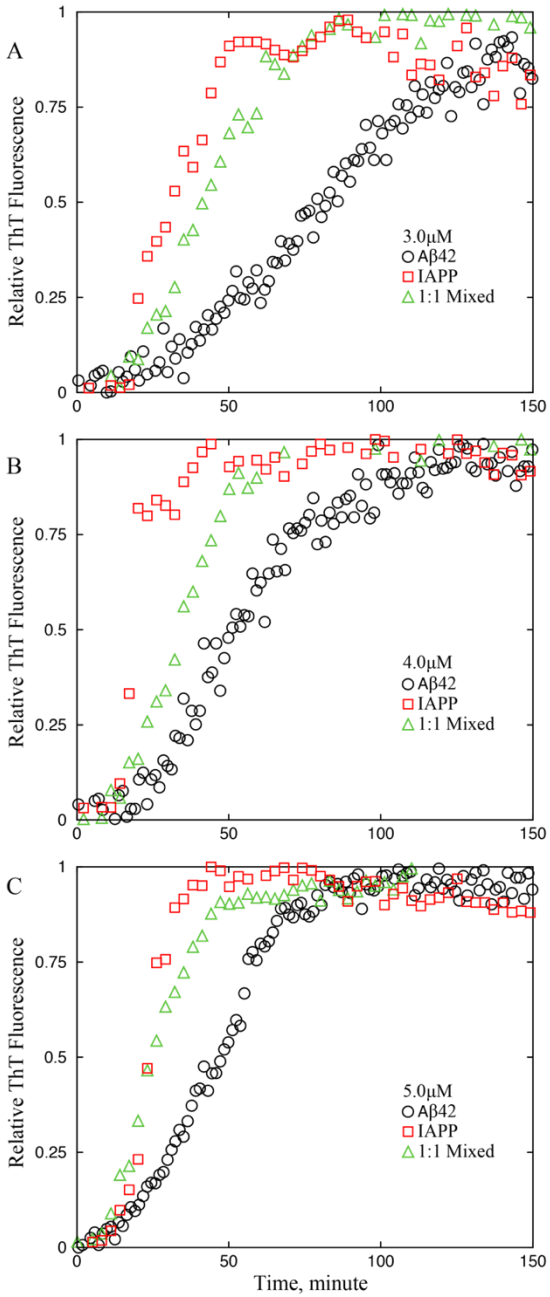

Figure 2-9. ThT fluorescence intensity of peptides at (A) 3.0μM, (B) 4.0μM, and (C) 5.0μM indicating the sigmoidal aggregation kinetics. Peptide concentration of 1.0, 2.0, 2.5, 3.0, 3.5, 4.0, and 5.0μM are examined with multiple repeats, with their fluorescence intensity normalized into 0~1. Data from 9 individual tests are shown in this figure.

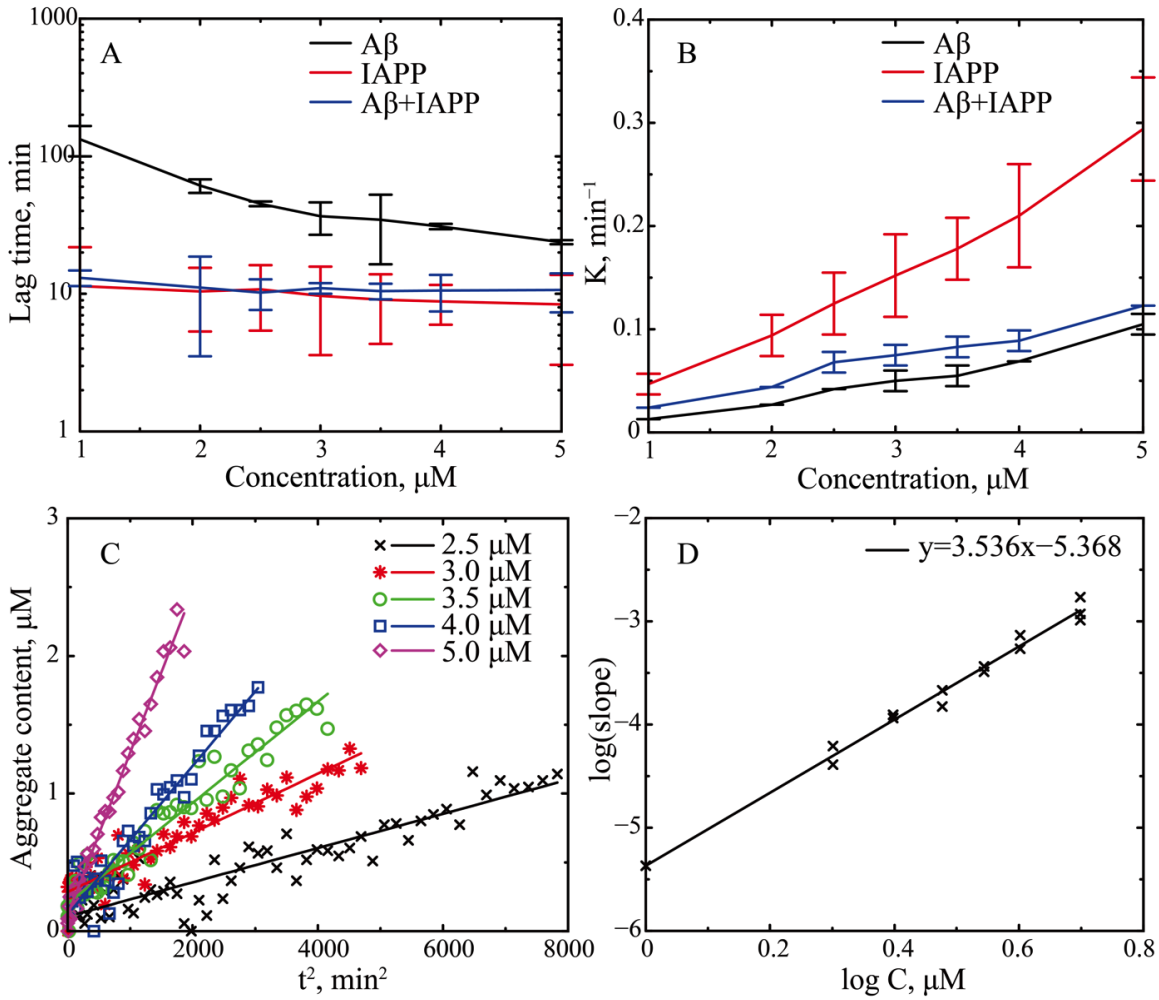

Figure 2-10. *In vitro* studies of IAPP-Aβ cross- and self-association. The concentration dependence of (A) the aggregation lag time and (B) fibril elongation rate for Aβ-IAPP co-aggregation (blue), and the self-aggregation of Aβ (black) and IAPP (red). (C) For the aggregation of Aβ, the amount of aggregates during the initial phase of aggregation linearly depends on the square of time, t^2. (D) The log-log plot of the slops in panel C vs. the peptide concentrations shows the power-law dependence. The linear fit in the log-log plot results into an exponent index of ~3.54s.

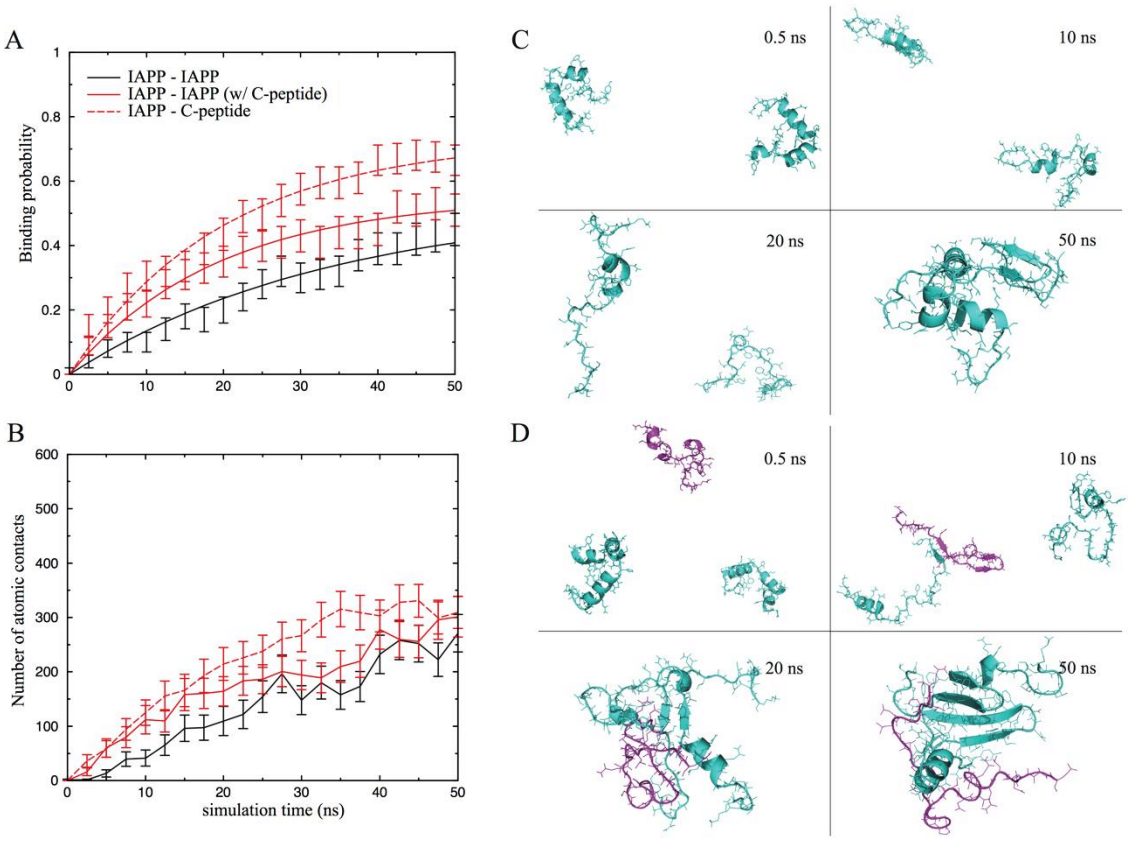

Figure 3-1. DMD simulations of IAPP dimerization with and without the presence of C-peptide. (A) Trajectories of binding probability and (B) trajectories of number of atomic contacts between different peptides. Error bars denote the standard error of means (SEM). Structural snapshots are displayed for simulation of (C) IAPPs alone and (D) IAPPs with C-peptide. IAPP peptides are colored in cyan while C-peptide in magenta.

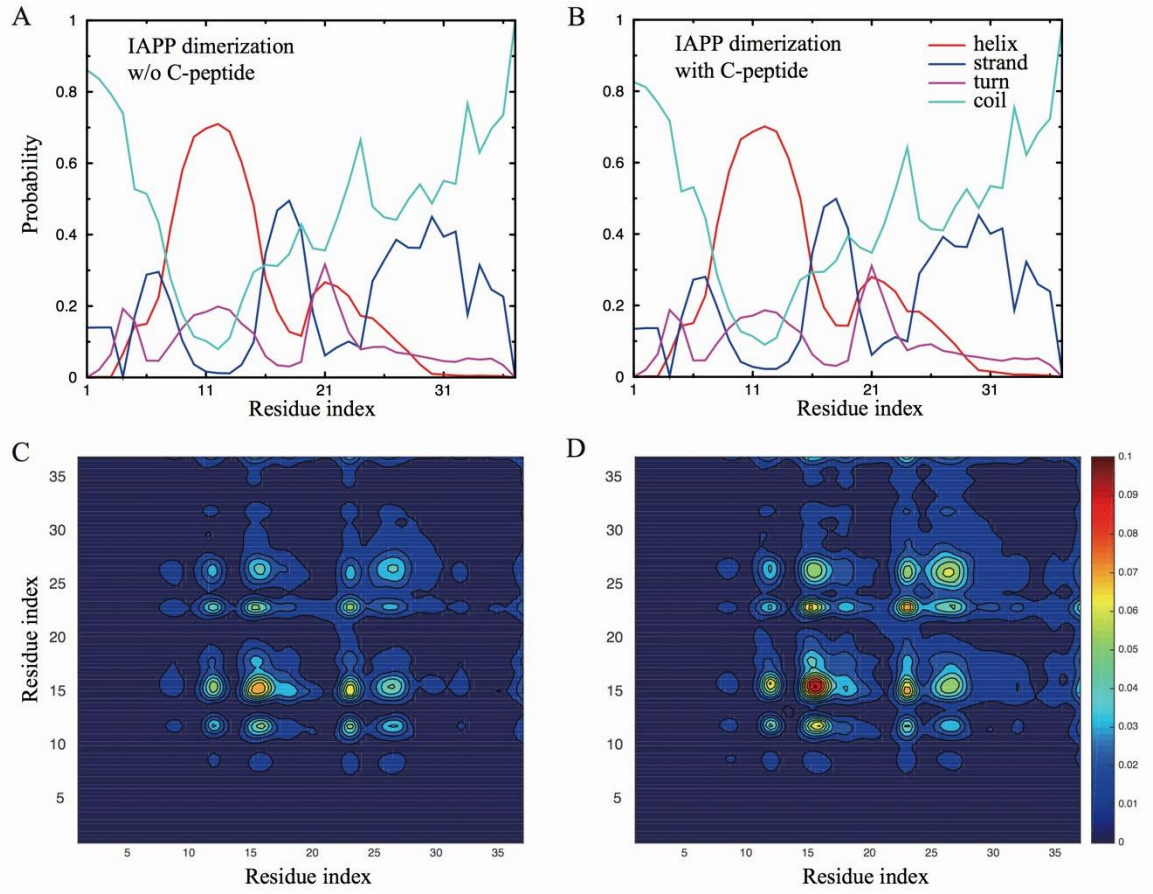

Figure 3-2. Secondary structure information and residue-wise binding frequency maps of IAPPs with and without C-peptide. (A, B) Secondary structure content probability of each residue in IAPP. Data are derived from the last 25ns of simulations and averaged over 100 independent trajectories. (C, D) Contour plots illustrating the residue-wise binding frequency for IAPP-IAPP association. Data are derived from the full-time simulations and averaged.

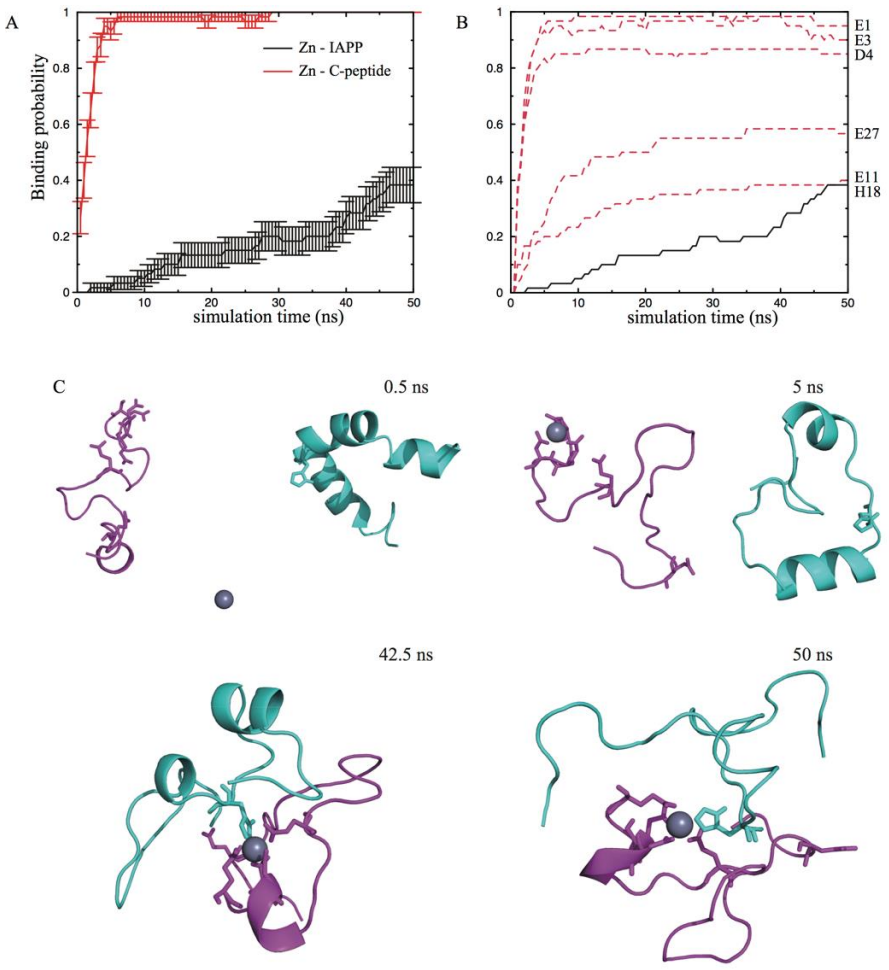

Figure 3-3. DMD simulations of the binding between Zn^{2+}, C-peptide, and IAPP at 1:1:1 molar ratio. (A) Trajectories of binding probabilities of Zn^{2+} with C-peptide and Zn^{2+} with IAPP. Error bars denote the standard error of means (SEM). (B) Trajectories of the averaged binding probabilities of Zn^{2+} with five acidic residues on C-peptide and Zn^{2+} with H18 on IAPP respectively. (C) Structural snapshots illustrating Zn^{2+} coordinating C-peptide and IAPP. IAPP are colored in cyan and C-peptide in magenta, while the zinc ion is illustrated as a grey sphere. Zn^{2+}-binding residues on both peptides are highlighted as sticks.

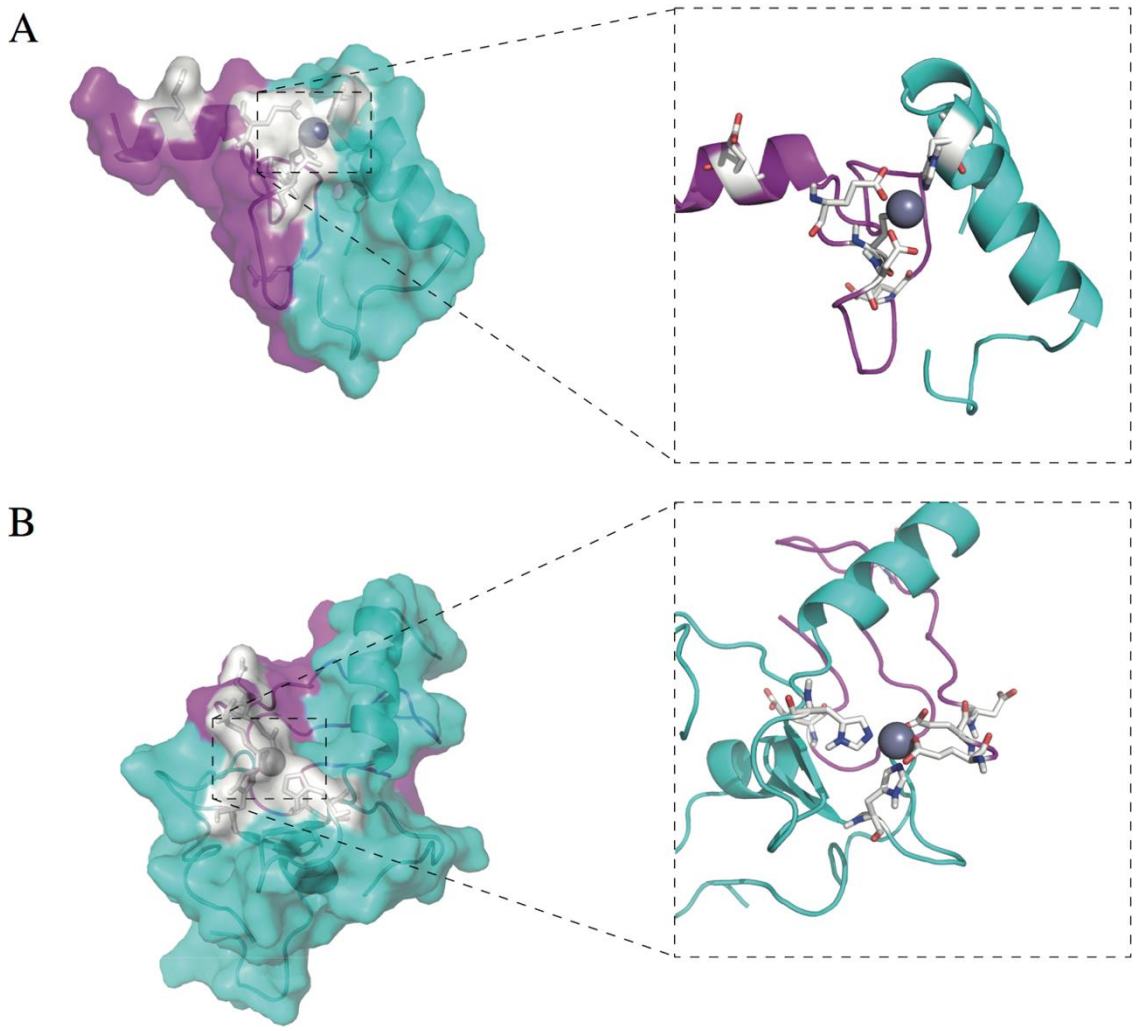

Figure 3-4. Surface structures of the Zn^{2+} coordinated heterodimer and heterotrimer of IAPP and C-peptide. (A) The zinc ion inside the heterodimer is partially solvent exposed, and can possibly bind additional incoming IAPP. (B) The zinc ion inside the heterotrimer is fully buried, preventing further coordination with IAPP. In both panels, IAPPs (and surfaces) are colored in cyan, C-peptide (and surfaces) are colored in magenta. Zinc ions are showed as a grey sphere. All binding residues (and surfaces) are highlighted in enlargements, with stick illustrations and colored in white.

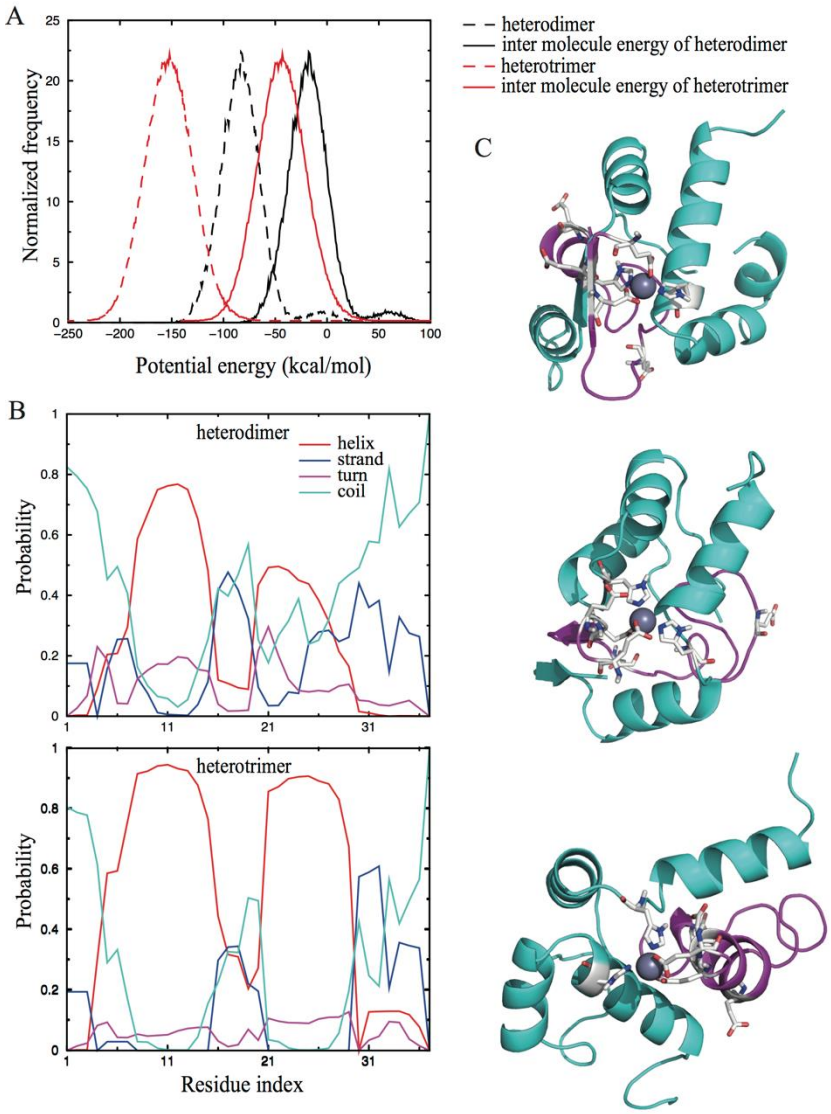

Figure 3-5. DMD simulations of the heterodimer and heterotrimer. (A) The energy gains upon complexation. (B) Secondary structure contents information of IAPP in the heterodimer and heterotrimer respectively. (C) Representative structures of a heterotrimer. IAPP is colored in cyan while C-peptide in magenta. Zinc-binding residues are highlighted as sticks.

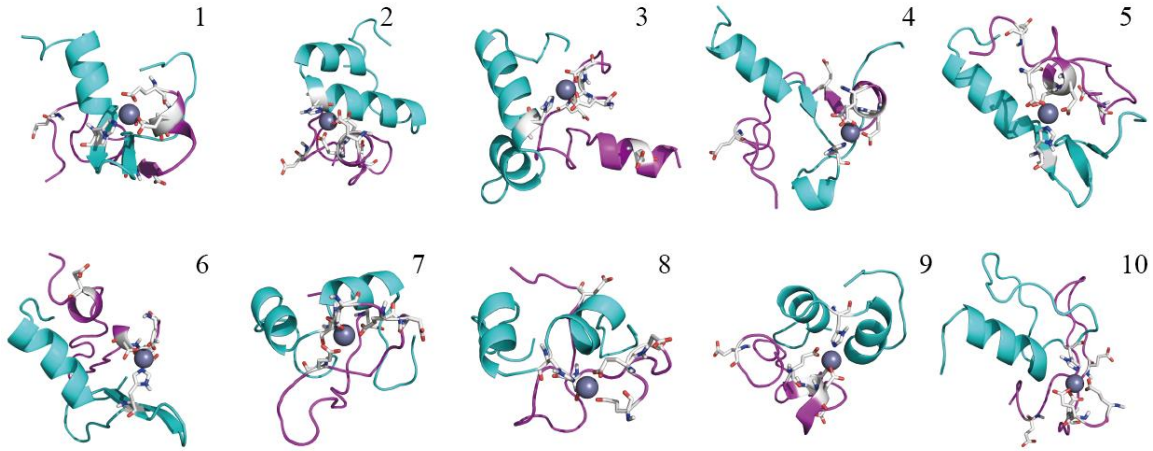

Figure 3-6. The centroid heterodimer structures of the top 10 clusters, with corresponding percentage of 1.57%, 2.36%, 1.57%, 1.57%, 1.77%, 3.74%, 2.16%, 1.97%, 2.56% and 1.18% of total structural ensemble respectively. IAPPs are colored in cyan while C-peptide colored in magenta, and zinc ion shown as a grey sphere. All binding residues (and surfaces) are highlighted as sticks and colored in white.

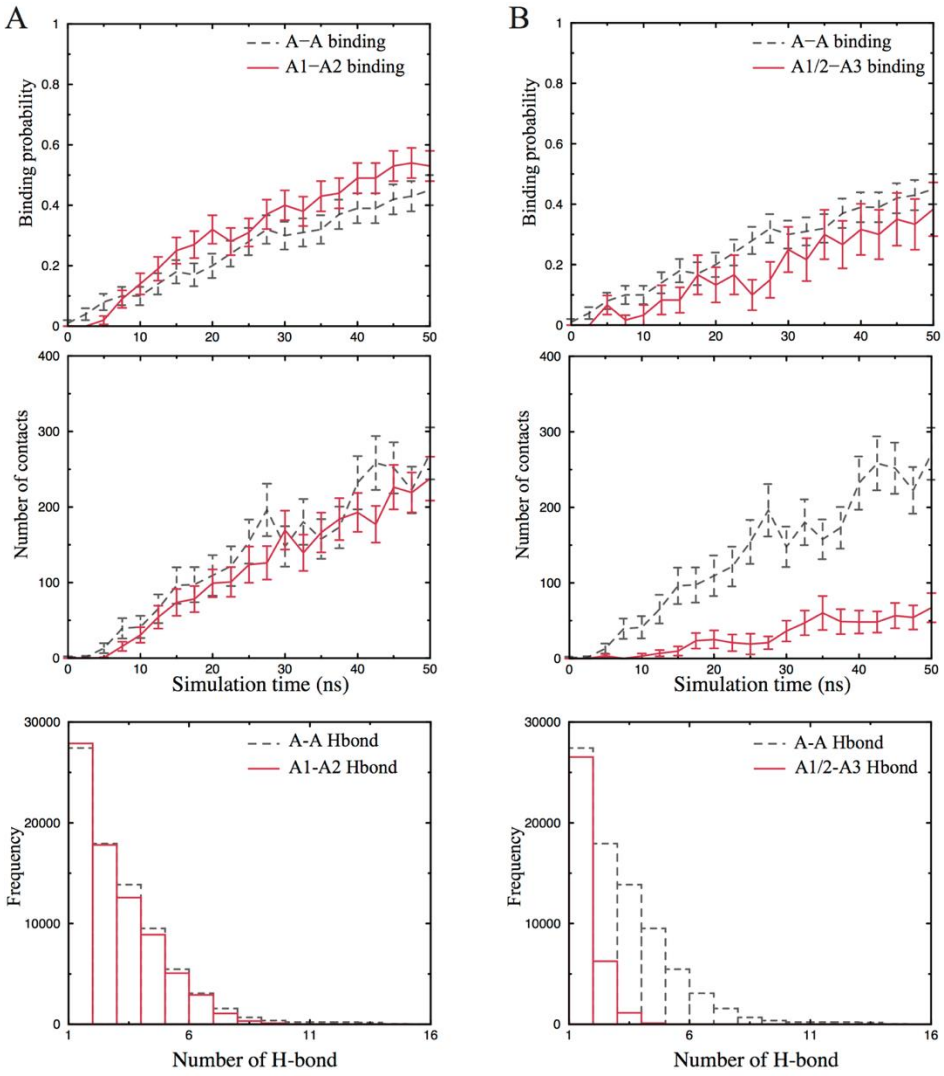

Figure 3-7. Nucleation test of zinc-coordinated heterodimer and heterotrimer. (A) The binding of IAPP in the heterodimer with an incoming IAPP are estimated in terms of IAPP-IAPP binding probability, number of atomic contact, and inter-chain hydrogen bond. The dimer simulations of two IAPPs alone is denoted as A-A binding and colored in grey, while IAPP in the heterodimer is denoted as A1 and the incoming IAPP as A2 respectively. (B) IAPPs in the heterotrimer are denoted as A1 and A2, while the incoming IAPP id denoted as A3. Data are averaged over both IAPPs in the heterotrimer.

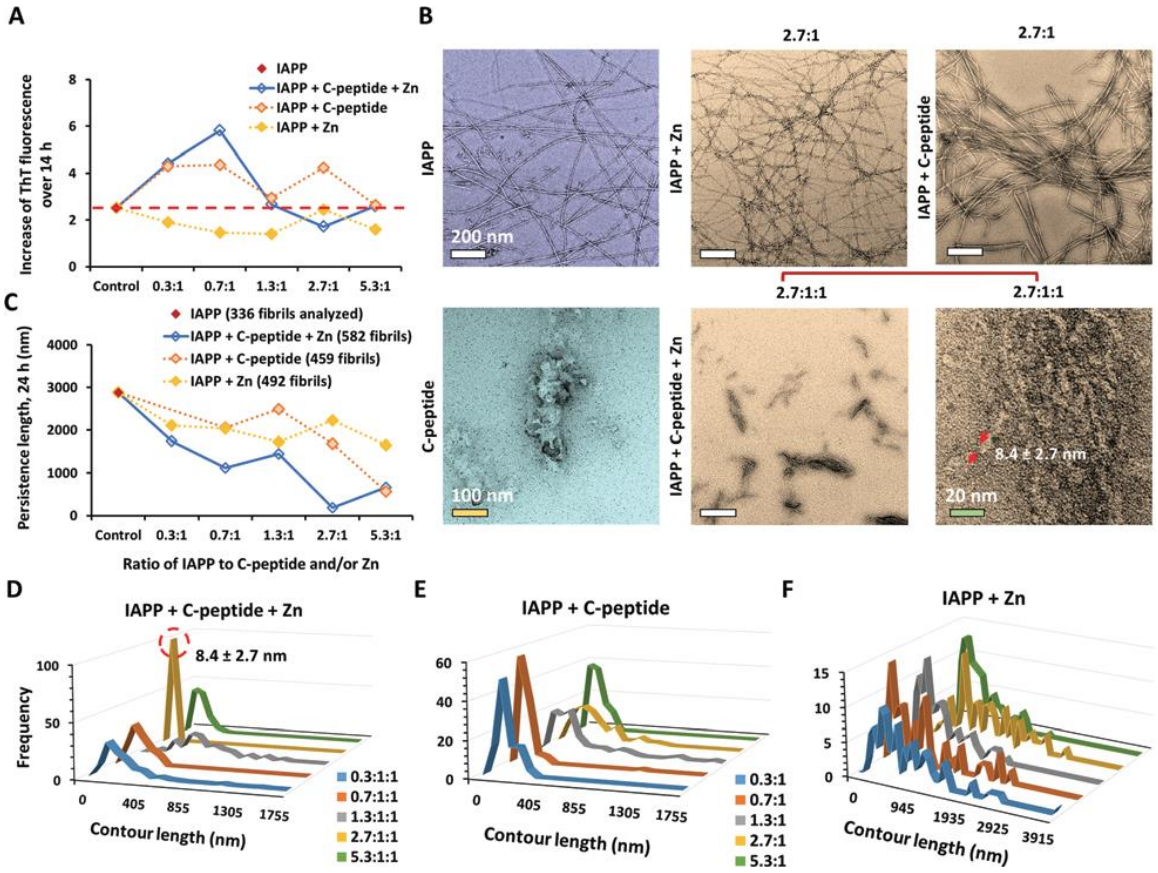

Figure 3-8. Experimental studies of zinc-coordinated IAPP-C-peptide complexation. (A) ThT fluorescence assay for 14h of sample incubation. The time dependent data are shown in Fig. 3-9. (B) TEM imaging of IAPP aggregation after 24h incubation with zinc and/or C-peptide. Only the samples with molecular ratio of 2.7:1 are shown while the rest is in Fig. 3-10. (C–F) Statistical analysis of the persistence length and contour length of IAPP fibrils. The concentration of IAPP is kept 16.9mM in all samples.

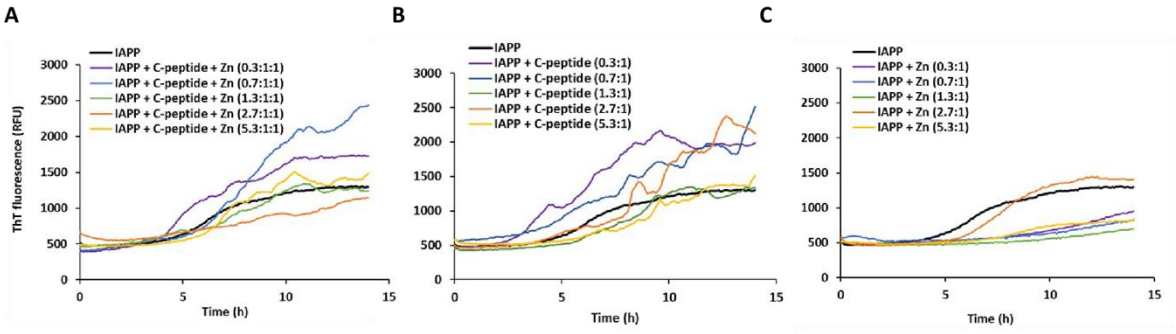

Figure 3-9. ThT fluorescence assay data on zinc-coordinated complexation for 14h of sample incubation. (A) ThT fluorescence assay of IAPP with C-peptide and zinc of various molar ratios. (B) ThT fluorescence assay of IAPP with C-peptide of various molar ratios. (C) ThT fluorescence assay of IAPP with zinc of various molar ratios. The final concentration of IAPP is 16.9μM in all samples.

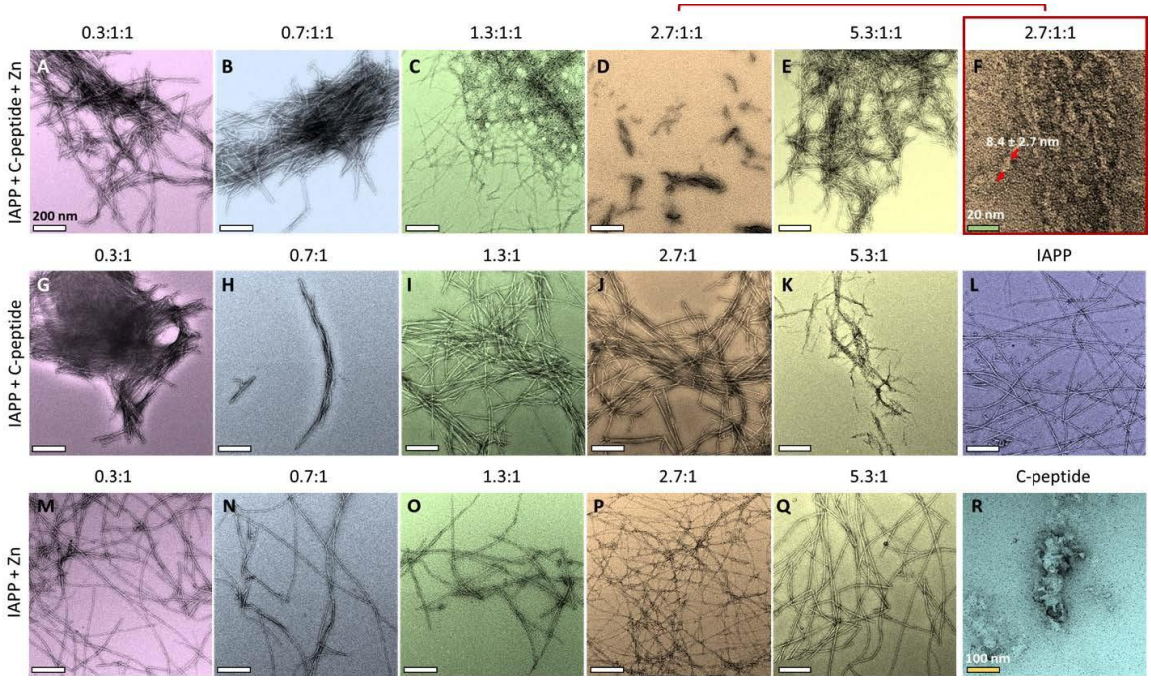

Figure 3-10. High-resolution TEM imaging of zinc-coordinated complexation for 24h of sample incubation. (A-E) IAPP with C-peptide and zinc of various molar ratios. (F) Magnified view of an aggregate in D. (G-K) IAPP with C-peptide of various molar ratios. (L) IAPP control. (M-Q) IAPP with zinc of various molar ratios. (R) C-peptide control. The final concentration of IAPP is 16.9μM in all samples. Scale bars: 200nm unless specified otherwise.

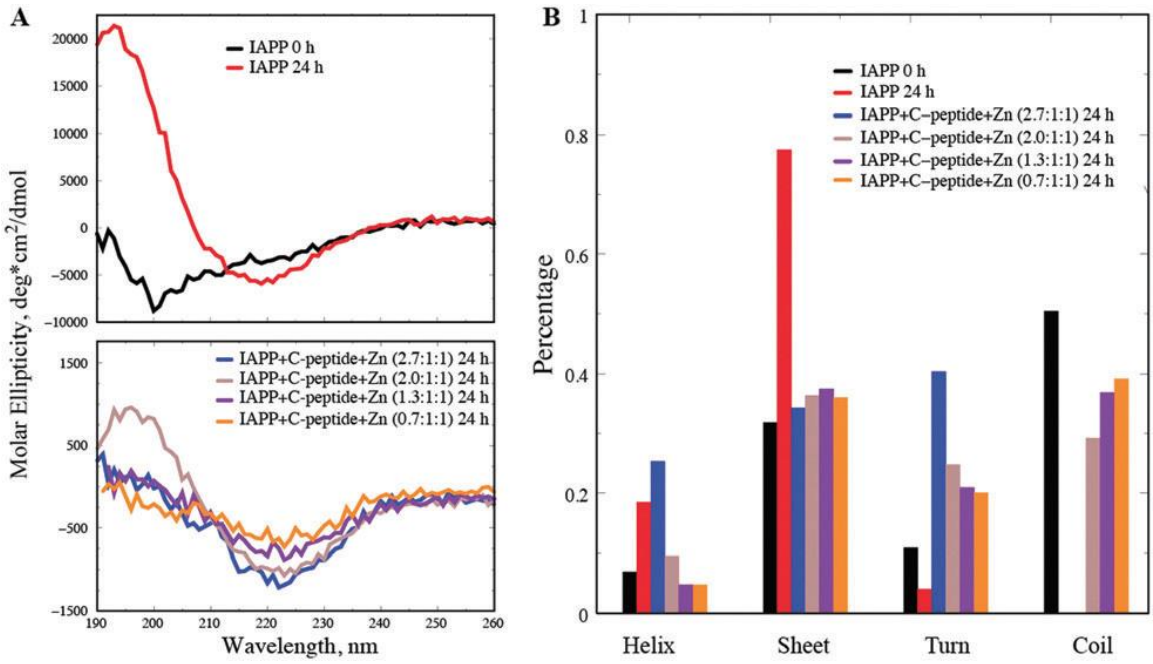

Figure 3-11. CD measurement of the secondary structures of IAPP control and IAPP/C-peptide/Zn^{2+} mixtures. (A) IAPP control of 25mM at 0h and 24h incubation (upper), and IAPP/C-peptide/Zn^{2+} at different molar ratios after 24h incubation (lower). (B) Secondary structural contents for the various molecular systems.

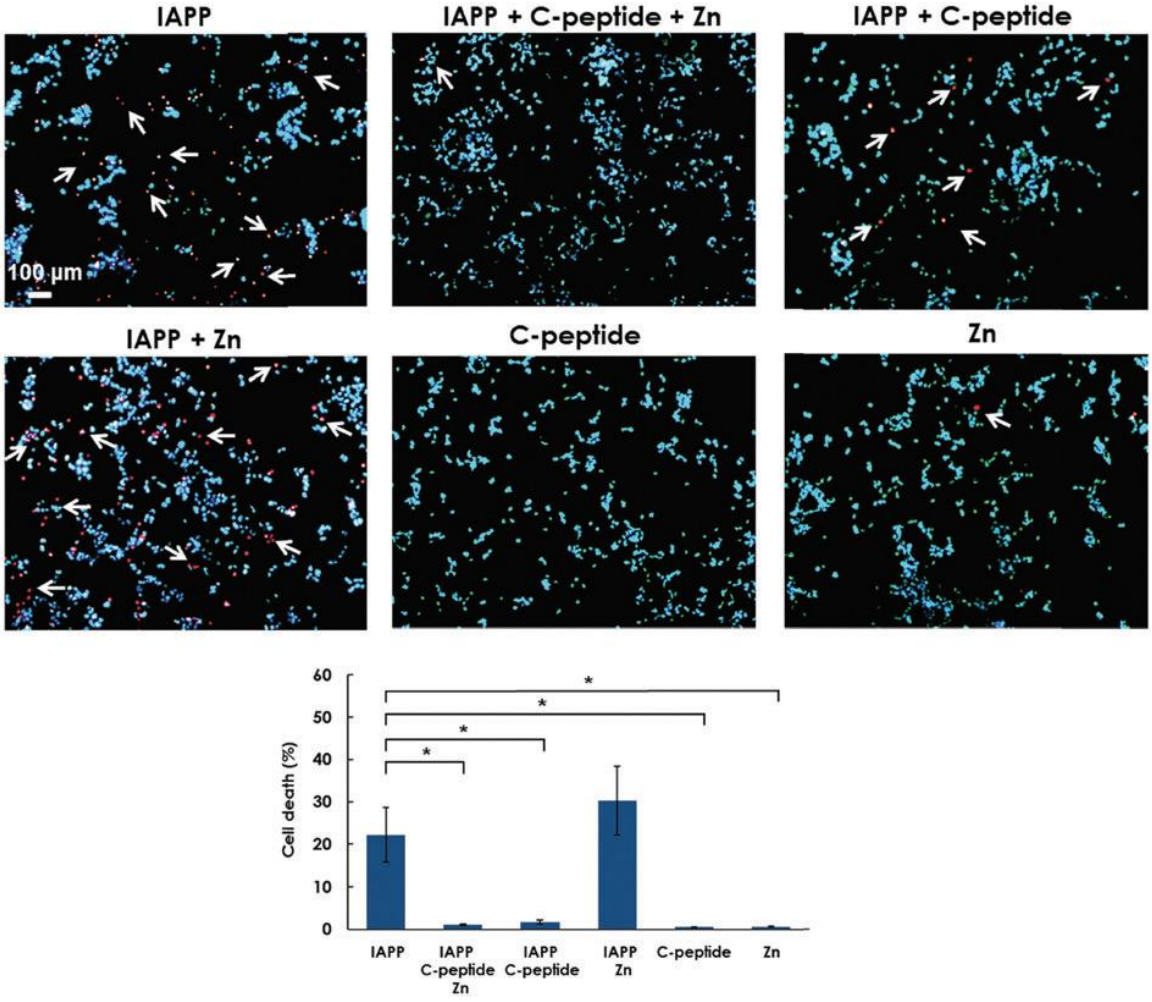

Figure 3-12. C-Peptide protects β-cells from IAPP-induced cell death. NIT-1 cells are untreated (control) or incubated with IAPP, C-peptide, Zn^{2+} or combination as indicated for 24h. Cell death is evaluated by Hoechst-33342 (blue)/propidium iodide (red). White arrows indicate propidium iodide positive cells. Data shown are means ± SEM of 4 independent experiments. *$P < 0.05$.

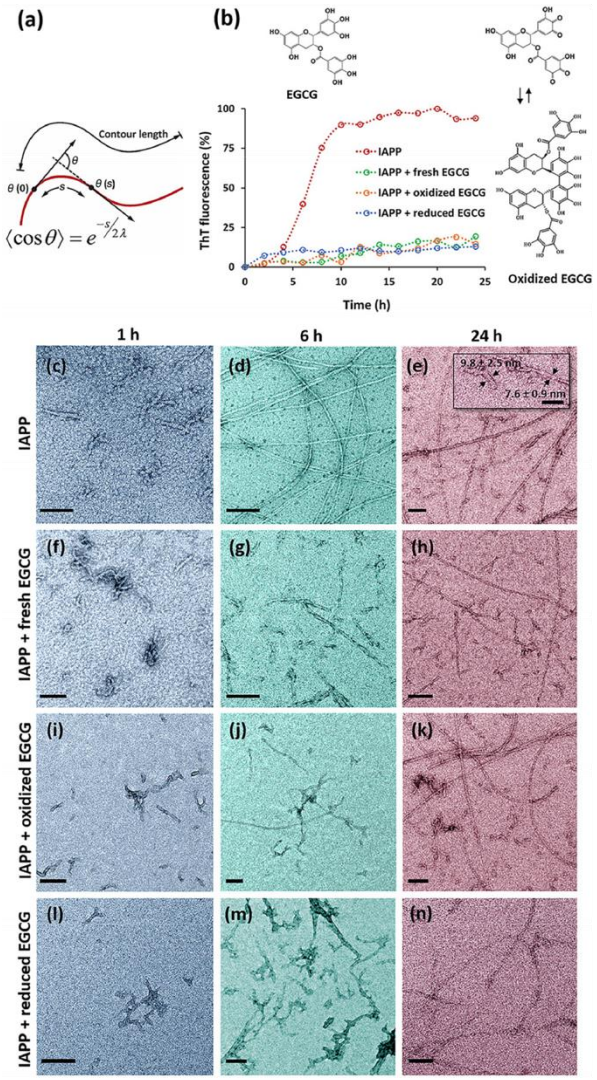

Figure 4-1. (A) Schematic definitions of *l* and λ of the fibril. λ is defined as the length over which angular correlations in the tangent direction decrease by *e* times. Factor 2 in the formula accounts for 2D Euclidean geometry. (B) ThT fluorescence assay of IAPP fibrillation with presence of fresh EGCG, oxidized EGCG, or reduced EGCG. (C–N) TEM images of IAPP fibrillization at 1, 6, and 24h of incubation time with or without EGCG species. All chemicals are prepared at 50μM concentrations and mixed with a 1:1 molar ratio. Scale bar: 100nm.

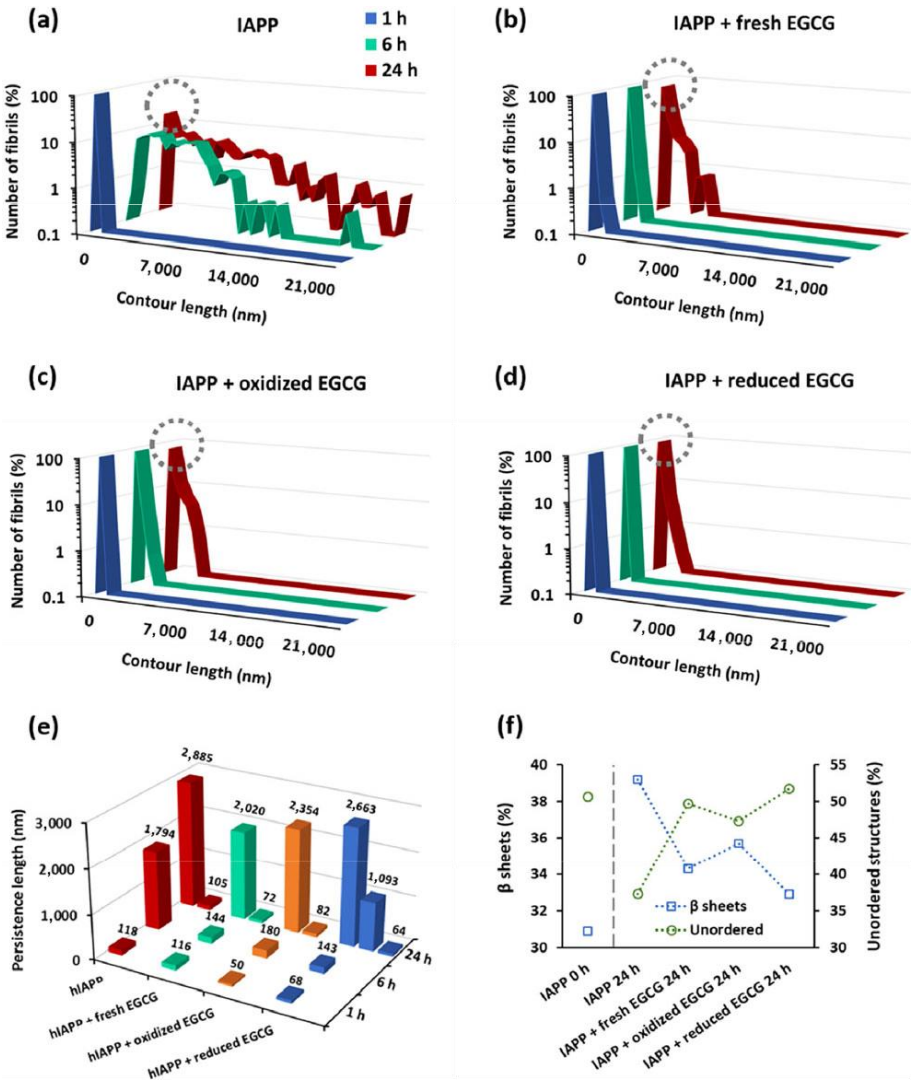

Figure 4-2. Contour length of IAPP fibrils incubated for 0–24 h for (A) IAPP control and (B–D) IAPP incubated with fresh, oxidized, or reduced EGCG. The dashed grey circles indicate populations of small fibrils at 24 h. (E) IAPP fibril persistence length versus time for the four sample conditions. (F) Secondary structures of IAPP incubated with fresh EGCG, oxidized EGCG, or reduced EGCG after 24h of incubation, showing reduced β-sheet and increased unstructured content compared with IAPP control. All chemicals are prepared at 50μM concentrations and mixed with a 1:1 molar ratio where applicable.

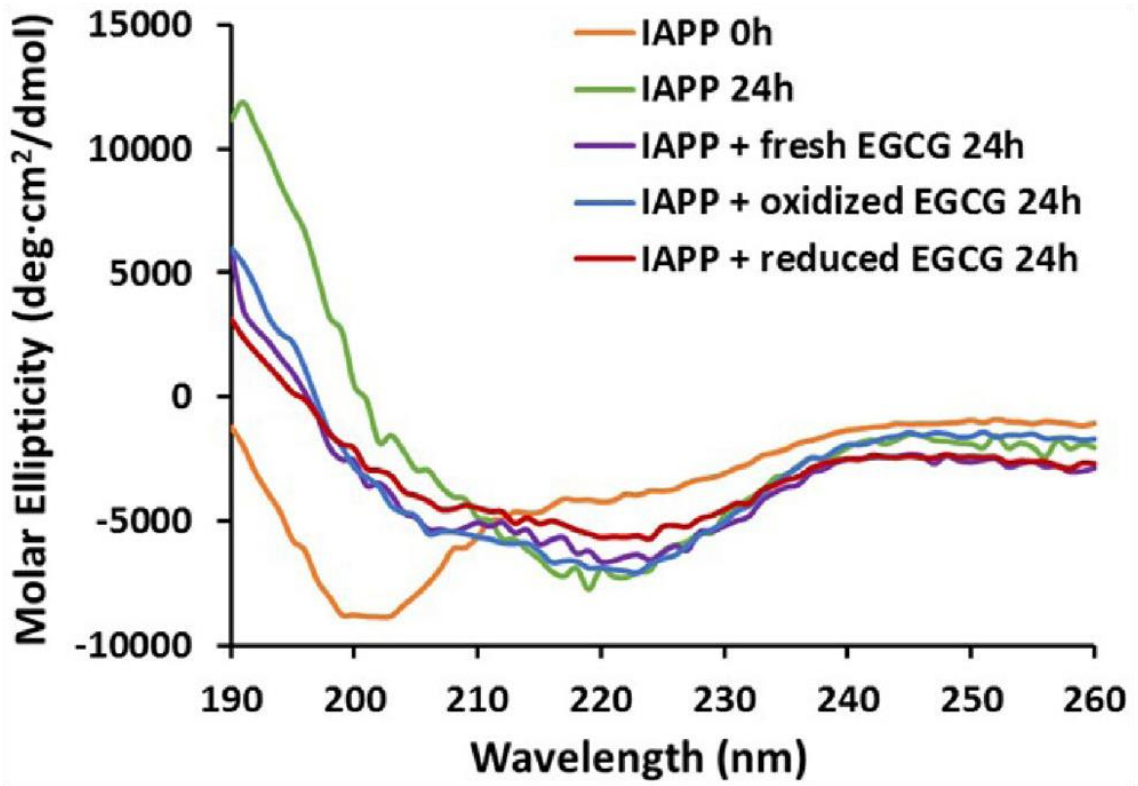

Figure 4-3. Circular dichroism (CD) spectra of IAPP at 0h and 24h, and IAPP with fresh EGCG, oxidized EGCG and reduced EGCG after 24h of incubation (control spectra subtracted).

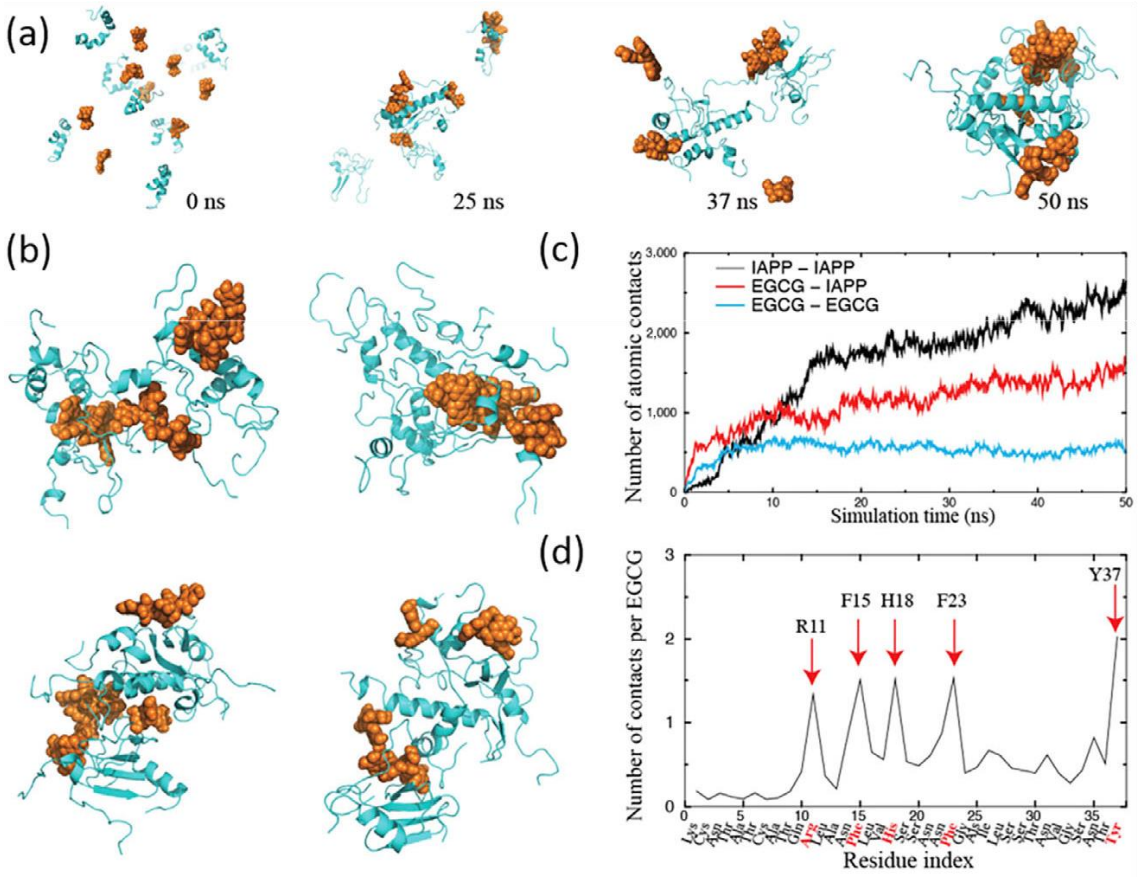

Figure 4-4. DMD simulations of 8 EGCG ligands binding with 8 IAPPs. (A) Structural snapshot illustrating the aggregation process. IAPP are colored in cyan while EGCG are in orange. (B) Final aggregates obtained from 4 independent simulations. (C) Trajectories of the total number of atomic contacts between IAPP-IAPP (black), EGCG-IAPP (red), and EGCG-EGCG (cyan). Data are averaged over 10 independent simulations. (D) Averaged number of atomic contacts between EGCG and each residue on IAPP. Arrows indicate the strong-binding residues.

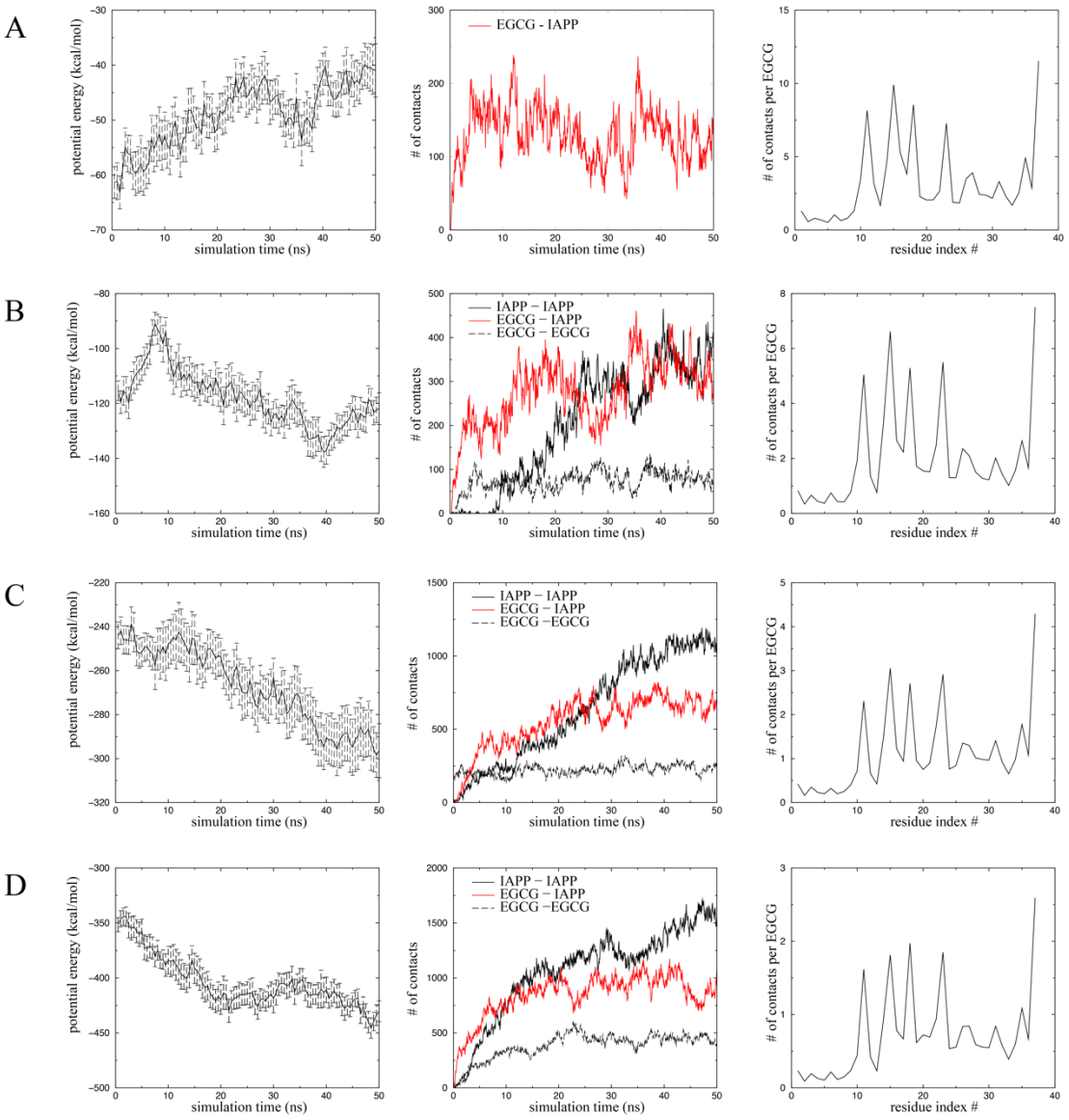

Figure 4-5. DMD simulations of various numbers of EGCGs and IAPPs: (A) 1:1, (B) 2:2, (C) 4:4 and (D) 6:6. All data are averaged over 10 independent simulations for each molecular system. From left to right within each panel displays the trajectories of potential energy, the trajectories of total number of contacts among different simulation components, and the number of atomic contacts between EGCG and each residue on IAPP, respectively.

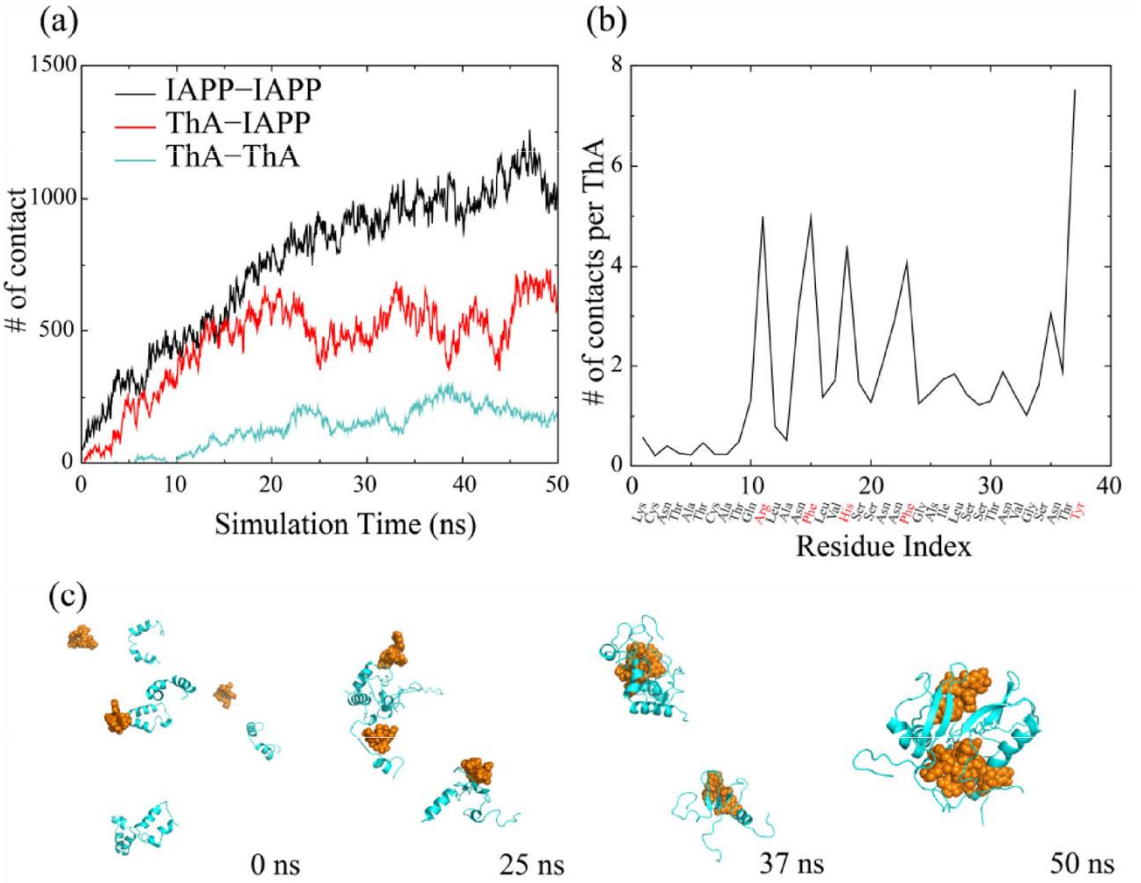

Figure 4-6. DMD simulations of IAPP aggregation with ThA. (A) Trajectories of the total number of atomic contacts between IAPP-IAPP (black), ThA-IAPP (red), and ThA-ThA (cyan). Data are averaged over 10 independent simulations. (B) Averaged number of atomic contacts between ThA and each residue on IAPP. Strong-binding residues are highlighted in red. (C) Structural snapshot illustrating the aggregation process. IAPP are colored in cyan while ThA are in orange.

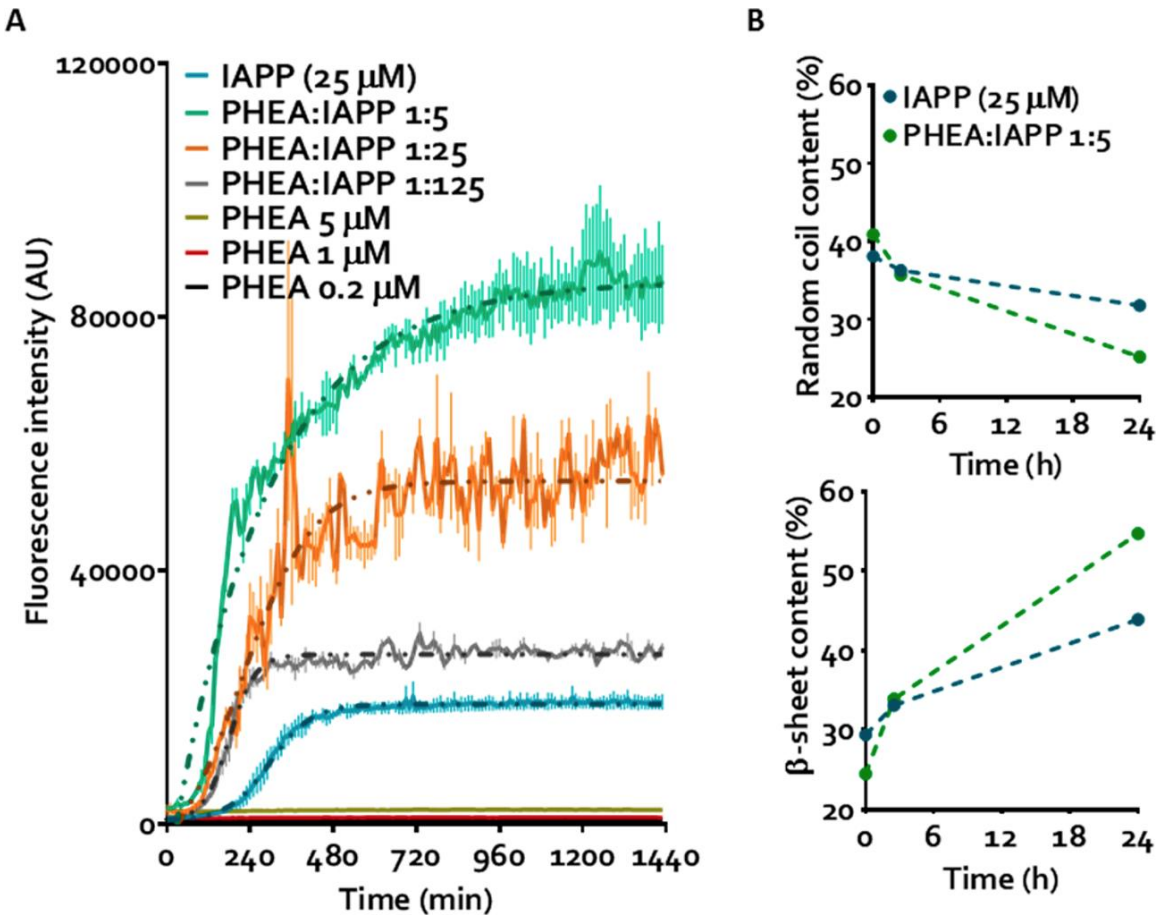

Figure 5-1. (A) ThT fluorescence of IAPP in the presence of PHEA stars over 24h. Dotted lines represent sigmoidal curve fitting (least-squares fit); error is SEM (n=2). (B) Secondary structure transitions in IAPP mapped by circular dichroism at 0, 2.5, and 24h time points. Lines are intended to guide the eye. The concentration of IAPP in all experiments is 25µM.

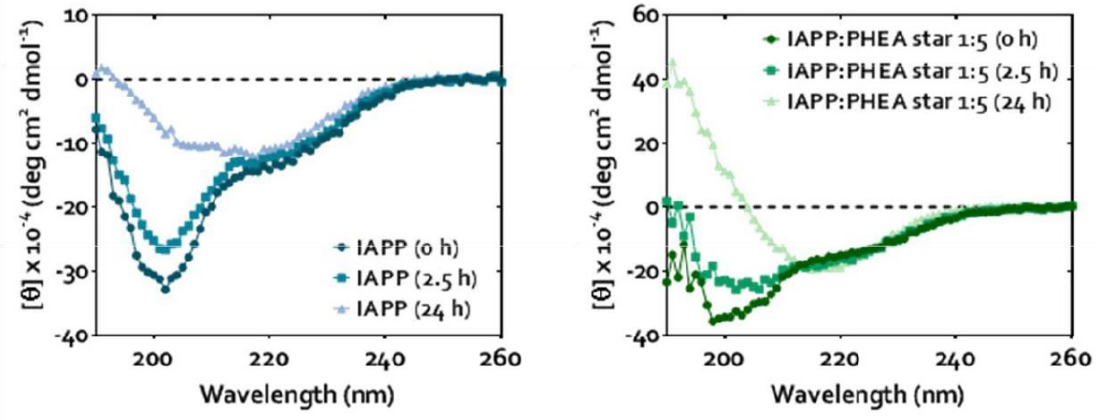

Figure 5-2. Normalized circular dichroism spectra of IAPP (25μM) alone and in the presence of PHEA stars after incubation in Milli-Q water at 0, 2.5 and 24h.

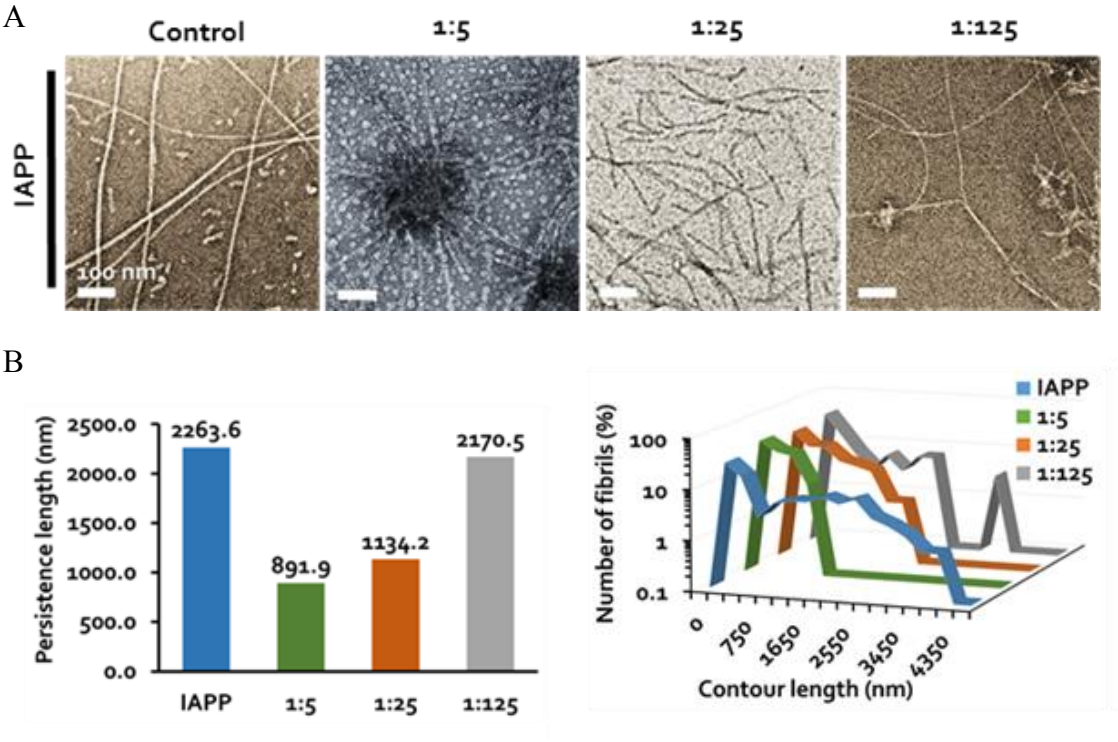

Figure 5-3. (A) TEM imaging of fibrillating IAPP in the presence and absence of PHEA stars after 24h incubation. Stelliform amyloids are seen at PHEA with IAPP at 1:5 molar ratio. Scale=100nm. (B) Structural analysis of amyloid fibrils visualized above. IAPP concentration in all experiments is 25μM.

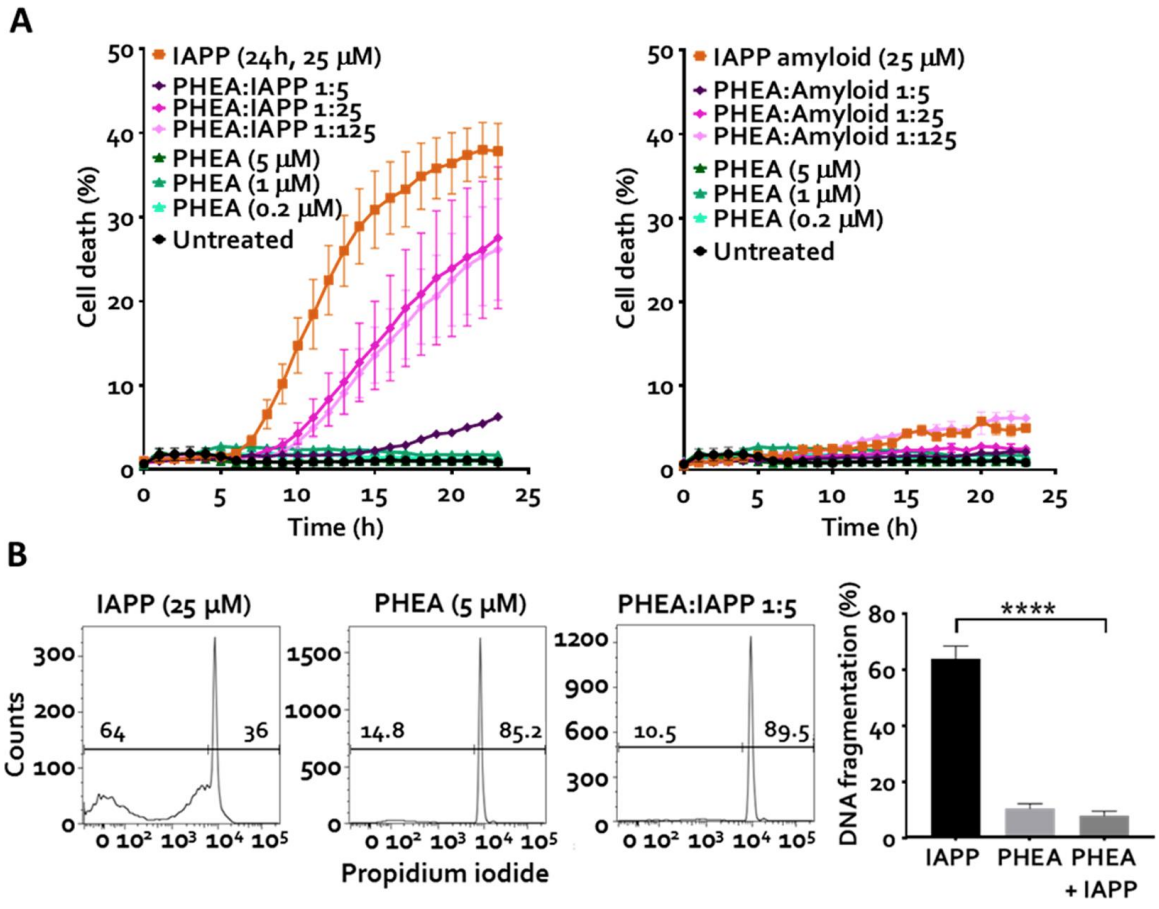

Figure 5-4. Protective effect of PHEA stars against IAPP-mediated cytotoxicity in pancreatic β-cells and islets. (A) *In vitro* cytotoxicity of fibrillating IAPP and mature IAPP amyloids in the presence and absence of PHEA in *β*TC6 cells over 24h. Error=SEM (n=3). (B) *Ex vivo* cytotoxicity of fibrillating IAPP and PHEA with IAPP at a 1:5 molar ratio in mouse islets after 48h incubation. Flow cytometry data is representative of n=5 experiments summarized in the graph. Error=SEM. ****$p < 0.0001$, one-way ANOVA with Tukey's correction.

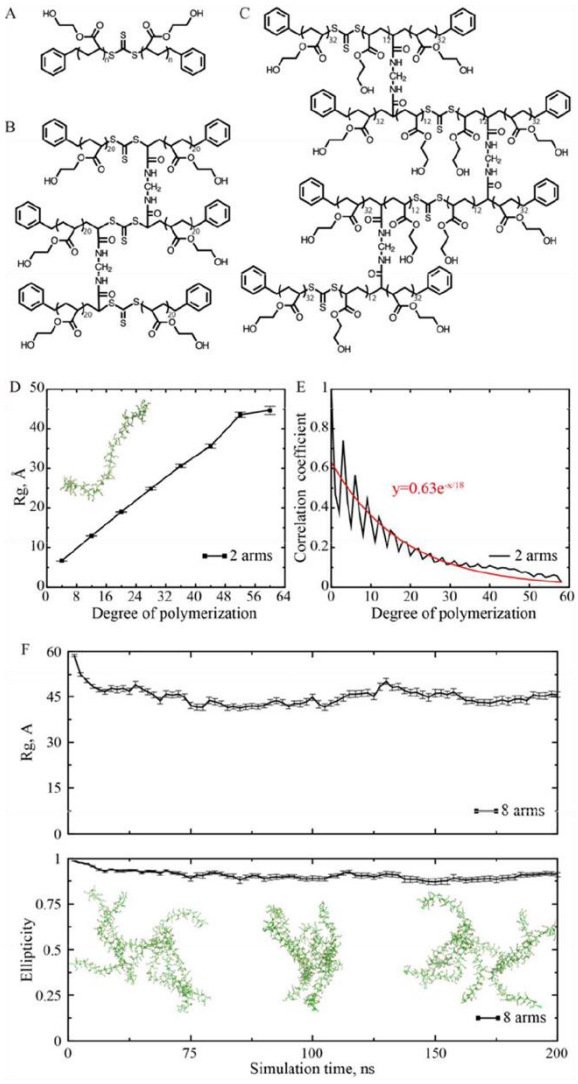

Figure 5-5. Simulations of PHEA stars. (A-C) Chemical structures of the 2-arm, 6-arm, and 8-arm PHEA modelled in simulations. (D) The radius of gyration (*Rg*) of 2-arm PHEA increases approximately linearly with the degree of polymerization. (E) Autocorrelation analysis of 2-arm PHEAs. The exponential fitting returns a persistence length of n~18 (i.e., corresponding to a Kuhn length of ~36). (F) Time evolution of *Rg* and ellipticity of an 8-arm PHEA model with equilibrated structural snapshots in the inset (three different views). Error bars denote the standard error of means (SEM).

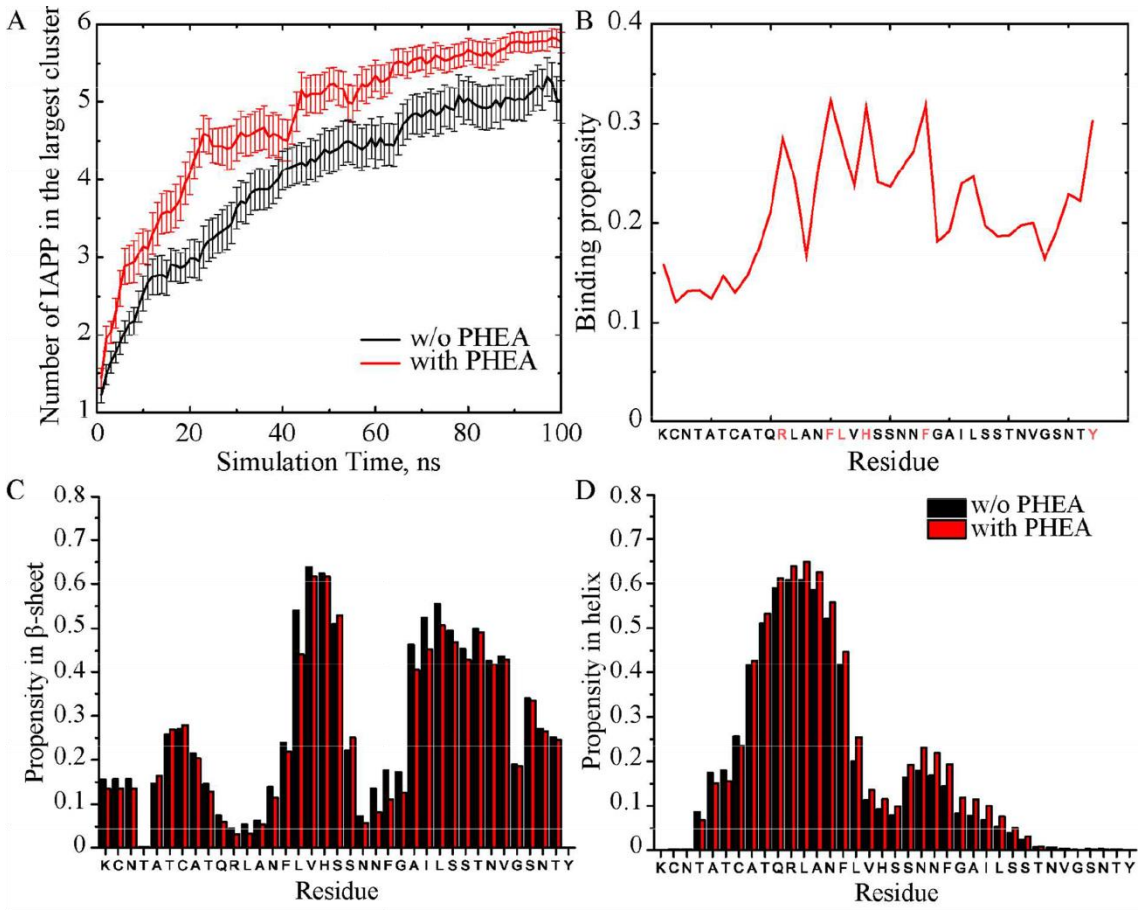

Figure 5-6. Binding of IAPP with 6-arm PHEA. (A) Time evolution of the size of the largest IAPP aggregates in DMD simulations of 6 IAPPs with and w/o the presence of a 6-arm PHEA. Error bars denote the standard error of means (SEM). (B) Binding probability of each IAPP residue with PHEA. Residues with the highest binding probabilities are highlighted in red. (C-D) β-sheet and α-helix content propensities of each IAPP residues. Data are averaged over the last 25ns of DMD simulations.

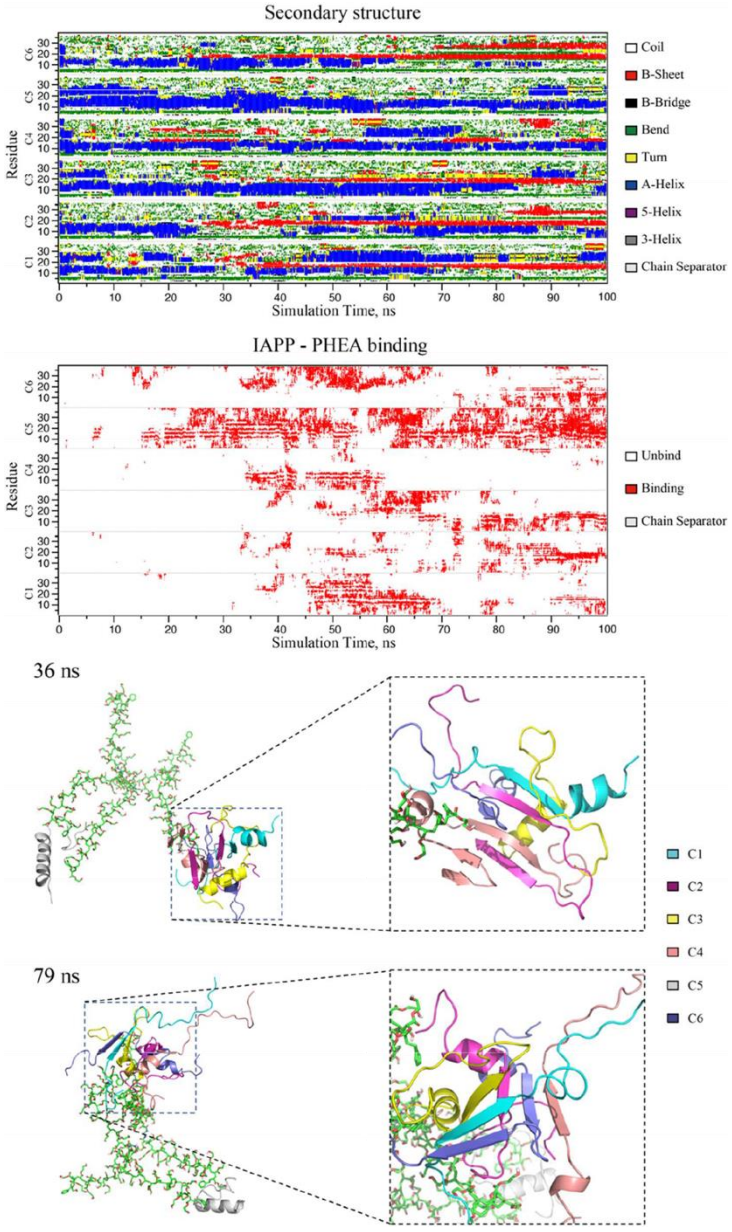

Figure 5-7. β-sheet formation in IAPP aggregates is correlated with their binding with PHEA. Secondary structure change of IAPP peptides (C1 ~ C6) is shown in the upper panel, while the PHEA-binding of each peptide is illustrated as red pixels in the bottom panel accordingly. Snapshots at the 36ns and 79ns are used to display the structure of the modeled system. It's noticeable that one of the peptides (C5) is not clustered in the IAPP aggregate.

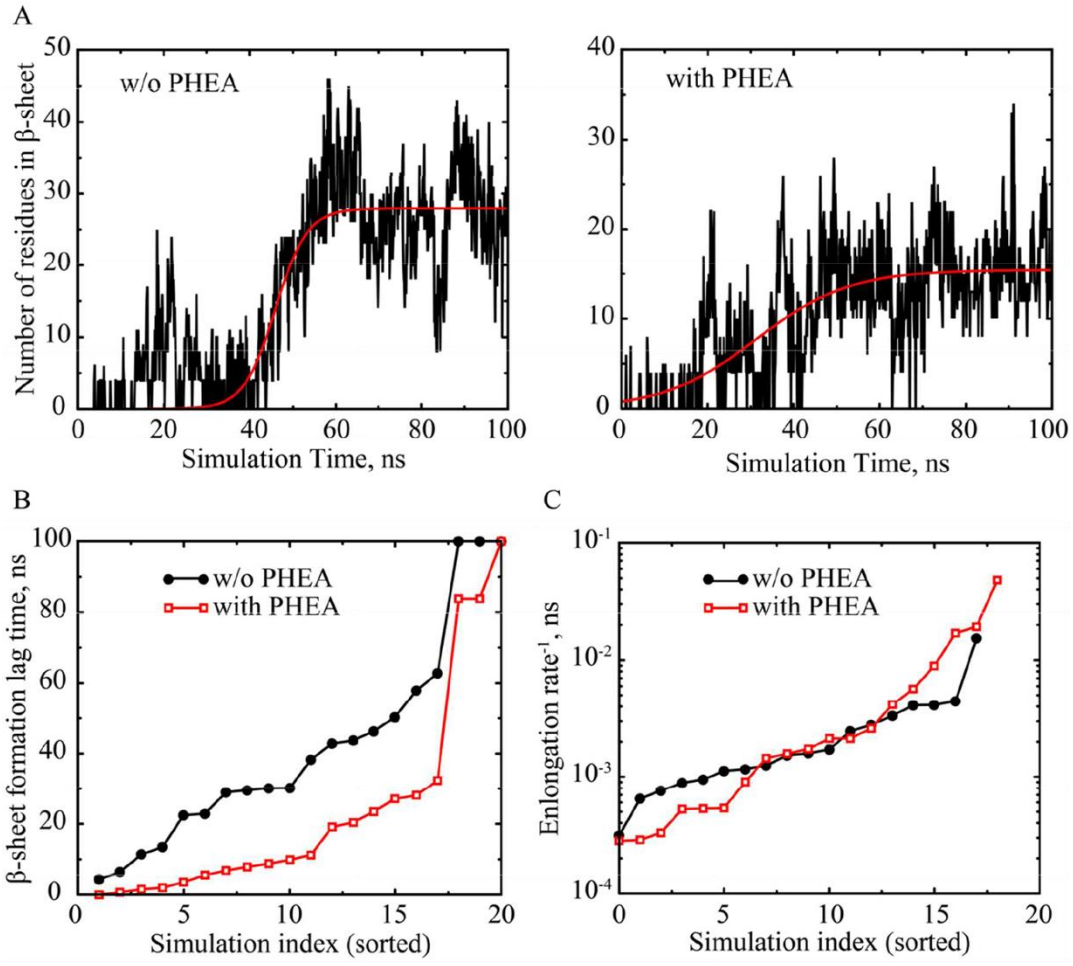

Figure 5-8. Binding with PHEA star reduces the aggregation lag time and induces the heterogeneity in the fibril elongation rate of IAPP self-association. (A) Time evolution of the total number of IAPP residues in β-sheet content with and w/o the presence of a 6-arm PHEA. (B-C) Distributions of the lag time and elongation rate of 20 independent simulations.

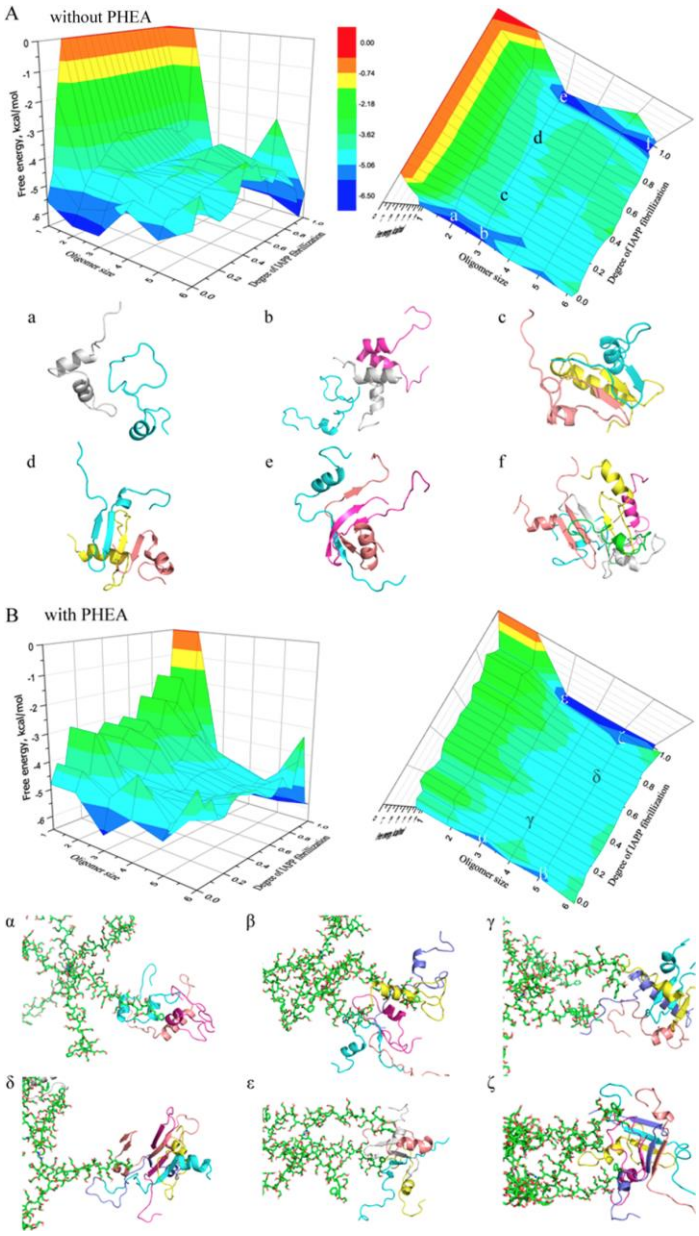

Figure 5-9. Aggregation free energy landscapes of IAPP without (A) and with (B) PHEA. 3D potentials of mean force (PMFs) with respect to IAPP oligomer size and degree of fibrillization are used to derive the free energy landscapes in front and top views. Snapshot structures with IAPP in cartoon and PHEA polymers in stick are shown to illustrate the basins and saddles of the energy landscapes.

REFERENCES

1. Schmitz, O., Brock, B. & Rungby, J. Amylin Agonists: A Novel Approach in the Treatment of Diabetes. *Diabetes* **53,** S233–S238 (2004).
2. Westermark, P., Andersson, A. & Westermark, G. T. Islet Amyloid Polypeptide, Islet Amyloid, and Diabetes Mellitus. *Physiol. Rev.* **91,** 795–826 (2011).
3. Marzban, L. *et al.* Role of β-Cell Prohormone Convertase (PC)1/3 in Processing of Pro-Islet Amyloid Polypeptide. *Diabetes* **53,** 141–148 (2004).
4. Wang, J. *et al.* The Prohormone Convertase Enzyme 2 (PC2) Is Essential for Processing Pro-Islet Amyloid Polypeptide at the NH2-Terminal Cleavage Site. *Diabetes* **50,** 534–539 (2001).
5. Lutz, T. A. Amylinergic control of food intake. *Physiol. Behav.* **89,** 465–471 (2006).
6. Young, A. Inhibition of Gastric Emptying. in *Advances in Pharmacology* **52,** 99–121 (Academic Press, 2005).
7. Naot, D. & Cornish, J. The role of peptides and receptors of the calcitonin family in the regulation of bone metabolism. *Bone* **43,** 813–818 (2008).
8. Padrick, S. B. & Miranker, A. D. Islet Amyloid: Phase Partitioning and Secondary Nucleation Are Central to the Mechanism of Fibrillogenesis. *Biochemistry (Mosc.)* **41,** 4694–4703 (2002).
9. Ferrone, F. Analysis of protein aggregation kinetics. *Methods Enzymol.* **309,** 256–274 (1999).
10. Chen, S., Ferrone, F. A. & Wetzel, R. Huntington's disease age-of-onset linked to polyglutamine aggregation nucleation. *Proc. Natl. Acad. Sci.* **99,** 11884–11889 (2002).

11. Wetzel, R. Nucleation of huntingtin aggregation in cells. *Nat. Chem. Biol.* **2,** 297–298 (2006).

12. Brender, J. R. *et al.* Amyloid Fiber Formation and Membrane Disruption are Separate Processes Localized in Two Distinct Regions of IAPP, the Type-2-Diabetes-Related Peptide. *J. Am. Chem. Soc.* **130,** 6424–6429 (2008).

13. Ritzel, R. A., Meier, J. J., Lin, C.-Y., Veldhuis, J. D. & Butler, P. C. Human Islet Amyloid Polypeptide Oligomers Disrupt Cell Coupling, Induce Apoptosis, and Impair Insulin Secretion in Isolated Human Islets. *Diabetes* **56,** 65–71 (2007).

14. Haataja, L., Gurlo, T., Huang, C. J. & Butler, P. C. Islet Amyloid in Type 2 Diabetes, and the Toxic Oligomer Hypothesis. *Endocr. Rev.* **29,** 303–316 (2008).

15. Zraika, S. *et al.* Toxic oligomers and islet beta cell death: guilty by association or convicted by circumstantial evidence? *Diabetologia* **53,** 1046–1056 (2010).

16. Chiti, F. & Dobson, C. M. Protein Misfolding, Functional Amyloid, and Human Disease. *Annu. Rev. Biochem.* **75,** 333–366 (2006).

17. Soto, C. Unfolding the role of protein misfolding in neurodegenerative diseases. *Nat. Rev. Neurosci.* **4,** 49–60 (2003).

18. Sipe, J. D. *et al.* Nomenclature 2014: Amyloid fibril proteins and clinical classification of the amyloidosis. *Amyloid* **21,** 221–224 (2014).

19. Westermark, P. Aspects on human amyloid forms and their fibril polypeptides. *FEBS J.* **272,** 5942–5949 (2005).

20. Knowles, T. P. J., Vendruscolo, M. & Dobson, C. M. The amyloid state and its association with protein misfolding diseases. *Nat. Rev. Mol. Cell Biol.* **15,** 384–396 (2014).

21. Eisenberg, D. & Jucker, M. The Amyloid State of Proteins in Human Diseases. *Cell* **148,** 1188–1203 (2012).

22. Sawaya, M. R. *et al.* Atomic structures of amyloid cross-[beta] spines reveal varied steric zippers. *Nat. Lond.* **447,** 453–7 (2007).

23. Hofman, A. *et al.* Atherosclerosis, apolipoprotein E, and prevalence of dementia and Alzheimer's disease in the Rotterdam Study. *Lancet Lond. Engl.* **349,** 151–154 (1997).

24. Crane, P. K. *et al.* Glucose Levels and Risk of Dementia. *N. Engl. J. Med.* **369,** 540–548 (2013).

25. de la Monte, S. M. & Wands, J. R. Alzheimer's disease is type 3 diabetes-evidence reviewed. *J. Diabetes Sci. Technol.* **2,** 1101–1113 (2008).

26. de la Monte, S. M., Tong, M., Lester-Coll, N., Plater, M. & Wands, J. R. Therapeutic rescue of neurodegeneration in experimental type 3 diabetes: relevance to Alzheimer's disease. *J. Alzheimers Dis. JAD* **10,** 89–109 (2006).

27. Yan, L.-M., Velkova, A., Tatarek-Nossol, M., Andreetto, E. & Kapurniotu, A. IAPP Mimic Blocks Aβ Cytotoxic Self-Assembly: Cross-Suppression of Amyloid Toxicity of Aβ and IAPP Suggests a Molecular Link between Alzheimer's Disease and Type II Diabetes. *Angew. Chem. Int. Ed.* **46,** 1246–1252 (2007).

28. Li, L. & Hölscher, C. Common pathological processes in Alzheimer disease and type 2 diabetes: A review. *Brain Res. Rev.* **56,** 384–402 (2007).

29. Jackson, K. *et al.* Amylin deposition in the brain: A second amyloid in Alzheimer disease? *Ann. Neurol.* **74,** 517–526 (2013).

30. Oskarsson, M. E. *et al.* In vivo seeding and cross-seeding of localized amyloidosis: a molecular link between type 2 diabetes and Alzheimer disease. *Am. J. Pathol.* **185,** 834–846 (2015).

31. Yan, L.-M., Velkova, A. & Kapurniotu, A. Molecular Characterization of the Hetero-Assembly of β-Amyloid Peptide with Islet Amyloid Polypeptide. *Curr. Pharm. Des.* **20,** 1182–1191 (2014).

32. Qiu, W. Q. *et al.* Association between Amylin and Amyloid-β Peptides in Plasma in the Context of Apolipoprotein E4 Allele. *PLOS ONE* **9,** e88063 (2014).

33. Baram, M., Atsmon-Raz, Y., Ma, B., Nussinov, R. & Miller, Y. Amylin–Aβ oligomers at atomic resolution using molecular dynamics simulations: a link between Type 2 diabetes and Alzheimer's disease. *Phys. Chem. Chem. Phys.* **18,** 2330–2338 (2016).

34. Banks, W. A., Kastin, A. J., Maness, L. M., Huang, W. & Jaspan, J. B. Permeability of the blood-brain barrier to amylin. *Life Sci.* **57,** 1993–2001 (1995).

35. Mulder, H. *et al.* Islet amyloid polypeptide (amylin) is expressed in sensory neurons. *J. Neurosci. Off. J. Soc. Neurosci.* **15,** 7625–7632 (1995).

36. Fawver, J. N. *et al.* Islet amyloid polypeptide (IAPP): a second amyloid in Alzheimer's disease. *Curr. Alzheimer Res.* **11,** 928–940 (2014).

37. Seeliger, J., Weise, K., Opitz, N. & Winter, R. The Effect of Aβ on IAPP Aggregation in the Presence of an Isolated β-Cell Membrane. *J. Mol. Biol.* **421,** 348–363 (2012).

38. M. Young, L. *et al.* Insights into the consequences of co-polymerisation in the early stages of IAPP and Aβ peptide assembly from mass spectrometry. *Analyst* **140,** 6990–6999 (2015).

39. Hutton, J. C. The insulin secretory granule. *Diabetologia* **32,** 271–281 (1989).

40. Jha, S. *et al.* pH Dependence of Amylin Fibrillization. *Biochemistry (Mosc.)* **53,** 300–310 (2014).

41. Khemtémourian, L., Doménech, E., Doux, J. P. F., Koorengevel, M. C. & Killian, J. A. Low pH Acts as Inhibitor of Membrane Damage Induced by Human Islet Amyloid Polypeptide. *J. Am. Chem. Soc.* **133,** 15598–15604 (2011).

42. Abedini, A. & Raleigh, D. P. The Role of His-18 in Amyloid Formation by Human Islet Amyloid Polypeptide. *Biochemistry (Mosc.)* **44,** 16284–16291 (2005).

43. Nedumpully-Govindan, P., Jemec, D. B. & Ding, F. CSAR Benchmark of Flexible MedusaDock in Affinity Prediction and Nativelike Binding Pose Selection. *J. Chem. Inf. Model.* **56,** 1042–1052 (2016).

44. Hutton, J. C. The internal pH and membrane potential of the insulin-secretory granule. *Biochem. J.* **204,** 171–178 (1982).

45. Chimienti, F., Favier, A. & Seve, M. ZnT-8, A Pancreatic Beta-Cell-Specific Zinc Transporter. *Biometals* **18,** 313–317 (2005).

46. Lemaire, K. *et al.* Insulin crystallization depends on zinc transporter ZnT8 expression, but is not required for normal glucose homeostasis in mice. *Proc. Natl. Acad. Sci.* **106,** 14872–14877 (2009).

47. Nedumpully-Govindan, P., Yang, Y., Andorfer, R., Cao, W. & Ding, F. Promotion or Inhibition of Islet Amyloid Polypeptide Aggregation by Zinc Coordination Depends on Its Relative Concentration. *Biochemistry (Mosc.)* **54,** 7335–7344 (2015).

48. Westermark, P., Li, Z.-C., Westermark, G. T., Leckström, A. & Steiner, D. F. Effects of beta cell granule components on human islet amyloid polypeptide fibril formation. *FEBS Lett.* **379,** 203–206 (1996).

49. Brender, J. R. *et al.* Role of Zinc in Human Islet Amyloid Polypeptide Aggregation. *J. Am. Chem. Soc.* **132,** 8973–8983 (2010).

50. Salamekh, S. *et al.* A Two-Site Mechanism for the Inhibition of IAPP Amyloidogenesis by Zinc. *J. Mol. Biol.* **410,** 294–306 (2011).

51. Larson, J. L. & Miranker, A. D. The Mechanism of Insulin Action on Islet Amyloid Polypeptide Fiber Formation. *J. Mol. Biol.* **335,** 221–231 (2004).

52. Gilead, S., Wolfenson, H. & Gazit, E. Molecular Mapping of the Recognition Interface between the Islet Amyloid Polypeptide and Insulin. *Angew. Chem. Int. Ed.* **45,** 6476–6480 (2006).

53. Susa, A. C. *et al.* Defining the Molecular Basis of Amyloid Inhibitors: Human Islet Amyloid Polypeptide–Insulin Interactions. *J. Am. Chem. Soc.* **136,** 12912–12919 (2014).

54. Nedumpully-Govindan, P. & Ding, F. Inhibition of IAPP aggregation by insulin depends on the insulin oligomeric state regulated by zinc ion concentration. *Sci. Rep.* **5,** (2015).

55. Keltner, Z. *et al.* Mass spectrometric characterization and activity of zinc - activated proinsulin C - peptide and C - peptide mutants. *Analyst* **135,** 278–288 (2010).

56. Young, L. M. *et al.* Screening and classifying small-molecule inhibitors of amyloid formation using ion mobility spectrometry–mass spectrometry. *Nat. Chem.* **7,** 73 (2015).

57. Ehrnhoefer, D. E. *et al.* EGCG redirects amyloidogenic polypeptides into unstructured, off-pathway oligomers. *Nat. Struct. Mol. Biol.* **15,** 558 (2008).

58. Cao, P. & Raleigh, D. P. Analysis of the Inhibition and Remodeling of Islet Amyloid Polypeptide Amyloid Fibers by Flavanols. *Biochemistry (Mosc.)* **51,** 2670–2683 (2012).

59. Andreetto, E. *et al.* Identification of Hot Regions of the Aβ–IAPP Interaction Interface as High-Affinity Binding Sites in both Cross- and Self-Association. *Angew. Chem. Int. Ed.* **49,** 3081–3085 (2010).

60. Walsh, D. M. & Selkoe, D. J. Aβ Oligomers – a decade of discovery. *J. Neurochem.* **101,** 1172–1184 (2007).

61. Hung, L. W. *et al.* Amyloid-β Peptide (Aβ) Neurotoxicity Is Modulated by the Rate of Peptide Aggregation: Aβ Dimers and Trimers Correlate with Neurotoxicity. *J. Neurosci.* **28,** 11950–11958 (2008).

62. Uversky, V. N. & Fink, A. L. Conformational constraints for amyloid fibrillation: the importance of being unfolded. *Biochim. Biophys. Acta BBA - Proteins Proteomics* **1698,** 131–153 (2004).

63. Kapurniotu, A. Amyloidogenicity and cytotoxicity of islet amyloid polypeptide. *Pept. Sci.* **60,** 438–459 (2001).

64. Wiltzius, J. J. W., Sievers, S. A., Sawaya, M. R. & Eisenberg, D. Atomic structures of IAPP (amylin) fusions suggest a mechanism for fibrillation and the role of insulin in the process. *Protein Sci.* **18,** 1521–1530 (2009).

65. Kayed, R. *et al.* Conformational transitions of islet amyloid polypeptide (IAPP) in amyloid formation in Vitro11Edited by R. Huber. *J. Mol. Biol.* **287,** 781–796 (1999).

66. Kirkitadze, M. D., Condron, M. M. & Teplow, D. B. Identification and characterization of key kinetic intermediates in amyloid β-protein fibrillogenesis11Edited by F. Cohen. *J. Mol. Biol.* **312,** 1103–1119 (2001).

67. Colvin, M. T. *et al.* Atomic Resolution Structure of Monomorphic Aβ42 Amyloid Fibrils. *J. Am. Chem. Soc.* **138,** 9663–9674 (2016).

68. Khorasanizadeh, S., Peters, I. D. & Roder, H. Evidence for a three-state model of protein folding from kinetic analysis of ubiquitin variants with altered core residues. *Nat. Struct. Mol. Biol.* **3,** 193–205 (1996).

69. Ding, F., Dokholyan, N. V., Buldyrev, S. V., Stanley, H. E. & Shakhnovich, E. I. Direct Molecular Dynamics Observation of Protein Folding Transition State Ensemble. *Biophys. J.* **83,** 3525–3532 (2002).

70. Sugita, Y. & Okamoto, Y. Replica-exchange molecular dynamics method for protein folding. *Chem. Phys. Lett.* **314,** 141–151 (1999).

71. Kumar, S., Rosenberg, J. M., Bouzida, D., Swendsen, R. H. & Kollman, P. A. THE weighted histogram analysis method for free-energy calculations on biomolecules. I. The method. *J. Comput. Chem.* **13,** 1011–1021 (1992).

72. O'Nuallain, B., Williams, A. D., Westermark, P. & Wetzel, R. Seeding Specificity in Amyloid Growth Induced by Heterologous Fibrils. *J. Biol. Chem.* **279,** 17490–17499 (2004).

73. Bitan, G. *et al.* Amyloid beta -protein (Abeta) assembly: Abeta 40 and Abeta 42 oligomerize through distinct pathways. *Proc. Natl. Acad. Sci. U. S. A.* **100,** 330–335 (2003).

74. Meral, D. & Urbanc, B. Discrete Molecular Dynamics Study of Oligomer Formation by N-Terminally Truncated Amyloid β-Protein. *J. Mol. Biol.* **425,** 2260–2275 (2013).

75. Dagliyan, O. *et al.* Engineering extrinsic disorder to control protein activity in living cells. *Science* **354,** 1441–1444 (2016).

76. Emperador, A. & Orozco, M. Discrete Molecular Dynamics Approach to the Study of Disordered and Aggregating Proteins. *J. Chem. Theory Comput.* **13,** 1454–1461 (2017).

77. Ding, F. & Dokholyan, N. V. Emergence of Protein Fold Families through Rational Design. *PLOS Comput. Biol.* **2,** e85 (2006).

78. Brooks, B. R. *et al.* CHARMM: A program for macromolecular energy, minimization, and dynamics calculations. *J. Comput. Chem.* **4,** 187–217 (1983).

79. Lazaridis, T. & Karplus, M. Effective energy functions for protein structure prediction. *Curr. Opin. Struct. Biol.* **10,** 139–145 (2000).

80. Ding, F., Borreguero, J. M., Buldyrey, S. V., Stanley, H. E. & Dokholyan, N. V. Mechanism for the alpha-helix to beta-hairpin transition. *Proteins* **53,** 220–228 (2003).

81. Andersen, H. C. Molecular dynamics simulations at constant pressure and/or temperature. *J. Chem. Phys.* **72,** 2384–2393 (1980).

82. Kabsch, W. & Sander, C. Dictionary of protein secondary structure: Pattern recognition of hydrogen-bonded and geometrical features. *Biopolymers* **22,** 2577–2637 (1983).

83. Mechanistic and Functional Studies of Zinc (II) Activation of C-peptide and its Effect on Red Blood Cell Metabolism. *MSU Libraries* Available at: http://etd.lib.msu.edu/islandora/object/etd%3A589. (Accessed: 24th October 2014)

84. Ge, X. *et al.* Zinc-coordination and C-peptide complexation: a potential mechanism for the endogenous inhibition of IAPP aggregation. *Chem. Commun.* **53,** 9394–9397 (2017).

85. Bieschke, J. *et al.* Small-molecule conversion of toxic oligomers to nontoxic β-sheet–rich amyloid fibrils. *Nat. Chem. Biol.* **8,** 93 (2012).

86. Bieschke, J. *et al.* EGCG remodels mature α-synuclein and amyloid-β fibrils and reduces cellular toxicity. *Proc. Natl. Acad. Sci.* **107,** 7710–7715 (2010).

87. Sancini, G. *et al.* Pulmonary administration of functionalized nanoparticles significantly reduces beta-amyloid in the brain of an Alzheimer's disease murine model. *Nano Res.* **9,** 2190–2201 (2016).

88. Wang, N. *et al.* (−)-Epigallocatechin-3-gallate Inhibits Fibrillogenesis of Chicken Cystatin. *J. Agric. Food Chem.* **63,** 1347–1351 (2015).

89. Gurzov, E. N. *et al.* Inhibition of hIAPP Amyloid Aggregation and Pancreatic β-Cell Toxicity by OH-Terminated PAMAM Dendrimer. *Small* **12,** 1615–1626 (2016).

90. Nedumpully-Govindan, P. *et al.* Graphene oxide inhibits hIAPP amyloid fibrillation and toxicity in insulin-producing NIT-1 cells. *Phys. Chem. Chem. Phys.* **18,** 94–100 (2016).

91. Mahmoudi, M., Akhavan, O., Ghavami, M., Rezaee, F. & Amin Ghiasi, S. M. Graphene oxide strongly inhibits amyloid beta fibrillation. *Nanoscale* **4,** 7322–7325 (2012).

92. Li, M. *et al.* Chemically exfoliated WS<Subscript>2</Subscript> nanosheets efficiently inhibit amyloid β-peptide aggregation and can be used for photothermal treatment of Alzheimer's disease. *Nano Res.* **8,** 3216–3227 (2015).

93. Nedumpully-Govindan, P. *et al.* Stabilizing Off-pathway Oligomers by Polyphenol Nanoassemblies for IAPP Aggregation Inhibition. *Sci. Rep.* **6,** (2016).

94. Xu, C., Shi, P., Li, M., Ren, J. & Qu, X. A cytotoxic amyloid oligomer self-triggered and NIR-enhanced amyloidosis therapeutic system. *Nano Res.* **8,** 2431–2444 (2015).

95. Supattapone, S., Nguyen, H.-O. B., Cohen, F. E., Prusiner, S. B. & Scott, M. R. Elimination of prions by branched polyamines and implications for therapeutics. *Proc. Natl. Acad. Sci.* **96,** 14529–14534 (1999).

96. Fischer, M. *et al.* Influence of Surface Functionality of Poly(propylene imine) Dendrimers on Protease Resistance and Propagation of the Scrapie Prion Protein. *Biomacromolecules* **11,** 1314–1325 (2010).

97. Griffith Jones, O. & Mezzenga, R. Inhibiting, promoting, and preserving stability of functional protein fibrils. *Soft Matter* **8,** 876–895 (2012).

98. Meng, F., Abedini, A., Plesner, A., Verchere, C. B. & Raleigh, D. P. The Flavanol (−)-Epigallocatechin 3-Gallate Inhibits Amyloid Formation by Islet Amyloid Polypeptide, Disaggregates Amyloid Fibrils, and Protects Cultured Cells against IAPP-Induced Toxicity. *Biochemistry (Mosc.)* **49,** 8127–8133 (2010).

99. Sang, S., Lee, M.-J., Hou, Z., Ho, C.-T. & Yang, C. S. Stability of Tea Polyphenol (−)-Epigallocatechin-3-gallate and Formation of Dimers and Epimers under Common Experimental Conditions. *J. Agric. Food Chem.* **53,** 9478–9484 (2005).

100. Kakinen, A. *et al.* Nanoscale inhibition of polymorphic and ambidextrous IAPP amyloid aggregation with small molecules. *Nano Res.* 1–12 (2017). doi:10.1007/s12274-017-1930-7

101. Wang, B. *et al.* Modulating protein amyloid aggregation with nanomaterials. *Environ. Sci. Nano* **4,** 1772–1783 (2017).

102. Chun Ke, P. *et al.* Implications of peptide assemblies in amyloid diseases. *Chem. Soc. Rev.* **46,** 6492–6531 (2017).

103. Cabaleiro-Lago, C. *et al.* Inhibition of Amyloid β Protein Fibrillation by Polymeric Nanoparticles. *J. Am. Chem. Soc.* **130,** 15437–15443 (2008).

104. Breydo, L. *et al.* A hyperbranched dopamine-containing PEG-based polymer for the inhibition of α-synuclein fibrillation. *Biochem. Biophys. Res. Commun.* **469,** 830–835 (2016).

105. Chowdhury, S. R., Agarwal, M., Meher, N., Muthuraj, B. & Iyer, P. K. Modulation of Amyloid Aggregates into Nontoxic Coaggregates by Hydroxyquinoline Appended Polyfluorene. *ACS Appl. Mater. Interfaces* **8,** 13309–13319 (2016).

106. Debnath, K., Shekhar, S., Kumar, V., Jana, N. R. & Jana, N. R. Efficient Inhibition of Protein Aggregation, Disintegration of Aggregates, and Lowering of Cytotoxicity by Green Tea Polyphenol-Based Self-Assembled Polymer Nanoparticles. *ACS Appl. Mater. Interfaces* **8,** 20309–20318 (2016).

107. Fowler, D. M. *et al.* Functional Amyloid Formation within Mammalian Tissue. *PLOS Biol.* **4,** e6 (2005).

108. Cheng, I. H. *et al.* Accelerating Amyloid-β Fibrillization Reduces Oligomer Levels and Functional Deficits in Alzheimer Disease Mouse Models. *J. Biol. Chem.* **282,** 23818–23828 (2007).

109. Ren, J. M. *et al.* Star Polymers. *Chem. Rev.* **116,** 6743–6836 (2016).

110. Jean, L., Lee, C. F., Hodder, P., Hawkins, N. & Vaux, D. J. Dynamics of the formation of a hydrogel by a pathogenic amyloid peptide: islet amyloid polypeptide. *Sci. Rep.* **6,** (2016).

111. Pilkington, E. H. *et al.* Pancreatic β-Cell Membrane Fluidity and Toxicity Induced by Human Islet Amyloid Polypeptide Species. *Sci. Rep.* **6,** (2016).

112. Huang, B., He, J., Ren, J., Yan, X.-Y. & Zeng, C.-M. Cellular Membrane Disruption by Amyloid Fibrils Involved Intermolecular Disulfide Cross-Linking. *Biochemistry (Mosc.)* **48,** 5794–5800 (2009).

113. Friedrich, R. P. *et al.* Mechanism of amyloid plaque formation suggests an intracellular basis of Aβ pathogenicity. *Proc. Natl. Acad. Sci.* **107,** 1942–1947 (2010).

114. Klementieva, O. *et al.* Dense Shell Glycodendrimers as Potential Nontoxic Anti-amyloidogenic Agents in Alzheimer's Disease. Amyloid–Dendrimer Aggregates Morphology and Cell Toxicity. *Biomacromolecules* **12,** 3903–3909 (2011).

115. Cedervall, T. *et al.* Understanding the nanoparticle–protein corona using methods to quantify exchange rates and affinities of proteins for nanoparticles. *Proc. Natl. Acad. Sci.* **104,** 2050–2055 (2007).

116. Pilkington, E. H. *et al.* Effects of Protein Corona on IAPP Amyloid Aggregation, Fibril Remodelling, and Cytotoxicity. *Sci. Rep.* **7,** 2455 (2017).

117. Radic, S., P. Davis, T., Chun Ke, P. & Ding, F. Contrasting effects of nanoparticle–protein attraction on amyloid aggregation. *RSC Adv.* **5,** 105489–105498 (2015).

118. Pilkington, E. H. *et al.* Star Polymers Reduce Islet Amyloid Polypeptide Toxicity via Accelerated Amyloid Aggregation. *Biomacromolecules* **18,** 4249–4260 (2017).

119. Ding, F. & Dokholyan, N. V. Incorporating Backbone Flexibility in MedusaDock Improves Ligand-Binding Pose Prediction in the CSAR2011 Docking Benchmark. *J. Chem. Inf. Model.* **53,** 1871–1879 (2013).